

TWO DIMENSIONAL BACKWARD FACING SINGLE STEP FLOW
PRECEDING AN AUTOMOTIVE AIR-FILTER

By

SHENGHONG YAO

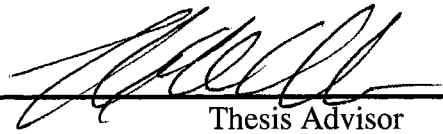
Bachelor of Engineering
Tianjin University
Tianjin, China
1983

Master of Engineering
Tianjin University
Tianjin, China
1986

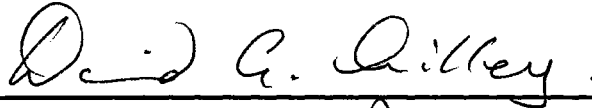
Submitted to the Faculty of the
Graduate College of the
Oklahoma State University
in partial fulfillment of
the requirements for
the Degree of
DOCTOR OF PHILOSOPHY
May, 2000

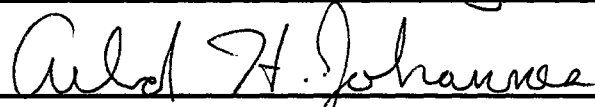
TWO DIMENSIONAL BACKWARD FACING SINGLE STEP FLOW
PRECEDING AN AUTOMOTIVE AIR-FILTER


Thesis Approved:

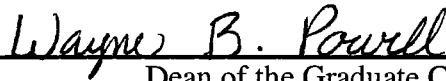


Thesis Advisor









Dean of the Graduate College

ACKNOWLEDGMENTS

In the study of the research topic and the writing of this dissertation, I have received tremendous and invaluable support and assistance from many individuals. It is also difficult to fully express my sincere thanks to my committee for their guidance in the process.

Being an advisor and the chair of my committee, Dr. Chambers has been indispensable in his advice from the beginning. His insistence on doing-it-right on every small detail and searching for the right methodology scientifically sets a great example for me. His trust and constant encourage have motivated me to persist in those years. My thanks also go to Dr. Dougherty, whose work ethics and enthusiasm has shown me how to pursuit one's career. I will remember forever the many times to work with him in the laboratory with our hands. I am truly grateful that Dr. Lilley and Dr. Johannes spent time to review and attend my examinations. Their insightful and constructive remarks and suggestions made this dissertation a better one. I am indebted to Dr. Tong, who gave me a chance to do something that I love to do and to fully enjoy the wonders in scientific research.

I also want to express my deep appreciation for the support and assistance in and out the laboratory from Mr. Abdul Al-Sarkhi and Mr. Yoesbar Sofyan, their friendship helped me tremendously during those years.

None of my achievements in fluid mechanics could happen without the guidance of my mentor, Professor Shu Wei in Tinjin University, who introduced me into the wonderland of fluid mechanics. His utmost integrity as a professional and great personality will be the example for my life.

My most profound gratitude goes to my family. My mother, Yao Shuqin, fed me with knowledge by getting books for me to read in the days at China when knowledge was not appreciated and fine books were hard to find. My big sister, Gao Xiaoran, cares so much about me. My little brother, Gao Shengzhen, took a great care of my late father and is taking a good care of my mother. My aunt, Li Wensu, looked after me in my schooling years. Her practice of dignity and honesty in the harsh time was the best lesson in my life. No one has contributed more to my academic endeavor than my lovely wife and partner Dr. Yibing Du. Her support and appreciation of my pursuit of academic goals have been essential and instrumental to me. I want to thank my newborn son, Bowen. The joy he gives me makes my life better and more meaningful.

TABLE OF CONTENTS

Chapter	Page
Chapter I Introduction	1
1.1 Background	1
1.2 Remaining Problems and Goals	12
Chapter II Numerical Method	15
2.1 Grid Size and Computing Capacity Needed	20
2.2 Large Eddy Simulation.....	22
2.3 Inlet Conditions and Outlet Conditions.....	31
2.4 Finite Difference Scheme.....	32
Chapter III Experimental Setup and Measurement Techniques.....	37
3.1 Two Dimensional Step Flow	37
3.2 Laser Doppler Anemometer	43
3.3 Actual Automotive Housing.....	48
Chapter IV Flow Field of an Actual Automotive Air Filter Housing	50
Chapter V CFD Results of Two-Dimensional Step Flows with and without Air Filter ..	56
5.1 Numerical Results of Step Flow for Homogeneous Pure Fluids	56
5.2 Laminar Flow with Porous Medium Present.....	68
5.3 Summary	96
Chapter VI Experimental Results of Step Flow with filter	97
6.1 Inlet Flow	98

6.2 Flow Fields with Filter Present	101
6.3 Summary	121
Chapter VII LARGE Eddy Simulation of Two Dimensional Turbulent Step Flow	123
7.1 Inlet Flow Conditions and Wall Models	124
7.2 Turbulent Step Flow without the Filter, $Re=10000$	126
7.3 Turbulent Step Flow with Filter at 4.35, $Re=10000$	129
Chapter VIII Conclusions.....	132
8.1 Computation of Laminar Flow with and without Filter	132
8.2 LDA Measurements of Step Flow with and without Filter	134
8.3 The Large Eddy Simulation at $Re=10000$	135
References	136
Recommended Papers	140
Appendices	142
A. LES Filter Process:	142
B. Non-Uniform Computational Grid:.....	143
C. Finite Difference Scheme	144
D. Over-Relaxation Iteration to Solve Poisson Equation.....	147
E. Difference Equations of 2-D LES for Step Flows	148
F. Difference at the Interfaces of Medium and Fluids	163
G. Focus Points for Four Beam LDA Through a Tilted Wall.....	169

LIST OF FIGURES

Figure	Page
Figure 1.1. Schematic of an actual car air-filter housing	3
Figure 1.2. Backward facing step flow. $Re = \frac{\frac{2}{3} U_{max} 2D}{\nu}$	5
Figure 2.1. The placement of the filter in the flow domain.	34
Figure 3.1. Step flow test section of the experimental set up, expansion ratio 1:2.....	39
Figure 3.2. Contraction curve of the channel inlet nozzle and its parameters.	39
Figure 3.3. Schematic of apparatus and instrumentation.	42
Figure 3.4. Set up of the four-beams of a two dimensional LDA	48
Figure 4.1. Schematic diagram of the coordinates in the model air filter housing. (a) The vertical cross section (x-z plane). (b) The top view of measured area, the x-y plane.	50
Figure 4.2. Velocity distributions 12.5 mm above the filter surface. (a) Axial velocity. (b) Vertical velocity.	53
Figure 4.3. Separation lines 12.5 mm above the filter of the air-filter housing model.	54
Figure 5.1. The effects of the grid size on the computed flow fields.....	59
Figure 5.2. Comparison of computed flow fields with the flow fields measured by Armaly et al. (1983) at Reynolds numbers of 100 and 389.	61
Figure 5.3. Reattachment length vs. Reynolds numbers	64
Figure 5.4. Locations of the secondary vortex at the non-step side.	64

Figure 5.5. Contours of velocity u at different Reynolds numbers.	65
Figure 5.6. Flow field for u - v vector at $Re=450$	67
Figure 5.7. Comparison of flows with and without the filter, the upstream edge of the filter is at $20.55h$. (a) Reattachment length. (b) Locations of the secondary vortex. 73	
Figure 5.8. Contour of velocity u with the filter's leading edge at $20.55h$, $Re=600$	75
Figure 5.9. The u - v vector field of flow with the filter's leading edge at $20.55h$, $Re=450$	76
Figure 5.10. Contour of velocity u at different permeability value K 's. Filter's leading edge at $20.55h$, $Re=450$	78
Figure 5.11. Flow field with filter close to the step at $5.85h$, $Re=450$	80
Figure 5.12. Pressure distribution at the upstream side of the filter. $Re=450$, filter's leading edge at $5.85h$	82
Figure 5.13. Velocity distributions entering the filter, filter's leading edge at $5.85h$ $Re=450$	86
Figure 5.14. Velocity distributions after leaving the filter, filter's leading edge at $5.85h$, $Re=450$	86
Figure 5.15. Velocity distributions upstream of the filter with and without the filter, filter's leading edge at $5.85h$, $Re=450$	88
Figure 5.16. Flow fields of different Reynolds numbers, filter's leading edge at $2.85h$. .	91
Figure 5.17. Reattachment length vs. Reynolds number with filter's leading edge at $9.64S$	92
Figure 5.18. Locations of the secondary vortex vs. Reynolds number without and with filter, filter's leading edge is at $9.64S$	94

Figure 6.1. Two dimensionality of the inlet flow, $x=0, y=.5h$.	99
Figure 6.2. Inlet velocity profiles at different Reynolds numbers.	101
Figure 6.3. Separation line of the primary vortex at $Re=2000$.	104
Figure 6.4. Velocity distributions at $x=6.25h$ without filter and with filter at $6.75h$, $Re=2000$.	106
Figure 6.5. Velocity profiles at $x=3.75h$ without and with the filter at $4.25h$, $Re=2000$.	108
Figure 6.6. Velocity profiles at $x=6.25h$ without and with the filter at $6.75h$, $Re=3750$.	110
Figure 6.7. The separation lines of flows with and without filter, $Re=3750$.	112
Figure 6.8. Velocity profiles at $x=3.75$ without and with the filter at $4.25h$, $Re=3750$.	113
Figure 6.9. Velocity profiles $.5h$ upstream of the filter with and without the filter, $Re=6550$. (a) Filter at $6.75h$. (b) Filter at $4.25h$.	116
Figure 6.10. The separation lines of flows with and without the filter, $Re=6550$.	117
Figure 6.11. The dependence of the separation line on Reynolds number, filter at $6.75h$.	118
Figure 6.12. The dependence of the separation line on Reynolds number, filter at $4.25h$.	119
Figure 6.13. The dependence of the separation line on Reynolds number without the filter.	120
Figure 6.14. Results of $Re=10000$. (a) The separation lines with and without the filter. (b) Velocity profiles $.5h$ upstream of the filter without and with the filter at $4.25h$. (c) Velocity profiles $.5h$ upstream of the filter without and with the filter at $6.75h$.	122
Figure 7.1. The fitted inlet curve for $Re=10000$.	125

Figure 7.2. Computed separation line compared with the measured, $Re=10000$	127
Figure 7.3. Comparison of the computed and the measured velocity profiles.....	129
Figure 7.4. The computed separation line compared with the measured at $Re=10000$. .	130
Figure 7.5. Computed and measured velocity profiles .5h upstream of the filter at $Re=10000$	131
Figure E.1. Staggered grids for the inner points.	161
Figure E.2. Staggered grids at the boundaries.....	162
Figure F.1. Grid system at the interface of the filter.	163
Figure G.1. Two horizontally arranged beams with a vertically tilted wall.....	169
Figure G.2. Two vertically arranged beams with a vertically tilted wall.....	170
Figure G.3. The relation between the two points of measuring u and v.	171

NOMENCLATURE

A_i	turbulence eddy diffusion term in the i-direction
b	inertial factor of porous medium
B	modified inertial factor of porous medium
\bar{B}	non dimensional inertial factor of porous medium
C_{pe}	pressure coefficient corresponding to the maximum wall velocity in contraction nozzle
C_{pi}	pressure coefficient corresponding to the minimum wall velocity in contraction nozzle
C_s	constant of Smagorisky's LES model
C_D	drag coefficient
d	length scale of the LES Sub-Grid Stress
d_p	diameter of seeding particles
D	step flow inlet width
D_i	discrete divergence
f	frequency
F_i, F_e	parameters for designing two dimensional contraction curve
g	gravitational acceleration
G	discrete gradient
h	half width of the step flow channel

h_i	numerical mesh size
H	vertical width of the contraction curve
H_i	inertial terms in the Navier-Stokes equation
i	subscripts for space steps
K	permeability of porous medium
\bar{K}	non dimensional permeability of porous medium
L	characteristic length scale
L_{ij}	Leonard stresses
m	subscript for terms pertaining to porous medium
nx	grid number in x direction
ny	grid number in y direction
N_i	total grid number in i-direction
O	on the order of
p	pressure of the fluid
\bar{p}	mean pressure
p_{mo}	modified pressure term
\bar{q}	turbulence kinetic energy
Q	discrete divergence of the intermediate velocity
Re	Reynolds number
R_{ij}	Reynolds stress
S	Step height of step flow
S_{ij}	strain rate tensor

t	time variable
T	time interval
u	velocity or velocity in the horizontal direction
\bar{u}	time average velocity
u'	fluctuating velocity
u^*	wall friction velocity
u^n	velocity at n th time step
\hat{u}	predicted velocity in the time split numerical method
\tilde{u}	non-uniformity velocity in the contraction nozzle
U	mean velocity in the horizontal direction
U_{\max}	the maximum velocity at the inlet of step flow
v	vertical velocity
V	mean vertical velocity
V_e	the maximum wall velocity in contraction nozzle
V_i	the minimum wall velocity in contraction nozzle
V_s	settling velocity of seeding particles
w	over-relaxation coefficient
x	horizontal axis
X	horizontal axis of the contraction curve
X_1	reattachment length of step flow
X_4	distance from the step to the front edge of the secondary vortex
X_5	distance from the step to the downstream edge of the secondary vortex

y	vertical axis
z	axis normal to the x-y plane
α, ζ	transform parameters for non-uniform grid system
Δ	length scale of the LES filter
Δx	grid width, or grid width in the horizontal direction
Δt	time step
ε_{SGS}	eddy viscosity
ϕ	an intermediate term associated with pressure
ϕ_m	porosity of porous medium
φ	an intermediate term associated with pressure for porous medium
μ	kinematics viscosity
ν	kinetic viscosity
ν_T	eddy viscosity
ρ, ρ_f	density of fluid
ρ_p	density of seeding particles
τ_w	wall shear stress

CHAPTER I

INTRODUCTION

1.1 BACKGROUND

Air filter housings in cars are designed with more attention to space utilization than to good fluid dynamics. Consequently the flow paths through the housing tend to have abrupt bends and sudden expansions, as shown in Figure 1.1. Flow is not delivered uniformly over the filter surface and separated flows cause fluid to move away from the filter for a significant part of its surface. For better performance there remains broad room for improvement. There are two issues that are very important for filters' filtration efficiency. First is the effect of the non-uniform distributed flow on the filtration when the mean velocity is not normal to the surface of the filter. Second is the effect of the velocity fluctuations, especially within the separated region where the velocity fluctuates violently with relatively small average velocity. Up to now these issues have not been addressed in sufficient depth. The OSU group has done much research about the flow inside a test housing with both LDA (Laser Doppler Anemometer) measurements and numerical simulations (see Liu, 1995). Gurumoorthy (1990) calculated a three-dimensional flow field inside a car air filter housing using the $K-\epsilon$ turbulent model. These investigations were about flows with the main flow perpendicular to the surface of the filter; and on the time averaged flow field. Separated flow and the dynamic behavior of the filter with large fluctuating velocity have not been studied to this author's knowledge.

There are many publications about the heat or mass transfer of flow fields or temperature fields with porous media present. Most researches in that category are with the main flow parallel to the interface of the pure fluid and the porous media. This is the first work to study the flow that impinges into the air-filter with the filter located inside a separated flow area.

Chwang and Chan (1998) reviewed studies of the use of Darcy's law to analyze waves that are moving past a porous structure. The research emphasizes the wave motion and its basic equation is inviscid. Thus the research does not help much in understanding the interaction of separated viscous flows with porous media.

Better understanding of the interaction between separated flows and porous media can help us design not only better air filter housings but also provides more design choices when perpendicular main flow is not possible. However it is very hard to measure all the details of the real flow field and it would be too costly to build models to cover most geometrical parameters that need to be investigated. Additionally the real flow fields are still too complicated to simulate numerically. We need to find a simplified model that can cover the most important features and that can also be solved. Therefore a backward-facing step flow, as shown in Figure 1.2, was selected for numerical study and a similar setup was built for velocity measurements and flow visualization. The details of the flow were observed with and without an air filter present at adjustable distances from the step. It was investigated experimentally and numerically how the filter affects the flow fields with circulation. The velocity and pressure distributions across the surface of the filter will be presented.

The step flow configuration was motivated by an actual car air filter housing,

which is shown in Figure 1.1. In the actual automotive air-filter housing, two features are dominant according to our measurements. The mean flow impinges on the filter with a not normal angle and the separated flow takes a large portion of the entire flow domain due to a sudden expansion at the inlet. The structure is aerodynamically similar to a backward facing step.

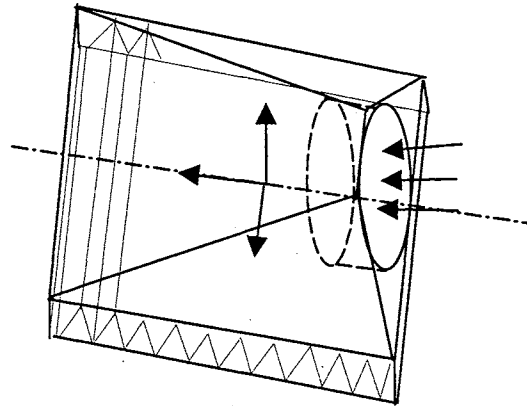


Figure 1.1. Schematic of an actual car air-filter housing

Newman et al. (1997) measured the velocity distributions upstream of a filter in different automotive air filter test housings by LDA (Laser Doppler Anemometer). Filter initial efficiency was estimated using the measured velocity fields and filtration models. They concluded that differences in velocity distributions resulted in small differences in filter initial efficiency. Modifications made to the test housings had small effects on the velocity distributions, which presented a very non-uniform flow to the filter. One should note that the test housing in their experiment is very different from real vehicle housings.

With housings that were similar in shape to a real air-filter housing, Al-Sarkhi et al. (1997) measured the velocity fields upstream of the filter. Their results indicate that

the flow fields upstream of an automotive air filter can have a significant effect on the filtration performance of the filter. The mean velocity distribution entering the filter is important to the efficiency, restriction and capacity of the filter. Filter performance can be improved by improving the velocity distribution, preferably uniform flow impinging directly into the filter. However in most engineering conditions, uniform flow normal to the filter surface is not easy to achieve. Many filter housings are configured in the way that the flow enters the housing with its largest component parallel to the upstream surface of the filter. Therefore, their experiments were performed with fully developed rectangular duct flow and a rectangular housing. The main flow entered the housing in the direction parallel to the filter surface and was forced to change its direction 90 degrees inside the housing. Three different housing configurations were established to control the flow distribution just upstream of the filter. LDA was used to measure the velocity fields throughout the plane 13 mm above the filter. It was found that with some minor changes in the housing, flow distributions could be changed significantly for the better, that is less separated area and flatter mean velocity distributions. Al-Sarkhi et al. (1999) predicted the filtration efficiency theoretically based on the real flow distribution obtained by LDA measurements for housings of different configurations. They found that the mean velocity distributions with filter present are flatter than the distributions without filter due to the resistance added by the filter. The flow fields with less separated areas provided much better filtration results for 1 μm diameter particles with higher filtration efficiency at higher velocity regions. The filtration efficiency of 10 μm diameter particles appeared independent of velocity distributions for the cases in which particle adhesion to the fibers of the filter was assumed perfect. With the application of an adhesion model,

the efficiency for large particles also exhibited a dependence on the velocity distribution.

A large amount of experimental data is available for the flow over a backward-facing step, therefore it is very good to serve as a prototype for laminar and turbulent flows in complex geometry, as noted by Kaiktsis et al. (1991). Step flow is a classic separation flow that served as a stiff test case for numerical codes and experimental techniques, as noted by Scarano and Riethmuller (1999) and Badran and Bruun (1999). It has three important properties: strong velocity shear at the edge of the step, strong separation flow behind the step and downstream developing channel flow with boundary layer flow recovery from the separation. A typical flow domain of a backward facing step flow is shown in Figure 1.2. Reynolds number is defined as $Re = 4U_{\max} D / (3\nu)$. In the low-Reynolds number regime, a unique relationship exists between the Reynolds number (Re), the expansion ratio and the normalized length of the circulation zone (X_1/S). In the high-Reynolds number regime, the reattachment length is determined by the expansion ratio and weakly correlated with the Reynolds number. So numerical methods and experimental results in the step flow can be tested on some basic aspects.

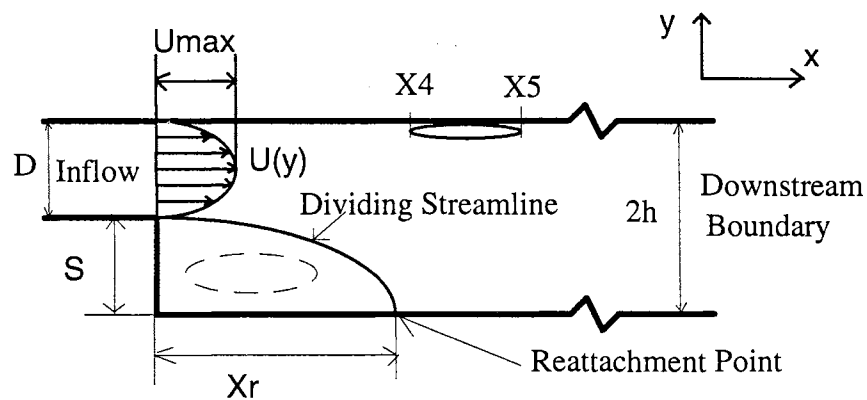


Figure 1.2. Backward facing step flow. $Re = \frac{2}{3} \frac{U_{\max} 2D}{\nu}$

Most information about turbulent separation flows was gained visually (Abbott and Kline, 1961, cited from Armaly et al. 1983) or inferred from hot-wire anemometer and pressure measurements (Bradshaw et al. 1972, Kim, 1978, cited from Armaly et al. 1983) in the early days. The detailed structure of the flows was not given until the development of the LDA in the 1970s, when potentially accurate measurements throughout a turbulent separated flow could be made. Armaly et al. (1983) used a single component LDA to study the flow over a backward facing step. The Reynolds number range was $70 < Re < 8000$, including laminar, transitional and turbulent flow regimes. Additional regions of flow separation downstream of the step were found on the flat side of the channel where no step was present. The experiment showed that the flow downstream of the step was two-dimensional at low and high Reynolds numbers, and was three-dimensional at Reynolds numbers in between. Two-dimensional numerical predictions were also made at low Reynolds numbers and agreed reasonably well with their experimental results.

Driver et al. (1985) did experimental and numerical studies on the flow over a backward facing step. Wall static pressure and time averaged surface skin-friction were measured and the instantaneous velocity was detected by a two component LDA. Two-dimensional $k-\varepsilon$ model and algebraic-stress turbulence model computations were carried out. The experiment provided extensive data for the mean velocity field and turbulence intensity distribution for a two-dimensional step flow. However the numerical results displayed only qualitative agreement with the experiment; quite large discrepancies existed at the strong shear zone near the step edge.

Kim and Moin (1985) studied two-dimensional step flow at low Reynolds

numbers by the numerical method that will be used in this paper. The results agreed well with Armaly's experimental results. They developed a special procedure that significantly reduced the computation time. Details will be discussed later.

Adams et al. (1988) studied experimentally the subsonic backward step flow. A single component LDA was used to measure the inlet flow and the velocity profile along the channel. The results indicated that upstream initial conditions were very important to the development of the shear layer downstream of the step. A thick boundary layer at inlet caused a lower pressure rise to reattachment and a lower pressure gradient at reattachment than cases with thinner initial separating boundary layers.

Low Reynolds number step flow was studied by Ku et al. (1989) with the direct numerical simulation (DNS) method. The flow domain was divided into a few subdomains, each of simple geometry, with the continuity equation as the boundary condition at the overlapped interfaces. Their results were in good agreement with experiments for low Reynolds numbers.

Kaiktsis et al. (1991) used a high-order-accurate mixed spectral/spectral element DNS model to investigate three-dimensional transitional flow over a backward step. By observing the instantaneous and time averaged velocity field aided with correlation methods, three dimensional bifurcation and secondary instabilities were studied. Very good agreement with experimental results was obtained on the relationship between the reattachment length with respect to Reynolds number. At low Reynolds number, $Re=500$, ($Re = U_{\max} S / \nu$, where U_{\max} is the maximum velocity at inlet, S is the step height and ν the viscosity of fluid), three different inlet velocity profiles were introduced to observe the effects of the initial conditions. Compared with the uniform inlet flow, a triangle

velocity profile produced a reattachment length X_r , about 18% longer and a parabolic inlet condition decreased the length about 27%. It should be noted that the definition of Reynolds number here is different than the definition in Figure 1.2. The definition in Figure 1.2, the same as in Armaly et al. (1983), will be used in this paper. The Reynolds number of Kaiktsis et al. is equivalent to about 660 in Armaly et al. This is consistent with Armaly's results that it is in the transitional regime.

By pitot tubes and hot-wire anemometer Yoo et al. (1992) measured the velocity and the fluctuating statistics beyond the separation and reattachment for a transitional flow over a backward step. The flow was a boundary layer flow, not a channel flow as others. They found that the wall pressure continued to reverse even slightly after the reattachment, reaching a maximum at $x/S=8$; eight times the step height. A discrepancy of the velocity profile from the universal law of the wall was observed after reattachment. The profile is gradually recovered until $x/S=25$, where the log law applied to $y^+=500$ in the direction normal to the wall. However in the outer region, the effect of the upstream mixing layer still existed even at $x/S=50$. The energy dissipation rate was obtained through numerical integration of the second moment of the energy spectrum. A non-equilibrium state was shown to exist near the wall after reattachment. Farther downstream the turbulence generation and pressure-strain terms were balanced so that at $x/S=50$ an equilibrium turbulent boundary layer distribution was attained.

With both direct and large eddy simulations, Silveira et al. (1993) investigated the shedding of coherent vortices in the mixing layer in an isothermal two-dimensional and three-dimensional backward step flow. The computations, corresponding to the geometry of Eaton and Johnston's laboratory experiment (Eaton & Johnston, 1980, cited from

Silveira et al. 1993), gave turbulence statistics in better agreement with the experimental data than Smagorinsky's method and K- ϵ modeling. At the near wall region the log law was applied as the boundary condition and inlet flow condition was the profile corresponding to the experimental profile of Eaton and Johnston (1980) superimposed with a white noise of amplitude of $10^{-4} \text{Max} \langle U(y) \rangle$. The Reynolds number of the simulated turbulent flow is 38000 based on the step height.

Table 1: Typical reattachment length for turbulent flows.

Experimental Result (Eaton & Johnston, 1980, Cited from Siveira et al., 1993)	$X_r / S = 7.8$
LES (fine grid, Silveira, 1993)	$X_r / S = 8.1$
K- ϵ model (grid independent result, Silveira et al., 1993)	$X_r / S = 8.1$

Karniadakis et al. (1993) studied the flow over a backward-facing step by re-normalization group (RNG) theory, the results are in fair agreement with the experimental data of Armaly et al. (1983). However some error existed in the order of 8% in the prediction of the reattachment length. It may be caused by the effects of mesh irregularities, inflow boundary conditions and numerical resolution, which need to be addressed as the authors noted.

Durbin (1995) used a K- ϵ - ν model in which an equation was added to the standard K- ϵ model to modify the turbulence velocity scale near the wall. The ν can be regarded as a turbulent intensity scale for the velocity normal to the wall. Turbulent separated flows over a backward step were computed. Compared with experimental

results of Jovic and Driver (1994) (cited from Durbin, 1995) and Driver and Seegmiller (1985), the profiles of the U component of velocity agreed very well inside the separation zone and at the top edge of the step where very strong shear was present. Nevertheless, the model solution for the boundary layer downstream of the reattachment recovered more slowly than that of experimental data. This slow recovery downstream of the reattachment is, as noted by Durbin (1995), who cited Ko (1993), a universal problem of turbulent models shown by Reynolds stress models as well as K- ϵ models. If considering only the mean velocity flow field, the results of Durbin (1995) are quite satisfying.

Jovic and Driver (1995) employed the Laser-Oil Flow Interferometry technique to directly measure the shear stress at the wall over a backward facing step flow. They found that the skin friction coefficient magnitude decreases extensively in the flow as the Reynolds number increases ($Re_h = U_0 h / \nu$, U_0 is the reference velocity upstream the step, h is the step height). By measuring the minimum skin-friction coefficient inside of the re-circulating region, they suggested that the flow near the wall in the re-circulating region is a viscous-dominant laminar-like flow.

Le et al. (1997) studied the turbulent flow over a backward facing step by using the DNS method. The Reynolds number is 5,100 based on the step height and the inlet free velocity. The grid points used were 768, 192 and 64 in the x, y and z directions respectively. The expansion ratio of the step flow channel is 1.2. The reattachment location varies in the span-wise direction and oscillates about a mean value of $6.28 S$, which agreed well with the experimental results of Jovic and Driver (1994, cited in Le et al. 1997). Large negative skin-friction coefficient is found in the re-circulating zone at a relatively low Reynolds number. The velocity profiles in the recovery region fell below

the universal log-law, which indicated the flow is not fully recovered at 20 times step height behind the step. This is similar with the experimental results of Yoo et al. (1992).

1.2 REMAINING PROBLEMS AND GOALS

As shown in the previous section, there are not many results about the flow field in air filter housings and its effects on the filtration efficiency of the filter, and the results are mostly obtained from mean flow field. Because of the complexity of the flows in real filter housings, the interactions between separated flow and the filter have not been studied in depth. A step flow is a proper flow to model the important features in a real air filter housing.

Although a large amount of experimental and numerical data are available now in flows over a backward-facing step, some important problems remain unclear. One of them is how the inlet flow affects the separation flow downstream of the step. In engineering applications, fully developed flow is often difficult to achieve, as bends and abrupt expansions just ahead of the step are sometimes not avoidable. The design of car air-filter housings needs specially to consider the effects of inflow conditions.

Most research of porous media with fluid flows are about either the micro-scale flow inside porous media or the heat and mass transfer of the flows that pass through the media. There are no published results about the interaction between separated fluid flow and porous media that are known to this author. It is important and critical for fine air-filter housing design to understand how the presence of the air-filter can alter the flow field, especially when a significant portion of the flow domain is inside a circulation zone. How and why the velocity and pressure field can be altered by the presence of an air-filter will be studied extensively.

At first the velocity field will be observed without an air filter. The separation lines (where the stream-wise velocity is zero) and velocity distributions will be measured

or computed for different Reynolds numbers. Then the filter will be placed downstream of the step and mounted normal to the side wall. Its position with respect to the reattachment location will be adjusted to study the interaction of the filter and the recirculation flow. In the experiments a filter will be placed at two given locations. The more delicate adjustment of the filter's location with respect to the reattachment position is achieved by adjusting the Reynolds number, since the reattachment position is related to Reynolds number. In computations the filter can be placed at more locations. The velocity and pressure profiles along the surface will be studied. Presently we can not measure the pressure distribution across the filter surface. However the pressure distribution across the filter surface can be handily studied by numerical simulation. When the filter is placed inside the recirculation zone, the flow between the step and the filter is likely separated. The main flow is not normally impinging on the filter since the main flow turns to the step side, in the manner of the dividing streamline shown in Figure 1.2.

For experiments at very low Reynolds number, we were not able to obtain flow that is two-dimensional and at the same time has the seeding particles well mixed with the airflow. Therefore, the experimental results will be presented in the Reynolds number range of 2,000 to 10,000, that is the regime of transitional and turbulent flow.

At very low Reynolds number, the flow is truly two-dimensional, which is the case the present CFD analysis can readily model. In the turbulent regime, the mean flow is two-dimensional, but the turbulence structures are inevitably three-dimensional. A two-dimensional model can predict the main flow field in some extent. Three-dimensional flow needs to be studied for flow structure details in the future. Additionally, with a

three-dimensional CFD model, more sophisticated LES models can be introduced. Numerically, three-dimensional problems will need much more computing power. In this thesis the Low Reynolds number step flow with and without the air filter downstream of the step is numerically studied in great details. The effects of the filter on the separating flow behind the step will be reported. Turbulent flow at Reynolds number of 10000 was simulated with two dimensional LES model, further study is needed for satisfying results.

CHAPTER II

NUMERICAL METHOD

In most engineering problems, flows are turbulent. However still much is unknown about the physics of turbulence. Understanding the mechanism of turbulent flows has been one of the greatest challenges for engineers and scientists for more than 100 years. It is extremely difficult to solve theoretically because of the non-linearity of the governing equations and it is also hard numerically because of the large range of scales involved in turbulent flows, which are mostly of high Reynolds numbers. The purely analytical solutions are not ready for engineering applications. Presently numerical methods still cannot handle the wide range of scales for flows of complex geometry, largely because the near wall region needs very fine grid to solve the shear stresses. Although very high Reynolds number flows can be studied with experiments, as Rogallo and Moin (1984) pointed out, the primary difficulty with experimental turbulence data is the lack of it. Some of the statistical quantities needed for theoretical analysis are difficult to measure, such as those involving the pressure. It is also very hard to measure a flow field over a two-dimensional or three-dimensional domain for time series with good resolutions of space as well of time, even with the powerful PIV (Particle Image Velocimeter) technique. Numerical techniques can provide some qualitative, not very fine but with certain accuracy, velocity distributions over a two or three-dimensional

domain over a time period. Therefore numerical study by some approximation is inevitable for high Reynolds number flows of complex geometry. For low Reynolds number flow, numerical study in many cases costs less and provides more information than experiments. Numerical simulation is more and more popular, especially with the rapid development of computers.

There are three categories of numerical simulation of turbulence. The classical one is the Reynolds stress average, a time average of the Navier-Stokes equations, equations (2.1). Occasionally other types of averaging are used, such as space average. With the whole velocity decomposed as in (2.2), time averaging of the Navier-Stokes equations results in the Reynolds equations (2.3).

$$\frac{\partial u_i}{\partial t} + \frac{\partial}{\partial x_j} (u_i u_j) = -\frac{\partial p}{\partial x_i} + \frac{1}{\text{Re}} \frac{\partial^2 u_i}{\partial x_j \partial x_j} \quad (2.1)$$

$$u = \bar{u} + u' \quad (2.2)$$

$$\frac{\partial \bar{u}_i}{\partial t} + \frac{\partial}{\partial x_j} (\bar{u}_i \bar{u}_j) = -\frac{\partial \bar{p}}{\partial x_i} + \frac{1}{\text{Re}} \frac{\partial^2 \bar{u}_i}{\partial x_j \partial x_j} - \frac{\partial \overline{u'_i u'_j}}{\partial x_j} \quad (2.3)$$

where u is the whole velocity, $u_i, i = 1, 2, 3$ is the velocity component in i -direction. The time averaging procedure and the resultant fluctuating velocity are as follows:

$$\bar{u} = \frac{1}{T} \int_0^T u(t) dt, \quad T \rightarrow \infty, \quad u' = u - \bar{u}$$

Reynolds number is a non-dimensional term defined as $\text{Re} = \frac{\rho UL}{\mu}$. U and L are the

characteristic scales of velocity and length for the flow respectively; ρ is the density and μ is the viscosity of the fluid. The Reynolds equations contain higher order terms that are time-averaged products of the fluctuating fields: Reynolds stresses. One can repeat the

process again on equation (2.3) to obtain equations of the second order moments, which will result in third order moments. This process always ends up producing higher order terms, more unknowns than equations regardless of how many moments one takes. This is known as the closure problem of turbulence.

To close the system of equations, a model or a closure assumption is required, assuming that higher order moments of velocity fluctuations can be expressed as the function of lower order moments. The simplest example is to predict Reynolds stresses by the mean velocity shear, the Boussinesq approach, for example the Prandtl's mixing length. This one is a zero equation or algebraic model, since there are no extra differential equations to solve. The next level of modeling, one-equation model generally employs a differential equation for the turbulent kinetic energy $\overline{u'_i u'_i} / 2$ and a prescribed length scale or dissipation rate. This level is limited by the skill of prescribing the length scale. Two-equation models use one equation for turbulence kinetic energy and one for a length scale or dissipation rate. This type of model has been very popular for Reynolds stresses average methods and one example is the K- ϵ model. The big problem for this method is that it needs several empirical constants, which are different for different flows. Generally it does not work well when the flow involves separations.

Reynolds average models model all scales of turbulence, from the smallest to the largest. Since the large eddies largely depend on the geometry, it is not practical (Ferziger, 1993) to find a universal model for this kind of method. In engineering problems of complex geometry, some specific constants have to be found. For a flow that is totally unknown it is very hard to find appropriate constants for numerical calculations. In the K- ϵ model, since the velocity scale represented by K is not appropriate for

turbulence transport toward the wall, it gives unacceptable results when integrated to a no-slip solid boundary (Rodi et al., 1986 and Durbin, 1995). In the $K-\epsilon-\nu$ model of Durbin (1995) a third equation was introduced to supplement the original $K-\epsilon$ model. It had more constants to manipulate, which can give difficulty if one wants to change the geometry as in the present study.

A second method of numerical simulation is Direct Numerical Simulation (DNS), which is to solve the Navier-Stokes equations directly over a large enough time period and to compute every detail of the flow from the smallest scales to the largest without any modeling. This requires very fine computing grids to solve the small scales and a large computing domain as well to cover the large scales. The DNS is good for accurate prediction but it is too expensive in terms of required computational resources and now only can be a good choice for some simple flows in a small flow region. With computing capacity nowadays, this will not be practical for engineering problems in the near future. For flows over backward facing steps, DNS is now most limited to moderately low Reynolds numbers. In the latest published simulation done by Le et al. (1997) the Reynolds number is 5,100 as described in section 1.2.

A third method is somehow between the above two methods: Large Eddy Simulation (LES). LES offers an approach to mathematically distinguish 'large' and 'subgrid' scale components of a turbulent flow field. The equations for the 'large' scales can be derived by 'filtering' the Navier-Stokes equations, but due to the non-linearity, subgrid scale terms appear and these must be modeled. Filtering is a special average for LES and will be addressed later. The large energy-carrying scales are directly computed. Since the small scales of turbulence tend to be more homogeneous and isotropic than

large ones, it is quite reasonable and possible to have one model for flows of different geometry. Generally LES is not ready for wide applications to engineering problems yet; however for some flows of not very complex geometry at moderate Reynolds number or with some tolerable approximations focusing on some important aspects, LES is a feasible choice. There already are some quite successful applications in flows over backward-facing steps as Silveira et al. (1993) and Karniadakis et al. (1993) up to Reynolds number $Re=38,000$, as mentioned previously in section 1.2.

DNS requires too much computing power for practical engineering problems. Reynolds average methods do not work well for flows with recirculation or at the near wall regions. Therefore LES was used as the numerical model to close the turbulent equations in this study for higher Reynolds number flows. Comparison will be made with existing experimental and numerical results.

2.1 GRID SIZE AND COMPUTING CAPACITY NEEDED

The first step in LES is to define the variables that can be resolved and their governing equations, as Rogallo et al. (1984) pointed out.

The values at discrete mesh points of a simulation represent flow variables only in some average sense. For example the popular 2nd-order center difference formula for the derivatives of a continuous variable gives exactly the derivative of the variable's average over the involved mesh range, that is:

$$\bar{u}|_{x-h_i, x+h_i} = \frac{1}{2h_i} \int_{x-h_i}^{x+h_i} u(\zeta) d\zeta$$
$$\frac{d\bar{u}}{dx} = \frac{d}{dx} \left\{ \frac{1}{2h_i} \int_{x-h_i}^{x+h_i} u(\zeta) d\zeta \right\} = \frac{1}{2h_i} \frac{d}{dx} \int_{x-h_i}^{x+h_i} u(\zeta) d\zeta = \frac{u(x+h_i) - u(x-h_i)}{2h_i}$$

This indicates that a discrete operator filters out scales less than the mesh size h_i . If all the averages give the same values, the direct approach may be applicable. At very high Reynolds number it is hardly appropriate to employ the direct approach (Rogallo et al. 1984). However by explicitly filtering the Navier-Stokes equations, the analyzed scales can be limited to a resolvable size. This formally defines the averaging process that separates resolvable scales from the subgrid scales. Then the SGS (subgrid scale) stresses must be modeled.

If the smallest scale, $O(h)$, that the mesh can resolve is sufficiently smaller than the smallest scale $O(\Delta)$ of the filter and the LES model, the computation results are dependent only on the filter and SGS model and independent of the numerical algorithm. It is still very costly in LES to completely satisfy the above condition, therefore choosing the right mesh size is very important for LES.

In LES the resolution requirements are determined directly by the range of scales one wants to study in detail and indirectly by the accuracy of the model. The less accurate the model, the further the modeled scales must be separated from the scales of interest. In engineering problems the important scales contain the events that are important for the heat and mass transfer or for the production of turbulence energy. In the near wall regions the large-scale coherent structures are the primary events and provide the most turbulence energy production. Simulating the basic mechanisms in the region would require a grid size of five wall units in the span-wise direction and 20 to 30 wall units in the stream-wise direction for a complete resolution as stated in Moin and Kim (1982). On average the coherent structures are about 100 wall units wide in the span-wise and 1000 wall units long in the stream-wise direction for a flat plane boundary layer flow or channel flow. We may choose the computing domain parallel to the wall to cover a whole event and use 64 points in the direction normal to the wall. The total number of grid points for three-dimensional simulation is in the order of $.06 Re_m^2$, $Re_m = U_{max} h / \nu$, h is the half width of the channel (Rogallo et al., 1984). This is quite too large for engineering applications of high Reynolds numbers. However for the present case with the Reynolds numbers less than 20,000, it is feasible to use LES on current computers. If a reliable wall model can be used to decrease the grid resolution required near the wall, the number of grid points could be significantly reduced, and could be low enough for many engineering applications. Silveira et al. (1993) successfully used a $200 \times 30 \times 30$ mesh system to compute by LES a step flow at $Re=38,000$ with the aid of a wall model. Without the wall model, 64 points would be the least needed as mentioned in the previous paragraph for the direction normal to the wall; Silveira et al. used only 30 in that direction.

2.2 LARGE EDDY SIMULATION

2.2.1. Filtering Operation and Basic Equations

In large eddy simulation the large scales are directly computed, and only the small ones are modeled. The filter operation defines the large-scale quantities (indicated by an over bar), which are supposed to be energy carrying.

$$\bar{f}(x) = \int f(x')G(x, x')dx', \quad (2.4)$$

in which G is the filter function and the integral is extended over the entire domain. Filter functions commonly used include the Gaussian, the sharp Fourier cutoff and the top hat (Leonard, 1974, cited from Piomelli, 1993a). One can obtain the filtered set of governing equations by applying the filtering operation to the appropriate governing equations. For incompressible, isothermal flows these are the continuity and Navier-Stokes equations. In dimensionless form and after filtering they are given as:

$$\frac{\partial \bar{u}_i}{\partial x_i} = 0 \quad (2.5)$$

$$\frac{\partial \bar{u}_i}{\partial t} + \frac{\partial}{\partial x_j} (\bar{u}_i \bar{u}_j) = -\frac{\partial \bar{p}}{\partial x_i} - \frac{\partial \tau_{ij}}{\partial x_j} + \frac{1}{\text{Re}} \frac{\partial^2 \bar{u}_i}{\partial x_j \partial x_j} \quad (2.6)$$

Equations (2.5)-(2.6) govern the evolution of the large scales. The effects of the small scales appear in the subgrid-scale (SGS) stresses,

$$\tau_{ij} \equiv \overline{u_i u_j} - \bar{u}_i \bar{u}_j \quad u_i = \bar{u}_i + u_i' \quad (2.7)$$

The SGS stresses are often decomposed into three parts (Leonard, 1974, cited from Piomelli, 1993a): the resolvable part, also known as ‘‘Leonard stresses’’, $L_{ij} \equiv \overline{u_i u_j} - \bar{u}_i \bar{u}_j$; the cross terms, $C_{ij} \equiv \overline{u_i u_j'} + \overline{u_j' u_i'}$, and the SGS Reynolds stresses, $R_{ij} = \overline{u_i' u_j'}$. Most

existing models are eddy viscosity types: assuming the anisotropic part of the SGS stress tensor, $\tau_{ij}^a = \tau_{ij} - \delta_{ij} \tau_{kk}/3$ is dependent proportionally on the large-scale strain rate tensor, \bar{S}_{ij} :

$$\tau_{ij}^a = -2\nu_T \bar{S}_{ij} = -\nu_T \left(\frac{\partial \bar{u}_i}{\partial x_j} + \frac{\partial \bar{u}_j}{\partial x_i} \right); \quad \tau_{ij} = -2\nu_T \bar{S}_{ij} + \frac{1}{3} \delta_{ij} \tau_{kk} \quad (2.8)$$

where ν_T is the SGS eddy viscosity. Equation (2.7) can be decomposed and then each term can be treated differently for a better modeling, however it costs too much and the benefit may not be large enough to justify the practice (Lesieur and Métais, 1996). More and more authors prefer the simple approach to SGS modeling, treating the τ_{ij} as a whole (Ferziger, 1993), which is easy to apply and requires less computation. Although ν_T could be a fourth rank tensor, it is generally assumed to be a scalar quantity as in Reynolds Stress modeling. Then equation (2.6) becomes:

$$\frac{\partial \bar{u}_i}{\partial t} + \frac{\partial}{\partial x_j} (\bar{u}_i \bar{u}_j) = -\frac{\partial \bar{p}_{mo}}{\partial x_i} + \frac{1}{\text{Re}} \left[\frac{\partial^2 \bar{u}_i}{\partial x_j \partial x_j} + \frac{\partial}{\partial x_j} \left(\frac{\nu_T}{\nu} \frac{\partial \bar{u}_i}{\partial x_j} \right) \right] \quad (2.9)$$

$$\bar{p}_{mo} = \bar{p} - \frac{1}{3} \tau_{kk}$$

Here a modified pressure is introduced. This term can be determined by taking the divergence of equation (2.9) with the help of the continuity equation.

The simplest top hat filter will be employed in this paper. Another widely used filter is the Gaussian filter, which is more complicated. The formula of a top hat filter applied to non-uniform mesh systems is given in Appendix A.

2.2.2 Smagorinsky's Eddy Viscosity Model

LES was first applied by Deardorff (1970), who used the eddy viscosity model introduced by Smagorinsky (1963), as reported by Ferziger (1993). By assuming that the

small scales are in equilibrium and that energy production and dissipation are in balance, this yields:

$$v_T = (C_s d)^2 (2\overline{S_{ij}}\overline{S_{ij}})^{1/2} = (C_s d)^2 |\overline{S}| \quad (2.10)$$

where d is the length scale associated with typical SGS eddy and C_s is the single model parameter. A number of arguments based on some fundamental considerations suggest that the length scale be (Ferziger, 1993):

$$d = (L\Delta^2)^{1/3}$$

where L is the integral length scale of the turbulence and the Δ is the length scale used in the filter. However the integral length is difficult to compute, in most cases Δ is used as the length scale d . When the flow is anisotropic, the most common choice is

$$d = \Delta = (\Delta x_1 \Delta x_2 \Delta x_3)^{1/3}$$

where the Δx_i is the filter width in the i -th direction and usually it is the mesh size (Piomelli, 1993a).

Although many new subgrid scale models have been developed, the Smagorinsky model is still successfully and widely used, such as the recent LES applications of homogeneous shear stratified simulation by Kaltenbach et al. (1994) and a backward step flow by Arnal and Friedrich (1993); reported by Lesieur et al. (1996). The value of the parameter C_s predicted by theories (about 0.2) does a good job for isotropic turbulence, since the theories are based on isotropic flows. For inhomogeneous shear flows, many authors have used values that are half of 0.2 or less. Deardorff (1970) used .0094 as C_s . It is still not clear why C_s should be smaller for inhomogeneous shear flows, although it appears to be related to the backscatter (energy transfer from small scales to large scales)

in flows with mean shear (Ferziger, 1993 citing McMillan et al., 1980). It is reported by Lesieur et al. (1996) citing Friedrich and Nieuwstadt, (1994) that using the Smagorinsky model, there were problems in reproducing the experimental data, due to their inability to predict the energy transfer mechanism at the wall. In particular, Lesieur and Métais (1996) further noted that it does not work for transition in a boundary layer over a flat plate for flows that start with a laminar profile to which a small perturbation is added. Due to excessive eddy viscosity coming from the mean shear the flow remains laminar when the Reynolds number is in the transitional regime.

By considering the transport equation for the resolved kinetic energy $\bar{q}^2 = \frac{\bar{u}_i \bar{u}_i}{2}$;

we can see the principle effect of the SGS model on the resolved scales (Piomelli, 1993a):

$$\frac{\partial \bar{q}^2}{\partial t} + \frac{\partial(\bar{q}^2 \bar{u}_j)}{\partial x_j} = \frac{\partial}{\partial x_j} (-2\bar{p} \bar{u}_j - 2\bar{u}_i \tau_{ij} + \frac{1}{\text{Re}} \frac{\partial \bar{q}^2}{\partial x_j}) - \frac{2}{\text{Re}} \frac{\partial \bar{u}_i}{\partial x_j} \frac{\partial \bar{u}_i}{\partial x_j} + 2\tau_{ij} \bar{S}_{ij}$$

$2\tau_{ij} \bar{S}_{ij} = \epsilon_{\text{SGS}}$ is the SGS dissipation, representing the energy transfer between resolved and subgrid scales. If it is negative, the subgrid scales remove energy from the resolved ones (forwardscatter). If it is positive, the subgrid scales give back energy into the resolved scales (backscatter). In most three-dimensional engineering problems, turbulence energy transfers from the large to the small scales on average. In the eddy viscosity model:

$$\tau_{ij} = -2\nu_T \bar{S}_{ij}, \quad \epsilon_{\text{SGS}} = -2\nu_T \bar{S}_{ij} \bar{S}_{ij} = -2\nu_T |\bar{S}|^2.$$

As long as the eddy viscosity is non-negative, there is no backscatter and the model is said to be 'dissipative' since it is always providing dissipation.

Clark et al. (1979, cited from Piomelli, 1993a), using DNS results to test the LES models, found that eddy viscosity models of the Smagorinsky type predicted the global energy transport from large eddies to small scales with acceptable accuracy, but failed to predict the local stresses. However the Smagorinsky model was fairly good for homogeneous flows. Kaltenbach et al. (1994), reported by Lesieur et al. (1996), compared their Smagorinsky model results with DNS and experimental data. The results were very good. When the same mesh resolution was used as DNS, better results were obtained by the Smagorinsky model than DNS. This indicates that when mesh resolution is not fine enough for DNS, modeling can provide better computation results.

There are many more complicated LES models, such as the Dynamic Eddy Viscosity model (Piomelli, 1991). Those models are not very popular in engineering applications yet since the models are not as easy to use as the Smagorinsky model.

2.2.3 The Wall Region

In the wall region, all the turbulent structures are small, even the energy-carrying structures. The velocity gradients are very steep. Very fine grids are needed to simulate the wall region if natural non-slip boundary conditions are applied. It is well known that the shear flows near solid boundaries contain alternating streaks of high and low speed fluid, which are very thin and active in turbulence energy production. If they are not adequately simulated, the turbulence energy production in the vicinity of the wall (which is a large fraction of the total energy production) is under-predicted (Kim and Moin 1986). Then some of the overall parameters of the flow will not be predicted correctly.

However some simulations suggest that wall-region turbulence and turbulence far from the wall are relatively loosely coupled. Chapman and Kuhn (1986) showed that a

simulation in the wall region displayed most of the characteristics of the wall layer found in a simulation that computed the entire flow. They put artificial boundary conditions at the top of the buffer layer (at approximately $y^+=100$). This indicates that accurate prediction of the flow near the wall does not require accurate simulation of the outer flow. On the other hand, Ferziger (1993) noted that Piomelli et al. (1987) and others had shown that by using relatively crude lower boundary conditions to represent the effect of the wall region, one could accurately simulate the central part of the flow in a channel. That implies that the outer region flow can be simulated without knowing the details of the flow in the wall region. Therefore it is possible either region can be well simulated if the correct shear stress and a reasonable approximation of the fluctuations are given at the interface between it and the other zone.

These results suggest that useful simulation can be done without resolving the entire flow. This is important because a very fine grid in every direction is required to resolve the wall region. If a model can represent the stresses in the wall region, it may result in huge savings, which makes it possible to extend LES to practical engineering applications. This approach allows one to place the first grid point in the logarithmic region ($y^+=50 - 200$, Piomelli et al., 1989), and there is no need to resolve the wall region. The subgrid scale turbulence structures in the core region are more isotropic and easier to model.

A still widely used wall region model was first introduced by Deardorff (1970) and then modified by Schumann (1975). It assumes that the instantaneous velocity at the first grid point from a wall is exactly correlated with the wall shear directly below it:

$$\tau_w(x, z) = \frac{\bar{u}_1(x, y_1, z)}{U_1(y_1)} < \tau_w >$$

where y_1 is the first grid point from wall, $\langle \tau_w \rangle$ is the mean wall shear stress and $U_1(y_1)$ is the mean velocity at the first grid point, determined by the log law from Deardorff (1970). The boundary condition for the velocity normal to the wall is impermeable. The mean wall stress was set to be equal to the driving pressure gradient for channel flow, as in Schumann (1975) who obtained considerably improved results. Due to the way the wall stress is computed, the model is limited to flows for which the pressure field is previously known.

Mason and Callen (1986) assumed the conventional logarithmic law velocity profile near the wall instead of the log law of Deardorff (1970). We know that the logarithmic law holds true only as the mean velocity profile, not locally and instantaneously. Citing Piomelli et al. (1987), Ferziger (1993) found it inadequate for engineering applications. Piomelli et al. (1989) used direct simulation results to test models for the wall layer and constructed two new models based on boundary layer research results of both experiments and direct simulations.

The first model of Piomelli et al. (1989) was derived from the idea that Reynolds stress producing events at near the wall region move away from the wall at a small angle to the wall, not vertically as assumed by Schumann (1975). This leads to the so-called shifted model, an improvement of Schumann's:

$$\tau_w(x, z) = \frac{\bar{u}_1(x + \Delta_s, y_1, z)}{U_1(y_1)} \langle \tau_w \rangle$$

where $\Delta_s = y_1 / \cos 8^\circ$ is a spatial shift, 8° is the observed mean angle of event trajectories.

The second model of Piomelli et al. (1989) is based on the observation that events

containing significant Reynolds stresses involve vertical movement, so that it is the vertical component of the velocity rather than the horizontal one that should be correlated with the wall shear stress.

$$\tau_w(x, z) = \langle \tau_w \rangle - Cu^* \bar{V}(x + \Delta_s, y_1, z)$$

Both these models gave improved results that agreed better with experiments and direct simulations for channel flow, including cases with transpiration from the walls and high Reynolds number flows.

All these models mentioned above have been applied only to flow over flat walls with very mild pressure gradients. They are almost certainly inadequate for separated flows or flows over complex-shaped walls. Ferziger (1993) pointed out that no reliable simulations of fully turbulent flows in complex geometry have yet been modeled. Because experimental data are scarce and lack detail, the development of trustworthy methods for simulating these flows will probably require simulation with non-slip conditions. However Silveira et al. (1993) used the conventional log law in the near wall region for separated step flow and the results were quite good.

For the flow inside the separation zone or near the reattachment location, the mean velocity in the wall region is not truly boundary layer like flow. Another problem is that the pressure gradient in the separated flow region is very different from those of straight pipe flow or flat plate boundary layer flow. If the log law applies here, different parameters of the law may need to be found accordingly. Discrepancy from the universal law does exist in the velocity profiles at reattachment location as reported by Yoo et al. (1992). Silveira et al. (1993) believed that using the log law profile does not introduce a significant error in the development of the turbulent flow in the shear layer just

downstream of the step and the recirculation region away from the immediate vicinity of the wall. In most parts of the flow domain, the flow characteristics are largely controlled by the inflectional instabilities close to the entrance, where the velocity profile is very unstable.

2.3 INLET CONDITIONS AND OUTLET CONDITIONS.

To limit the number of the computational grid points, the inlet channel is not simulated. The inflow conditions are imposed at the step ridge corresponding to measured experimental data. For laminar flow at low Reynolds numbers, a parabolic profile will be used. For turbulent flows the inflow will consist of a mean velocity field on which a white noise is superimposed with a given magnitude as the fluctuating velocity. The mean velocity profile is a fourth order polynomial to match the measured velocity profile for the Reynolds number. It is reported by Silveira et al. (1993) that precisely matching the experimental inflow fluctuating conditions, demonstrated by Arnal and Friedrich (1993), is very difficult. Synthetic white noise with a uniform probability distribution therefore will be introduced, as did Silveira et al. (1993).

At the outlet, the longitudinal velocity gradient will be set to zero, the fully developed condition. When the air filter is present, the outlet condition will not affect the upstream flow very much due to the very high resistance of the filter. For the cases without the filter, the outlet will be placed far from the region of interest to let the flow recover from the re-circulation. In most cases the outlet condition will be applied at 30 step heights behind the step. Since the current emphasis is on the interaction between separation flow and the presence of a filter, there is no need to simulate precisely the recovering flow downstream. According to the experiments of Yoo et al. (1992) and the computation of Silveira et al. (1993), 30 step heights away from the step are quite enough. Le et al. (1997) also applied the outlet conditions at 30 times step heights downstream of the step at $Re=5,100$ in their direct numerical simulation.

2.4 FINITE DIFFERENCE SCHEME

2.4.1 Equations for Pure Fluids

For laminar flows, the governing equations are the Navier-Stokes equations. The equations for turbulent flows with LES models are similar and can be solved by the same numerical method. The procedure therefore will be developed upon the non-dimensional Navier-Stokes equations.

$$\frac{\partial u_i}{\partial t} + \frac{\partial p}{\partial x_i} = H_i + \frac{1}{\text{Re}} \frac{\partial^2 u_i}{\partial x_j^2}$$
$$H_i = -u_j \frac{\partial u_i}{\partial x_j} = -\frac{\partial}{\partial x_j} (u_i u_j)$$

The two-step time-split method is used. The first step is to split the velocity into the sum of predicted and corrected values. The predicted velocity is determined by time integration of the momentum equation without the pressure term.

$$\hat{u}_i^{n+1} = u_i^n - \Delta t \left[\left(\frac{3}{2} H_i^n - \frac{1}{2} H_i^{n-1} \right) + \frac{1}{2\text{Re}} \frac{\partial^2 (\hat{u}_i^{n+1} + u_i^n)}{\partial x_j^2} \right] \quad (2.16)$$

The viscous term is treated by Crank-Nicholson scheme and the convective term by an Adams-Bashforth scheme (Kim et al. 1985, Ku et al. 1989). Then it is second order accurate in both time and space. The first order temporal approximation has an error term which is diffusive. This may cause problems for the LES model since an extra numerical diffusion term is introduced.

The second step is to develop the pressure and corrected velocity fields that satisfy the continuity equation by using the relation:

$$u_i^{n+1} = \hat{u}_i^{n+1} - \Delta t \frac{\partial \phi}{\partial x_i} \quad (2.17)$$

$$\frac{\partial u_i^{n+1}}{\partial x_i} = 0 \quad \frac{\partial^2 \phi}{\partial x_j \partial x_j} = \frac{1}{\Delta t} \frac{\partial \hat{u}_i^{n+1}}{\partial x_i}, \text{ and } p = \phi + (\Delta t / 2 \text{Re}) \frac{\partial^2 \phi}{\partial x_j \partial x_j}$$

The pressure is found by taking the divergence of equation (2.17) and by invoking the incompressibility continuity condition. This results in the Poisson equation that is going to be solved by an over-relaxation iteration method. With the second-order staggered finite difference scheme (Harlow, F. H. et. al. 1965), the need for pressure boundary conditions does not arise. The continuity equation at the interior cells together with the momentum equations (at the interior grid points) and the velocity boundary conditions, leads to a closed system of algebraic equations for pressure.

Details about how to apply the above schemes to the equations (2.5) and (2.9) for turbulent flows are in Appendix C.

2.4.2 The Flow within the Air-Filter

The flow inside the air filter is treated as laminar flow, since its Reynolds number is less than one if the characteristic length is taken as the diameter of the fibers of which the filters are made. For simplicity the filter will be considered as a homogeneous porous medium and an extended Darcy's law will apply. The equations for the porous medium are (Chen and Chen, 1992):

$$\nabla \cdot \mathbf{u}_m = 0$$

$$\rho_o \left(\frac{1}{\phi_m} \frac{\partial \mathbf{u}_m}{\partial t} + \frac{B}{K} |\mathbf{u}_m| \mathbf{u}_m \right) = -\nabla p_m - \frac{\mu}{K} \mathbf{u}_m + \frac{\mu}{\phi_m} \nabla^2 \mathbf{u}_m$$

In the equations the subscript m denotes quantities pertaining to the porous medium and u_m denotes the filtration velocity. Where ϕ_m is the porosity, K is the permeability and

two additional terms have been included in Darcy's equation. One is the Brinkman term $\frac{\mu}{\phi_m} \nabla^2 u_m$ to account for the viscous effect. This term is important in the neighborhood of solid boundaries and interfaces where viscous shear is strong. The Forchheimer term $\frac{B}{K} |u_m| u_m$ takes into account the inertial effects when the filtration velocity becomes large. The coefficient B is independent of the properties of the fluid, but depends on the properties of the medium. It will be determined from the experimental data of Tebbutt (1995) who worked on the same filters that are used in this research. The flow domain including the regions with and without air filters will be solved simultaneously. At the interfaces the boundary conditions are the continuities of velocity, shear stresses and normal stress (Chen and Chen, 1992). For the two-dimensional case:

$$\begin{aligned} v &= v_m & \mu \frac{\partial v}{\partial x} &= \mu \frac{\partial v_m}{\partial x} \\ u &= u_m & p + 2\mu \frac{\partial u}{\partial x} &= p_m + 2\mu \frac{\partial u_m}{\partial x} \end{aligned}$$

The subscript m presents variables inside the filter. The coordinates are shown in Fig. 2.1.

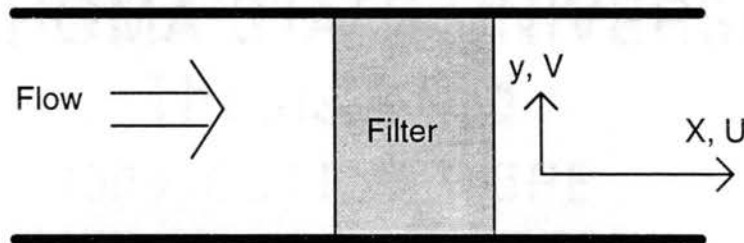


Figure 2.1. The placement of the filter in the flow domain.

The static pressure at the interface should be the same at both sides, that is $p = p_m$. Since the flow inside the filter is considered laminar, at the interface, the eddy viscosity should be zero. Hence the viscosity there is constant. Then we have:

$$v = v_m \quad \frac{\partial v}{\partial x} = \frac{\partial v_m}{\partial x} \quad \text{and} \quad u = u_m \quad \frac{\partial u}{\partial x} = \frac{\partial u_m}{\partial x}$$

The velocity outside of the filter will be the velocity of the LES filtered field. At the solid boundary non-slip conditions apply.

To compute the entire flow field simultaneously, we need to apply the time-split method to the equations of the porous medium. Although the equations for porous media are different from the Navier-Stokes equations for pure fluids, they are similar in the basic forms. Some modifications are necessary. The porosity affects the relation between velocity and the pressure gradients and the term for inertial effects caused by the porous medium. Therefore the inertial term in the numerical method will have two terms here to make the resultant equations have the same form. The same length and velocity characteristic scales as for the pure fluid are used to normalize the equations for the porous medium. The details can be found in Appendix F.2. Then the non-dimensional equations are the following, where the bar represents normalized terms:

$$\frac{\hat{u}_{mi}^{n+1} - u_{mi}^n}{\Delta t} = \frac{1}{2}(3H_i^n - H_i^{n-1}) + \frac{1}{2\text{Re}} \nabla^2 (\hat{u}_{mi}^{n+1} + u_{mi}^n)$$

$$H_i^n = -\phi_m \left(\frac{\bar{B}}{\bar{K}} |u_{mi}^n| + \frac{1}{\text{Re} \bar{K}} \right) u_{mi}^n$$

And the Poisson equation for pressure will have changes as follows:

$$\text{Let } \frac{u_{mi}^{n+1} - \hat{u}_{mi}^{n+1}}{\Delta t} = \phi_m \nabla \varphi^{n+1} \text{ and we have } \nabla \bullet u_{mi}^{n+1} = 0.$$

$$\text{Then: } \phi_m \nabla^2 \varphi^{n+1} = (\nabla \cdot \hat{u}_{m_i}^{n+1}) / \Delta t \text{ and } p_m = (1 + \frac{\Delta t}{2\phi_m \text{Re}} \nabla^2) \varphi$$

The porosity has to be taken into consideration for the relation between pressure gradient and the velocity. Then we yield the same form of equations and the same CFD procedure to solve the flow inside the porous medium as for the pure fluid. The entire flow field now can be treated as one by the same governing equations numerically and be solved simultaneously. However since the coefficients are different at the right side of the Poisson equations for pressure and the continuity conditions at the interface, the entire flow domain is divided into three divisions as pure fluids, porous medium and pure fluids again. All the coefficients of the numerical equations are computed respectively for the three domains and the two interfaces between them. At the interfaces the relations are steady state, therefore they are very easily combined into the whole procedure. Then the entire flow domain is solved at the same time. More details can be found in Appendices E and F.

CHAPTER III

EXPERIMENTAL SETUP AND MEASUREMENT TECHNIQUES

3.1 TWO DIMENSIONAL STEP FLOW

Step flow is a good prototype for separation and turbulence research and it is a simple model to simulate some important aerodynamic features of a real automotive air-filter housing. A transparent model has been constructed for LDA measurement and flow visualization. It is an open air-driven flow channel which incorporates a two dimensional backward-facing step, as shown in Figure 3.1. The expansion ratio is 1:2 with the large channel 50 mm in height and an aspect ratio of 10:1 to ensure a two-dimensional mean flow field. The airflow passes through a 25-mm thick regular air filter to enter a mixing chamber. The solution of seeding particles, the concentration of which is approximately 400 ppm, is introduced through a vertical pipe of 100 mm in diameter by a TSI 9306 atomizer into the mixing section of the wind tunnel. The atomizer produces water droplets together with the particles. Since the water droplets are not good particles for LDA measurement and may condense on the wall of the tunnel or on the filter to cause problems, the air is heated slightly to remove the water droplets. The particles have a very small speed at the exit of the pipe; therefore it has little effect on the flow. The particles are very small, .5 to 1 micrometer, of which the density is very close to water. They are very well mixed into the airflow at the developing chamber when the mean

velocity in the chambers is larger than .1 m/s. The mixing chamber is about .75 meters long to let the flow develop. The sedimentation velocity of the particles is very small; approximately 3×10^{-5} m/s compared with the .4 m/s mean velocity inside the test section. It has virtually no effect on the flow field. Details will be discussed in section 3.2. Then the seeded airflow is fed through flow straighteners and two screens. To maintain a uniform and non-separated flow upstream of the step, a contraction nozzle was designed and built based on the formula of Morel (1977). The curve and the parameters are shown in Fig. 3.2. The inlet to outlet area ratio is 10. The outlet nozzle is connected to the inlet of the test section. The first part of the test section is 25 mm high and .5 meter long to provide a fully developed inlet flow for the step.

An air filter can be placed either at 4.25 or 6.75 times the step height downstream of the step, normal to the side wall. The separated flow downstream of the step when the filter is not present was first observed and will serve as a comparison base. Then the filter is added to the flow field at the positions either inside the separation zone or outside the separation zone. Since the reattachment location is a function of Reynolds number for a large range of Reynolds numbers, we can control the filter's position relative to the reattachment location by changing the Reynolds number, that is, changing the flow rates. The flow rates are adjusted by regulating valves available in the blower control system and monitored by a TSI 2-21 mass flowmeter.

Two-Dimensional Backward Facing Step

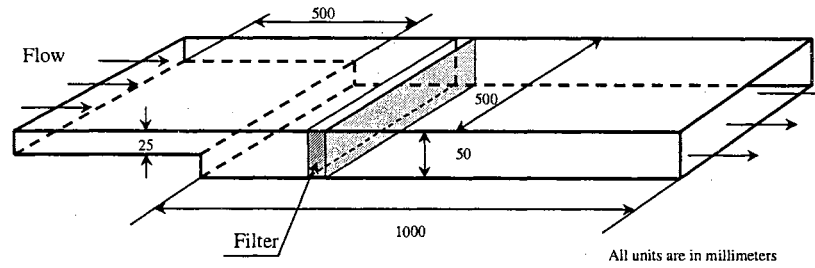


Figure 3.1. Step flow test section of the experimental set up, expansion ratio 1:2.

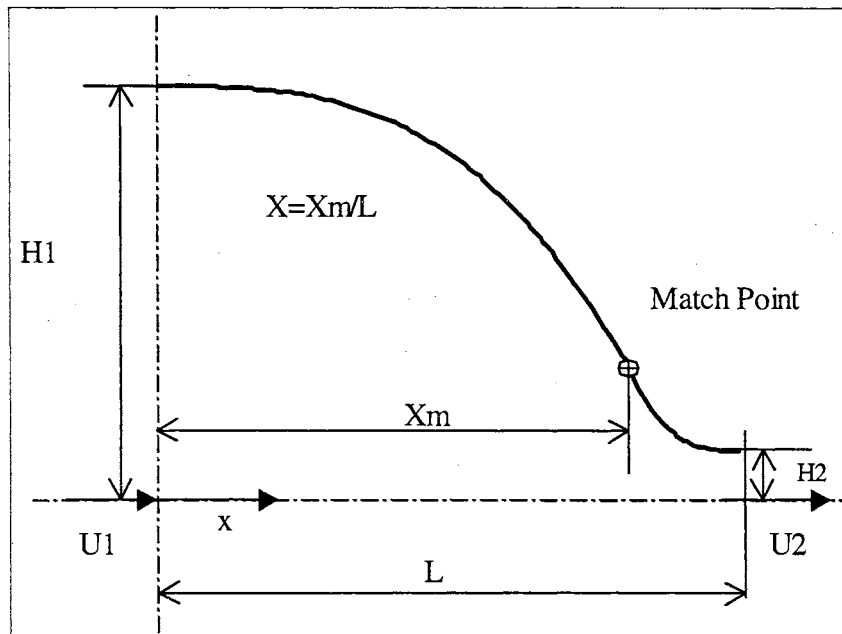


Figure 3.2. Contraction curve of the channel inlet nozzle and its parameters.

Because of the reversing flow behind the step, the main flow is not parallel to the side wall close to the step. When the filter is inside the separated flow zone, the mean flow is not impinging normally on the air filter. The Reynolds number can be adjusted between 5,00 to 10,000 by changing the mean velocity, covering both the laminar and turbulent regimes. The LDA technique was used to measure the instantaneous velocity throughout the flow domain. Measurements were conducted at .5 step height (12.5 mm) away from the surface of the filter. Since the velocity measured is normal to the surface of the filter, the effective velocity to drive particles through the air filter then can be obtained. The entire experiment setup is shown in Figure 3.3.

Contraction design is centered on finding the optimum wall shape and the minimum nozzle length for a given purpose. A short nozzle tends to have higher acceleration that leads to thinner boundary layer at the throat. However if it is too short the exit flow may not be steady or have thick boundary layers due to its tendency to separation. A good wall shape produces uniform exit flow without separation. Morel (1977) provided charts of one-parameter family of wall shapes for two-dimensional wind tunnel contractions. The shapes were based on two cubic arcs and were developed using inviscid flow analysis and separation criteria. The two cubic functions are:

$$\frac{H - H_2}{H_2 - H_1} = 1 - \frac{1}{X^2} \left(\frac{x}{L} \right)^3 \dots\dots\dots x/L < X$$

$$= \frac{1}{(1 - X)^2} \left(1 - \frac{x}{L} \right)^3 \dots\dots\dots x/L > X$$

The curves and the parameters are shown in Figure 3.2. The exit of the contraction was given by the test section's inlet. The contraction ratio is usually specified due to other considerations such as the size of the channel upstream of the contraction. In the present

design the contraction ratio CR was chosen as 10. With H_1 and H_2 known, the parameters left for design is the nozzle length and the shape parameter X .

As stated in Morel (1977), since all the wall shapes are specified by a single one-parameter X , all the wall pressure distributions and the velocity profiles in the end zones are quite similar for all the shapes in the family. Then it is quite enough to avoid flow separation by choosing the appropriate values of the two wall-pressure coefficients defined as

$$C_{pe} = 1 - (U_{2,\infty}/V_e)^2 \quad C_{pi} = 1 - (V_i/U_{1,\infty})^2$$

where V is the wall velocity (this is inviscid analysis, velocity at the wall is not zero), i and e refer to the point of maximum and minimum velocity respectively. For different purposes the two coefficients are different. Morel (1977) found that the non-uniformity velocity is $\tilde{u}_2 = .19C_{pe}$. If $C_{pe} = .05$, the non-uniformity will be less than 1%. To avoid separation in the exit of the nozzle, Morel suggested that $C_{pi} = .16$ for laminar flow. Since turbulent flow is less likely to separate compared with laminar flow; the value for laminar is chosen for the present design. With the two coefficients known, two parameters could be found in a chart provided in Morel, which are $F_i = .72$ and $F_e = .18$.

Then we have

$$X = \left(1 + \frac{1}{m} (F_i / F_e)^5 \right)^{-1} \quad m = \frac{H_1}{H_2}$$

$$F_i = \frac{m-1}{m} X^{-2} (L/H_1)^{-3}$$

The equations above yield $X = .83$ and $L/H_1 = 1.22$. This completes the contraction design. The flow channel and LDA system are shown schematically in Figure 3.3.

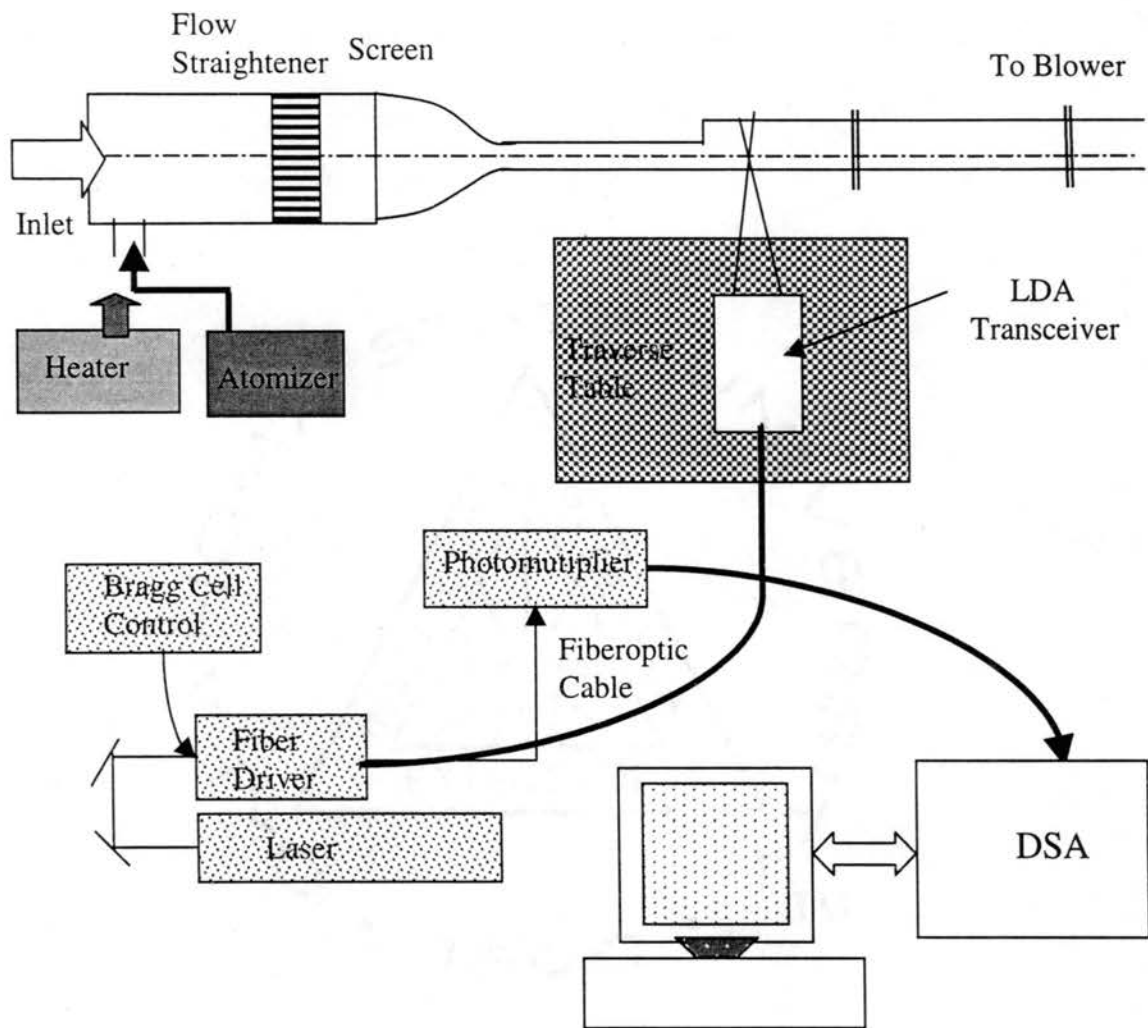


Figure 3.3. Schematic of apparatus and instrumentation.

3.2 LASER DOPPLER ANEMOMETER

The LDA system used to measure the velocity was an Aerometrics, Inc. two-component fiber optic system. Doppler signals are processed by a Doppler Signal Analyzer (DSA) using Fast Fourier Transforms (FFT). A Coherent Innova 70-A 4-watt argon ion laser provides the four laser beams. One pair of the beams is green and another pair is blue, the two pairs measure two velocity components respectively. The frequency of one beam in each pair is shifted 40 MHz by a Bragg cell, this enables us to measure velocity in reversing flow regions.

A fiber optic transceiver focuses the system's four beams at a 500 mm focal point, producing a probe volume that is 737 μm long and 66 μm in diameter. The measuring point is located at the crossing point of the four beams. When a moving particle passes through the measuring volume, it scatters light to all the directions. The forward direction, the direction of the laser beams travel, has the strongest scattering light while the backward direction has relatively weak light. The backward scattering light is collected by the transceiver lens and then transmitted to two photomultipliers through a fiber optic cable. The backward-scatter mode is designed so that the beam transmitting and scattered light collecting can be at one probe, and thus can be at one side of the test section. This mode does not require two sides of the test section to be transparent and is much easier to arrange the setup and to move the probe. The scattered light has two colors and the two photo-multipliers process the light respectively by its color and transform the light Doppler signals into analog electronic signals. Then the electronic signals, which carry the Doppler signals, are analyzed by the two-channel DSA and Doppler frequencies with respect to two velocity components are found by the FFT

method. The FFT method can pick up the Doppler frequencies even when the signal to noise ratio is as low as -5 dB. This is critical to getting the right measurement when the measuring point is close to a wall or in a recirculating flow region where noise could be very strong.

LDA has three distinguishing features. One is that the relation between the velocity and the Doppler frequency is theoretically given once the system's optical configurations are given, regardless of the room temperature or humidity. There is no need of calibration. Another one is that in most cases it has nearly no direct effect on the flow field. The third feature is that it measures the velocity components directly and independently. Practically there is no effect of the velocity components in other directions on the measured component. This is critical when we measure velocity in the recirculation area where the velocity direction is hard to know a priori and may be in any direction. However LDA requires transparent wall and media at the measuring area and it needs seeding when the measured medium is clear.

The flow medium is air and seeded with $.966 \mu\text{m}$ or $.505 \mu\text{m}$ diameter polystyrene latex particles in an approximate 400 ppm solution in water by a TSI model 9306 atomizer. The density of the latex particles is 1.05 g/cm^3 , which is very close to the density of water so that little sedimentation may happen in the atomizer. The particle solution is introduced to the entrance flow upstream of the contraction and heated slightly to remove or significantly reduce the sizes of the water droplets. The setup for seeding is shown as part of Figure 3.3. If the density of the seeded particles is the same as the flow medium, the particles can follow the flow motion precisely. However the current seeded particles have far larger density than the flow medium. Then two issues need to be

addressed.

First, can the particles follow the airflow? Since the step flow is not steady state and large fluctuations exist, we need to see how fast the particles can respond to the ambient flow changes. The standard way is to examine the step response time constant, which is, for very small particles ($Re \ll 1$) and particle density much larger than the flow medium:

$$t_1 = \frac{\rho_p d_p^2}{18\mu_f}, \quad \rho_p / \rho_{air} \approx 900$$

where ρ_p is the particle density, d_p is the particle diameter and μ_f is the fluid viscosity.

The frequency response, indicating how fast the particles can follow the flow motion, is:

$$f = \frac{1}{2\pi t_1}.$$

For the current particles, $d_p = .996\mu m$, $t_1 = 3\mu s$, $f = 52kHz$. For most incompressible turbulent flows the cut off frequency is less than 10 kHz. This implies that the particles can follow even the fastest changes in the flow motions. A second issue about the seeded particles is the sedimentation of the particles. The maximum falling velocity is referred to as the settling velocity, which is computed by the equilibrium of the particle weight, buoyant force and the drag for a sphere with very slow motions:

$$V_s = \left[\frac{4(\rho_p - \rho_f)gd_p}{3\rho_f C_D} \right]^{1/2} \quad (3.1)$$

The particles used here are spheres. Since the particles are very small and the velocity is likely small too, the Reynolds number is very small and then the drag coefficient C_D can be determined by the equation (Schlichting 1975):

$$C_D = \frac{24}{R} \left(1 + \frac{3}{16} R\right), \quad \text{for } R = \frac{V_s d_p}{\nu} \leq 5 \quad (3.2)$$

Substituting (3.2) into (3.1) yields:

$$V_s = 2.95 \times 10^{-5} \text{ m/s}, \quad R = 1.96 \times 10^{-6}$$

for $1 \mu\text{m}$ particles. The settling velocity is negligible since the mean velocity is about .4 m/s in the test section for the lowest Reynolds number. For $.5 \mu\text{m}$ particles the settling velocity will be even smaller according to the equations (3.1) and (3.2). Their ability to follow the flow motion will be better. Then we can conclude that the particles introduced into the flow can follow the flow motion very well and their sedimentation has no practical effects on the flow field and the LDA measurements.

The measuring position is adjusted by moving the transceiver probe. The fiber optic cable and the backward-scatter mode make the moving much easier. The transceiver probe is mounted on a three-direction traversing table with motion provided by stepping motors under computer control. The whole setup is shown in Fig. 3.3. Since the flow inside the housing is not uniform and a large portion is reversing flow, the seeding is not uniformly distributed either. The wall that the laser beams pass through may have some moisture or fine dust on some spots so that the wall conditions may vary a bit at different locations. When measuring points close to the wall, the background light, mainly reflecting from the wall, makes the signal to noise ratio of the Doppler signal much smaller compared with the core region. For all the reasons above the signal processing parameters of the LDA need to be adjusted as the measuring point was moved in the flow field. Therefore the data rates and validation rates were varied in different regions of the flow field. In order to obtain consistent velocity measurement across the

flow field, all measurement results presented here were obtained from the average of 500 validated samples. As tested by Newman (1995), the LDA system can yield an accuracy of 1%, which is adequate for the present research. No bias corrections were applied to the measurements. As stated by Adams and Eaton (1988) the velocity bias of LDA measurements is negligible when the mean velocity is very small. In this thesis the most important measurements were performed around the separation line of the step flow, where the mean velocity is close to zero. For the velocity profiles measured upstream of the filter, the bias would have similar effects on the profiles with and without the filter. Therefore the velocity bias is not a concern for this thesis. At low Reynolds number when the velocity is very small, the sampling rates of the LDA can be as high as 200 valid data per second, which implies the total sampling time would be as small as 2.5 second for 500 valid data. That time appears not sufficient to compute an accurate time average for the flow with the step height of .025 meter and the average velocity across the channel of .4 m/s. Therefore the data rates were voluntarily reduced by lower the laser power or the high voltage of the photo-multipliers so that the total time to collect 500 validated samples would incorporate some low frequency fluctuations. In most cases the total sampling time was controlled between 20 to 60 seconds.

3.3 ACTUAL AUTOMOTIVE HOUSING

A model to investigate the flow field upstream of the filter inside a real automotive air filter housing was built based on an actual air-filter housing of a Chrysler minivan. The model has the size of the real one. The part downstream of the filter and the inlet pipe were the original parts of the real housing and the upstream part is made of transparent plastic. Its geometry is schematically shown in Figure 1.1. To measure the velocity normal to the filter surface, the model has to be mounted in a way that the optical axis of LDA transceiver is in line with the plane of the filter. Since the housing is not rectangular, its side walls are not normal to the filter plane, and consequently the four LDA beams may not be able to focus exactly on the same point since the refraction of the tilted wall is not symmetrical. The thickness of the wall and the angles between the wall and the optical axis of the LDA transceiver are the two main factors in this matter. However the angles are given since the real housing provides the geometry of the model. Therefore we need to determine the wall thickness to make the distance between two focused points close enough to be considered as one point.

The LDV used in this study is a four-beam system to measure two velocity components. A typical 4-beam system is as shown in Figure 3.4.

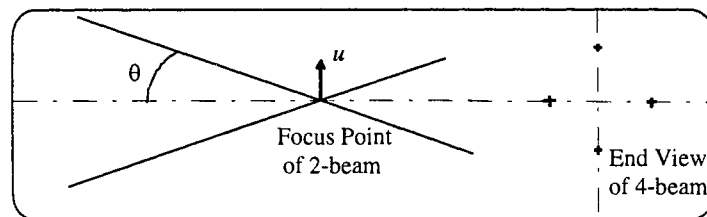


Figure 3.4. Set up of the four-beams of a two dimensional LDA

The model shown in Figure 1.1 has tilted walls at all sides, so the wall can not be normal to the optical axis, which is horizontal given by the way the LDA transceiver is mounted for measuring the vertical velocity component. Since the four beams come into the transparent wall from different angles, the focus point of the horizontally arranged beams is not the same as the focus point of the vertically arranged beams. This means that the vertical velocity component, measured at the focus point of the two vertical beams, is not precisely at the same point as the horizontal velocity component is measured.

The shift distance between the two focus points is a function of the wall tilt angle α , the half angle between two beams θ and the thickness of the wall, given the refraction index of the wall. The present θ was about 4.5 degrees and α was about 35 degrees. Refraction index n for the transparent wall was 1.5. The wall was 2.5mm (0.1 inch) thick. Thus the two focused points were 1.2 mm apart. For a filter with upwind surface of 114 mm by 170 mm the difference in measuring points is reasonably tolerable. The error is not critical since u and v are analyzed separately. Reynolds stress was not measured. The derivation of the calculation can be found in Appendix G

CHAPTER IV

FLOW FIELD OF AN ACTUAL AUTOMOTIVE AIR FILTER HOUSING

Two components of the velocity field in the model automotive air filter housing, shown in Figure 1.1, are measured by the LDA techniques. The two velocity components are u and w , which are parallel and perpendicular to the surface of the filter respectively. Flow visualization was also conducted to observe the flow patterns at different sections. A conventional humidifier was used to generate water droplets and a laser sheet light was used to illuminate the section to observe. Strongly separated flows are found at a large portion of the filtration area, by flow visualization and LDA measurements.

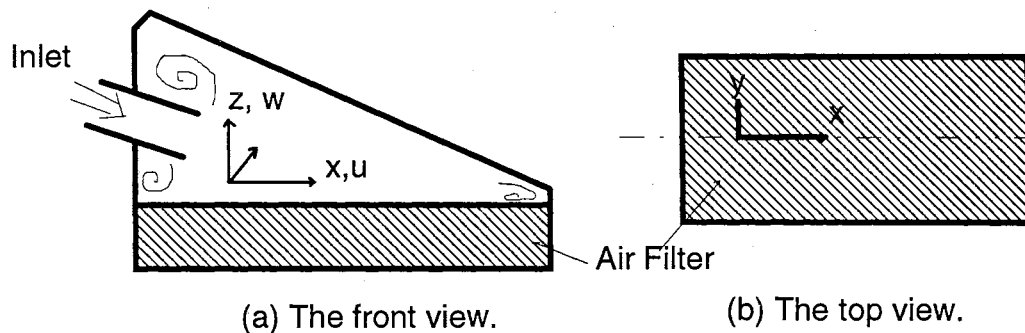


Figure 4.1. Schematic diagram of the coordinates in the model air filter housing. (a) The vertical cross section (x - z plane). (b) The top view of measured area, the x - y plane.

The coordinates and the measured area are depicted in Figure 4.1. There is a section about 62.5 mm long in the x direction behind the inlet tube, upstream of the exit of the inlet pipe. That section is not measured. The flow domain is symmetric with

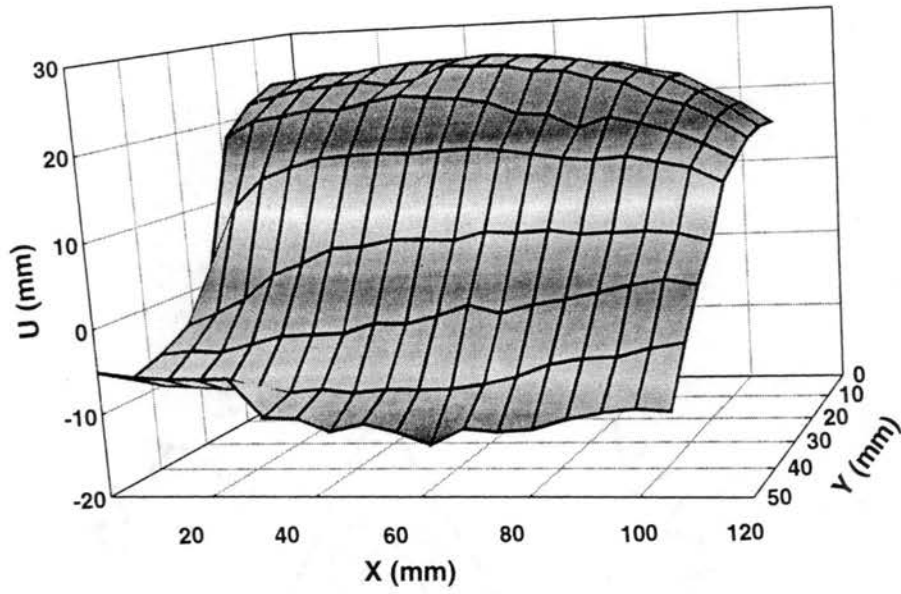
respect to the central x and z plane and preliminary tests showed that the flow field is also symmetric. The measurements reported here were conducted at half of the plane 13 mm above the surface of the air filter starting from the inlet, as shown in Figure 4.1(b). The measurement grid was spaced at increments 6.3mm in the x and y directions. The mean velocity distributions of u and w are shown in Figure 4.2(a) and (b). The vertical velocity w , which is normal to the surface of the air filter, decreases significantly along the stream-wise (axial) direction and decreases even more in the span-wise (y) direction. A large portion of the area is covered by small and negative velocity. Negative velocity implies that the flow is going away from the filter. Since the filtration efficiency of a filter for small particles can decrease rapidly when the filtration velocity, the velocity that is normal to the surface of the filter, is small, the velocity distributions presented are not considered good for filtration. Another observation can be made that the axial velocity is much higher, about 2 times higher, and more uniform than the vertical velocity. However the axial velocity is parallel to the air filter surface, it does not contribute directly to the filtration.

It can be seen from Figure 4.2 that the velocities u and w are large in the center and decrease nearly monotonically as y increases. A separation line, where the mean velocity is zero, is the dividing streamline between positive mean velocity area and the negative mean velocity area. The separation line is determined by finding the location where the velocity is zero. It is interpolated between two points of velocities with opposite signs, assuming that the velocity is linearly distributed between two adjacent measured points. In Figure 4.3, the solid line is where the axial velocity is zero and the dotted line is where the vertical velocity is zero. The x starts from 62.5 mm. The area

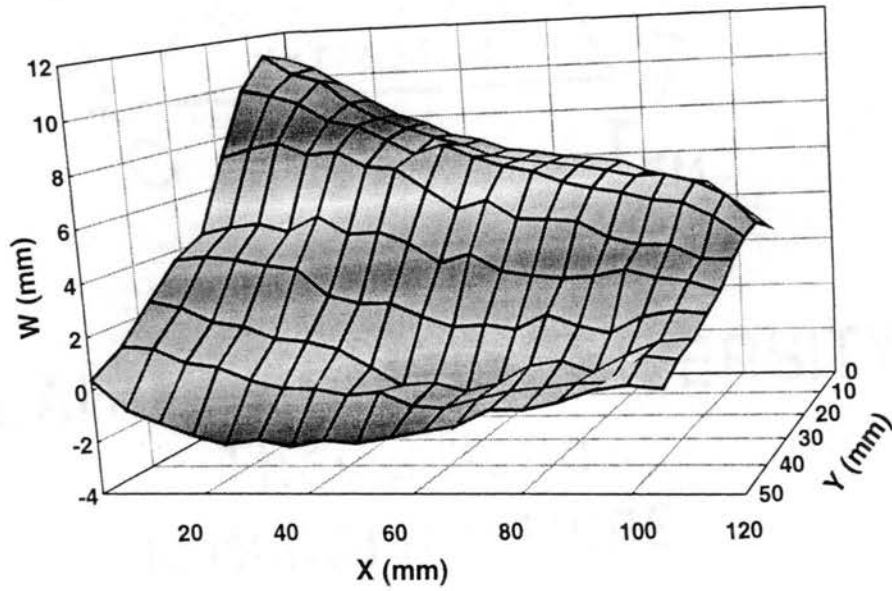
where x is less than 62.5 mm is behind the inlet and visualization showed the flow there is recirculating. To take all the above into consideration, we may estimate that separated flow takes about 40% of the filtration area 12.5 mm above the air filter surface. Since in the separation zone, even in the vicinity of the separation line, fluctuating velocities are quite large, it is still not clear how the filtration is working under these conditions.

However it is understood that when the mean velocity increases at the small velocity range the filtration efficiency can go up and when the velocity exceeds a given value, the filtration efficiency will saturate and then even go down as the result of poor adhesion, for certain particle sizes. Therefore when part of the flow domain is of higher velocity at the expense of the other part having very low velocity, it may not be good for the general filtration. When the flowrate is given, if part of the cross section is in a reversing region where the velocity is negative, the velocity at the other area will be much higher than the mean velocity. While the higher velocity flow is not necessarily improving the filtration there, the reversing flow area is certainly not considered good for filtration. In most cases the uniform velocity distribution is preferred.

When the average velocity is zero while the fluctuation RMS (root mean square) is large as in a separation region, there is still some filtration going on. If the mean velocity is used to assess the filtration efficiency, there will be a problem since very small velocity with some filtration will have very big particle concentration at the area and yield confusing efficiency results. In a separated flow region, different methods should be used to evaluate the efficiency-velocity relation. It is important to identify the filtration regions where flow is separated.



(a)



(b)

Figure 4.2. Velocity distributions 12.5 mm above the filter surface. (a) Axial velocity. (b) Vertical velocity.

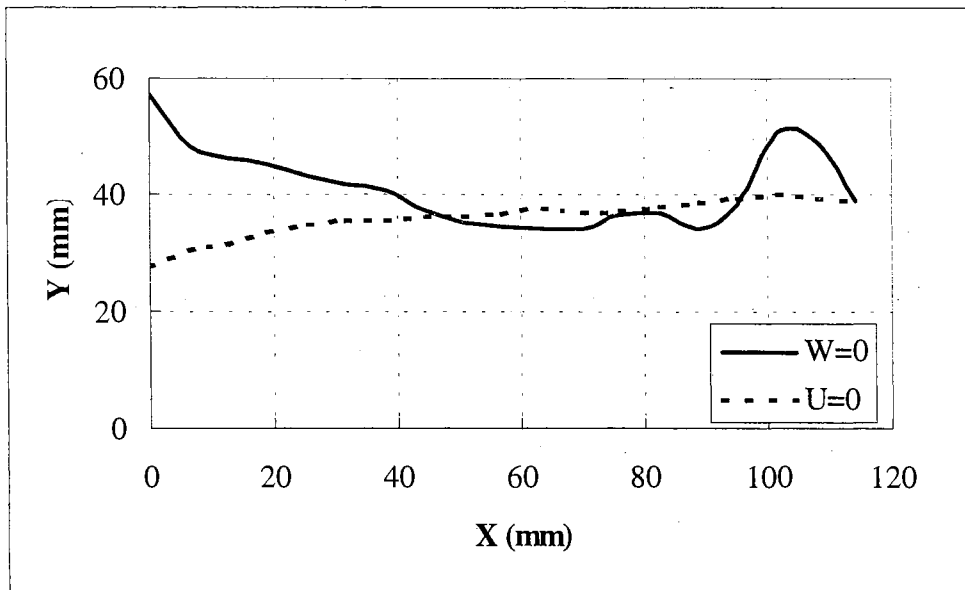


Figure 4.3. Separation lines 12.5 mm above the filter of the air-filter housing model.

From the results above, it should be noted that the flow inside an actual automotive air-filter housing has two dominant features. One is that the flow is very separated mostly because of a sudden expansion at the inlet, which is similar to a backward facing step flow aerodynamically and geometrically. The second is that the flow is not impinging on the filter surface normally, the axial velocity (parallel to the filter surface) is relatively larger. The flow and the geometry of a real air filter housing are too complicated to simulate numerically. It is also difficult to study the flow experimentally since so much is happening at the same time and so little is known about the fundamental properties of the flow. It would cost too much to build experimental setups to model a real housing that can incorporate an air filter at different positions with different geometry surroundings. A step flow could be considered to simulate the two most important features of the actual housing. The step flow has a separated flow region.

Inside the circulation zone the main flow is not parallel to the side walls and therefore is not normal to the filter surface that is mounted normal to the side wall.

The flow with an air filter present is very interesting and different from the pure fluid flows. Little is known about the interaction between the air filter and separated flows. It is very important for air filter and filter housing designs since it is very hard to avoid separated flows in engineering applications. A backward facing step flow is a good prototype to study the interaction of separated flows and air filters. It has the most important features of the flow of a real housing and it is relatively easy for numerical and experimental study. A filter can be placed at different locations downstream of the step, inside or outside of the recirculating region behind the step, so that its effects on the separation flow can be studied under different flow conditions. A two dimensional backward facing step flow was therefore studied both numerically and experimentally and the results will be presented in the later chapters.

CHAPTER V

CFD RESULTS OF TWO-DIMENSIONAL STEP FLOWS WITH AND WITHOUT AIR FILTER

5.1 NUMERICAL RESULTS OF STEP FLOW FOR HOMOGENEOUS PURE FLUIDS

Study of backward facing step flow preceding an air filter can help us understand better the flow inside a real automotive air filter housing. Numerical methods have the advantage that the parameters can be changed easily compared with experiments. The numerical methods described in section 2.4 will be applied to a two dimensional step flow. A FORTRAN program was developed to perform the computations. First of all the code is used to compute the step flow without filter at low Reynolds number.

Comparisons will be made with existing experimental and numerical results to validate the code. For this purpose, the geometry of the flow domain is exactly the same as the experimental set-up of Armaly et al. (1983) and the CFD parameters of Kim and Moin (1985).

For laminar flows the reattachment length depends directly on Reynolds number and the expansion ratio. This relation can be used to check the numerical methodology. At low Reynolds numbers, the reattachment of the step flow is largely controlled by the momentum transfer through viscous diffusion, especially at the near sidewall region or the strong shear layer near the step edge. Excessive numerical smoothing, such as extra numerical diffusion, may incorrectly enhance the viscous effects and will not predict the

right reattachment length (Kim and Moin, 1985). In this section the results are reported for low Reynolds number laminar flow. The geometry and boundary conditions are shown in Figure 1.2. The inlet velocity profile was given as parabolic, as the fully developed channel flow profile from Armaly et al. (1983) in the laminar flow regime. Outflow boundary was located 30 step heights away from the step and the fully developed condition was prescribed, with the velocity gradients in the axial direction zero in the cross section. These inlet and outlet conditions are the same as used by Kim and Moin (1985). In the present computation, convergence is considered to be reached when the velocity u and pressure P are constant within .01% for a time period of one non-dimensional time unit, namely $\frac{3h}{2U_{\max}}$. The computation procedure starts from initial conditions of zero velocity and uniform pressure fields to compute the lowest Reynolds number flow reported here. The inlet velocity profile is normalized parabolic, with the maximum velocity being one. This initial condition is an aerodynamically true condition, the case that a constant flowrate flow is suddenly introduced into a still flow domain. Therefore the flow oscillates violently at the beginning and then converges to a steady state flow. After the first Reynolds number flow converges, the known flow field is used as the initial condition for the next higher Reynolds number flow; and so forth. The inlet profiles are always the same since it is normalized; it is just the Reynolds number that needs to be changed every time. Every time that the Reynolds number is increased there are significant fluctuations when the flow acts like a higher flow rate is introduced to an existing flow of lower flow rate. The velocity and pressure fluctuates more than 100% at the very beginning. It takes many time steps to get a stable flow. The computing accuracy is also examined for all cases by applying the continuity condition. For each and every

mesh cell, the continuity equation is applied. That is if $\Delta D = \frac{\partial u}{\partial x} + \frac{\partial v}{\partial y} \leq O(\Delta^2 x + \Delta^2 y)$.

For all the cases presented here, the accuracy of all the results is

$$\Delta D \leq .05 \quad \text{when } \Delta x = .3 \text{ and } \Delta y = .02 .$$

All the variables are non-dimensional, as the non-dimensional equation in Chapter 2. The flux at each and every cross section for the entire flow field is calculated by adding up the axial velocities in all the vertical grid locations at the section. The difference between the maximum flux and the minimum flux is less than .1%, which indicates the computation is also accurate for the overall mean flow field. There are two reasons for applying continuity conditions to check the numerical accuracy. First one is that it is easy to implement and it is generally applicable. The second is that in the present numerical method, the continuity equation is not explicitly solved. Continuity is implicitly applied in the process of the numerical procedure. It can demonstrate whether the entire computation procedure is working properly or not by checking the continuity at each and every grid cell.

100 by 101 grid points were used in all the results reported for laminar flows with and without filter, with $\Delta x = .3$ and $\Delta y = .02$. The 101 grid points in the vertical direction were chosen to match exactly the parameters of Armaly's experimental setup, in which the channel is 10.1 mm wide and the step is 4.9 mm height. 101 ensures the step starts at a grid point. The mesh size and the outlet location were chosen based on the CFD model of Kim and Moin (1985). The same results were obtained with finer and coarser mesh sizes and farther downstream outlet locations at $Re=600$, which can verify that the computed results are independent of difference scheme at present conditions. The

Reynolds number of 600 was chosen because it is the highest Reynolds number that currently can yield good results for the two-dimensional laminar flow regime. The higher Reynolds number flow needs better resolution and bigger computing domain since the stronger shear and the longer reattachment length at the present range of Reynolds numbers. For the same computed domain of $30h$ by $2h$, 41×41 , 81×81 , 101×101 , 126×126 and 202×202 grid points were used to compute the flow field at $Re = 600$. As shown in Figure 5.1, the two cases of 101×101 , 126×126 and 202×202 yielded about the same results while the other two cases are not good enough.

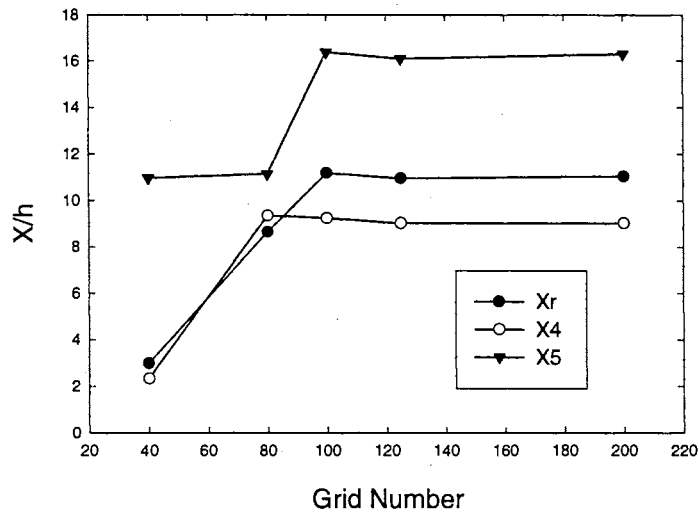
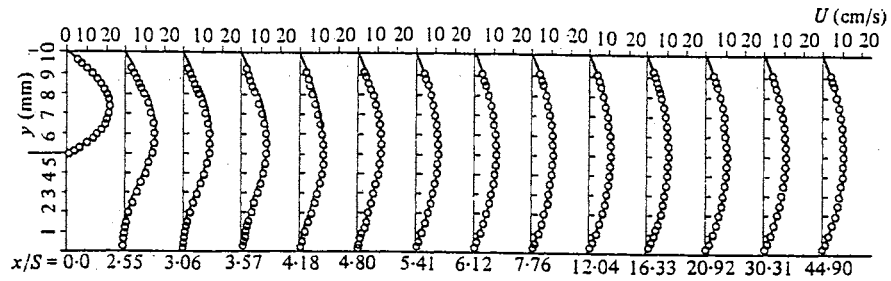


Figure 5.1. The effects of the grid size on the computed flow fields.

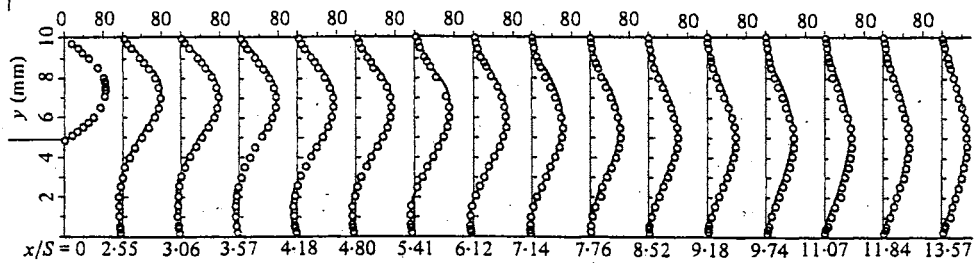
Then with the same mesh size as 101×101 , the outlet was located at $36h$ by employing 121 grids and at $45h$ by employing 151 grids in the x -direction. The locations of the two dominant vortices were found at $X1 = 11.13S$, $X4 = 9.16S$, and $X5 = 16.37S$ for $36h$ and $X1 = 11.16S$, $X4 = 9.18S$, and $X5 = 16.37S$ for $45h$. With the outlet at $45h$, they were $11.16S$, $9.18S$ and $16.37S$ and with the outlet at $30h$, they were 11.19 , 9.24 and

16.37 respectively. We can see clearly that $30h$ is adequate for the current purposes. The symbols of the vortex locations were described in Figure 1.2 and will be explained more in the later text.

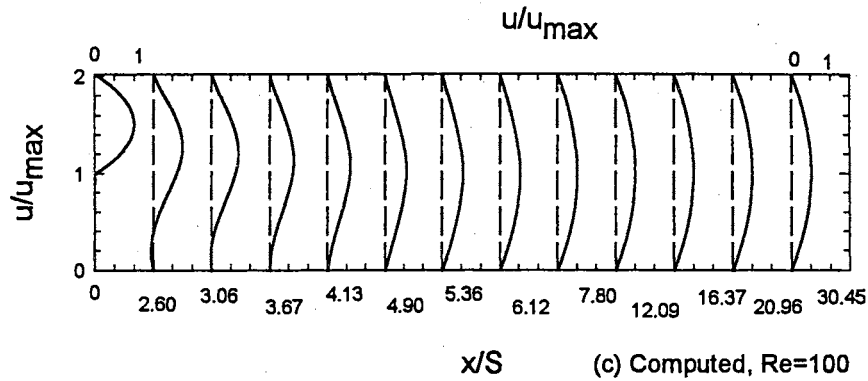
To further examine the computing algorithm, the velocity profiles of the flow fields at Reynolds numbers of 100 and 400 are shown in Figure 5.2. Figure 5.2 (a) presents the velocity profiles measured by Armaly et al. (1983) at Reynolds numbers of 100 and 400, (b) presents the current computed profiles for the same Reynolds numbers. The locations of the computed profiles are not exactly the same as of the measured ones, however they are very close. If we overlap the two plots of the same Reynolds number, we can see that the computed and measured profiles at both Reynolds numbers match reasonably well. There are some differences, however the agreement is satisfactory for the present purpose.



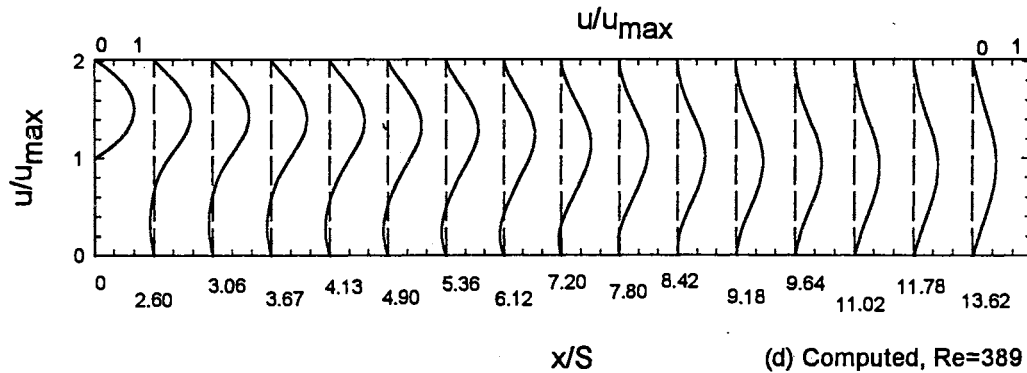
(a) Measured, Armaly et al., Re=100



(b) Measured, Armaly et al., Re=389



(c) Computed, Re=100



(d) Computed, Re=389

Figure 5.2. Comparison of computed flow fields with the flow fields measured by Armaly et al. (1983) at Reynolds numbers of 100 and 389.

Figure 5.3 depicts the dependence of the reattachment length on Reynolds number at 800 and less. X_1 is the reattachment length, measured from the step to the reattachment location. It is found by locating the zero axial velocity at the first grid point away from the step side wall. Up to Reynolds number 600, the results are in very good agreement with the experimental results of Armaly et al. However the present results are a bit different from the computations of Kim and Moin. Their results are close to the experimental results at lower Reynolds number. The present results yield a better agreement at Reynolds numbers from 400 to 600. The two computational curves are almost parallel while the present reattachment length is about .5 step height farther than Kim and Moin's. It is not clear what caused the discrepancy between the present results and theirs. As pointed out by Armaly et al., the experimental step flow exhibits significant three-dimensionality around Reynolds numbers between 600 to 6600. Most likely the three-dimensionality caused the deviation of the numerical results from the experiments at Reynolds number above 600, since the present CFD model is two-dimensional.

Armaly et al. (1983) also reported the existence of a secondary separation region on the non-step wall in the range of $Re=400$ to 6600, mostly when the flow is not purely two-dimensional. As shown in Figure 1.2, the location of the secondary vortex is measured by X_4 and X_5 , which are respectively the locations of the upstream edge and the downstream edge of the non-step side vortex. In the computations of Armaly et al. and Kim and Moin (1985) there is no quantitative comparison of the locations of the non-step side vortex with experiments. It was reported by Kim and Moin that the vortex exists at $Re=1000$. Figure 5.2 shows the computed locations of the vortex compared with

Armaly's experimental results for Reynolds number 450 to 800. The present CFD results are in fairly good agreement with the experiment. This indicates that the present CFD model and codes are working properly for quantitative details.

The secondary vortex is very delicate, with very small negative velocities. Its reversing area is very thin in the vertical direction. The contours of the computed flow field, shown in Fig 5.5, clearly demonstrate the existence of the secondary vortex on the non-step wall at Reynolds numbers 450 and 600. At low Reynolds number, such as $Re=300$, the curvature of the contour at the top wall at the vicinity of $x=7h$ is not big enough to cause recirculation at the area. At $Re=450$, the flow is curved further and the circulation starts to form at the upper side, though it is a very small area. From Figure 5.4 we can see that the secondary vortex forms at Reynolds number about 400. This is very close to the experimental results of Armaly et al. (1983) in which the vortex begins to appear at $Re=400$. As the Reynolds number increases, the vortex at the non-step side stretches longer in the streamwise direction and the center of the vortex moves further downstream due to the increase of the inlet velocity. At low Reynolds number the contour lines are very straight far downstream, which indicates the flow is smooth there. However at 600, visible oscillation appears. At $Re=800$, the computed flow is no longer stable. It is not clear what caused the instability. This Reynolds number is in the transitional flow regime, so the flow is no longer stable. The instability also may be the result of numerical instability. Additionally at this Reynolds number the flow is no longer two dimensional, hence the two dimensional model used is no longer appropriate.

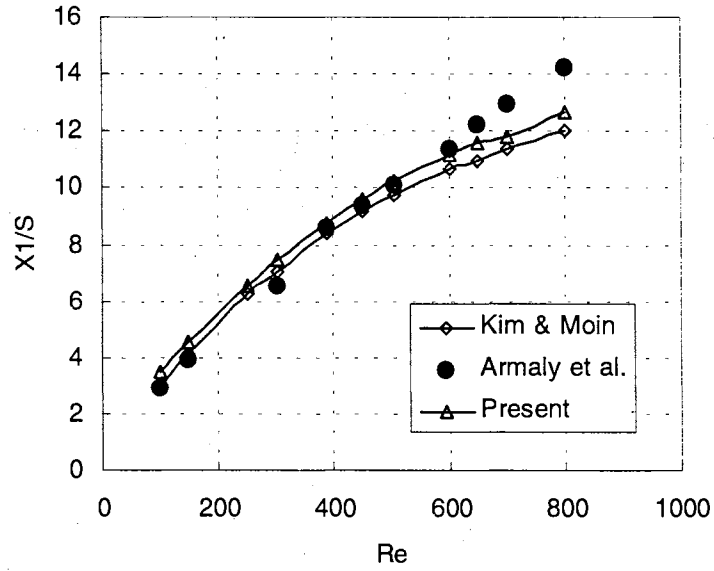


Figure 5.3. Reattachment length vs. Reynolds numbers

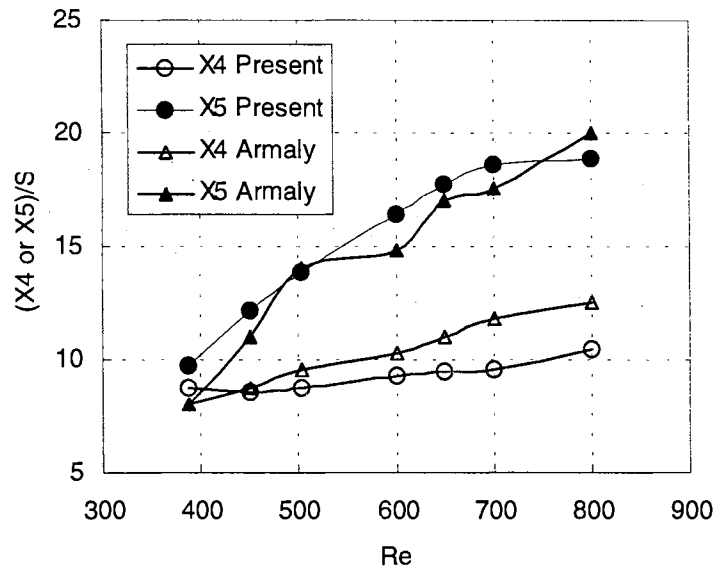


Figure 5.4. Locations of the secondary vortex at the non-step side.

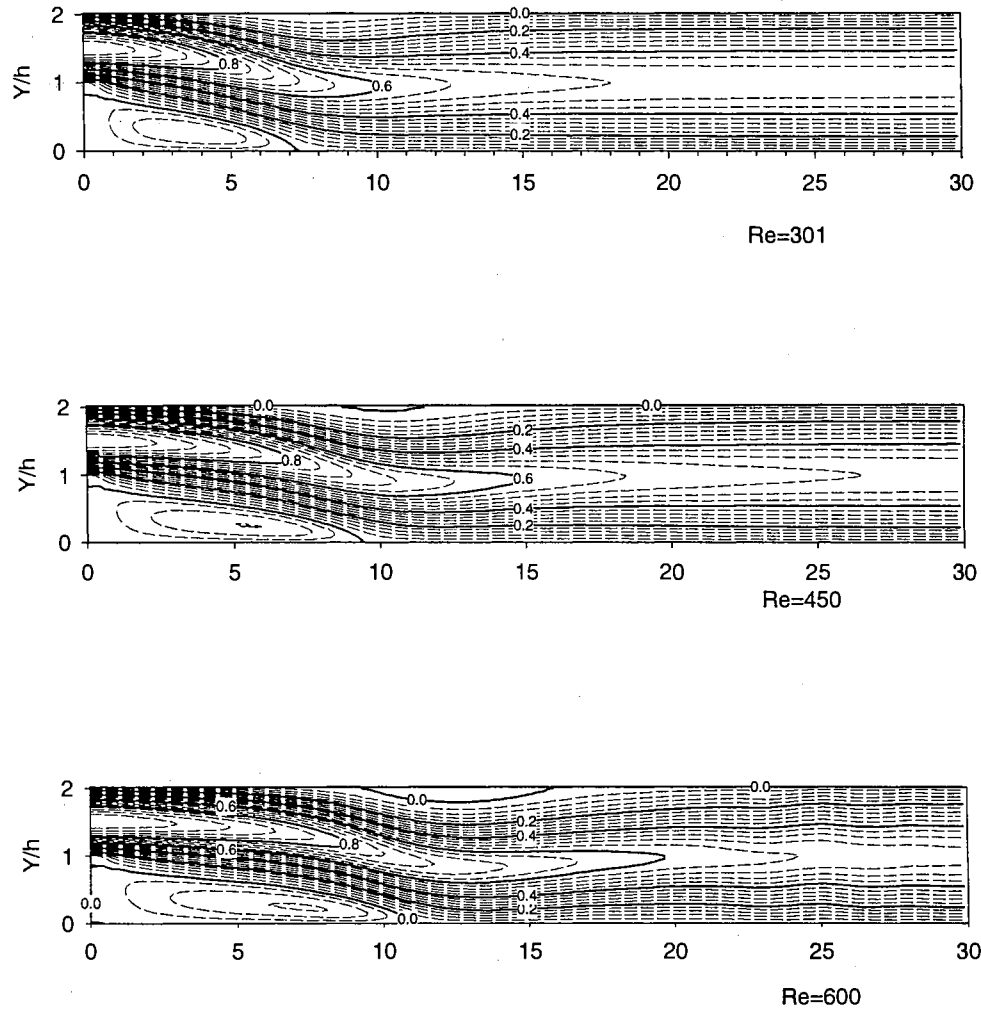


Figure 5.5. Contours of velocity u at different Reynolds numbers.

At Reynolds numbers 600 and less, the velocity u and pressure converged to the required criteria. However when Reynolds numbers are higher than 600, the computation can not converge to the specified accuracy. The velocity and pressure fluctuate in a range around 1%. The velocities and pressure are changing significantly. It is not very clear what causes the instability. Figure 5.5 also depicts the shape of the primary vortex downstream of the step. It is noted that the shapes are similar for different Reynolds number. At the inlet where $x = 0$, the separation line starts at the same vertical location. The separation line is defined here as the non-wall locations with zero axial velocities. As Reynolds number increases, the vortex, with a domain bounded by the zero velocity contour lines, stretches downstream, similarly as the non-step side vortex. That results in less effective passage area for the flow and higher velocity gradient in the core region corresponding to the location of the vortex.

The vector field of velocity is shown in Figure 5.6, with the positive axial velocity u directed to the right and the vertical velocity v directed upward. The lines start from zero, their length represents the absolute value of the velocity vector and from zero to the line end indicates the direction of the flow. At the entrance the velocity profile is parabolic for horizontal velocity u and zero vertical velocity. Thus the lines there are horizontally parallel. Then due to the existence of the step, the main flow turns to the bottom side and negative velocities are found behind in the step. Far downstream the main flow recovers from the recirculation and flow becomes horizontally parallel again as at the inlet, only here the profiles are flatter due to the channel being wider. In the process, the main flow turns from going downward back to going straight to the right, a low velocity area forms at the top non-step side. The low velocity area at about $x=10$ is a

recirculation flow zone, which is more clearly demonstrated in Figure 5.3 (Re=450).

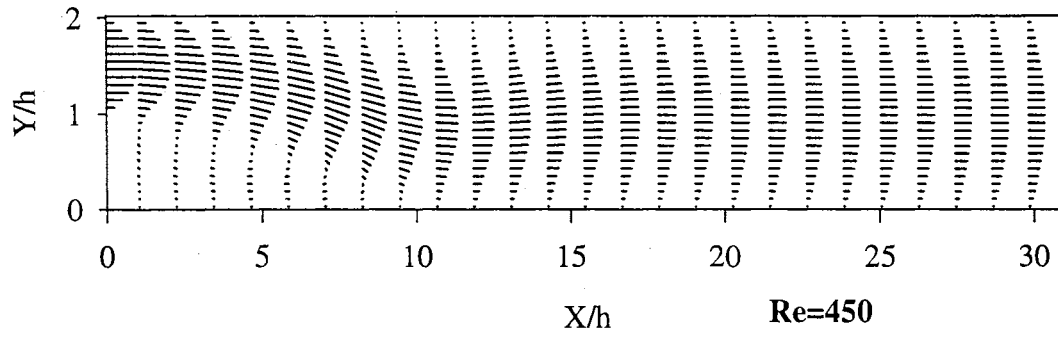


Figure 5.6. Flow field for u-v vector at Re=450.

5.2 LAMINAR FLOW WITH POROUS MEDIUM PRESENT

In the previous section it is verified that the present CFD mode and the codes for two-dimensional step flow provide quantitatively reliable results for a certain range of Reynolds number. At this section the CFD model is used to study the effects of the filter on these step flows. All the geometric and CFD parameters are kept the same as in the previous pure fluid computations except a section of air-filter is placed in the flow domain. The filter is placed at three different locations with respect to the step and the circulation zone; far downstream, close to the reattachment location and deep inside the circulation zone. Pressure and velocity distributions will be presented to demonstrate the effects of the air-filter's presence on the whole flow field and the circulation properties.

5.2.1 Parameters of the Darcy's Law

In the present CFD model filters are considered as homogeneous porous media since most filtration theories and models are based on statistically homogeneous filtering media. A flat sheet of filtering media is very close to homogeneity. However most filters used in industrial applications are pleated from flat sheets. Compared with a flat sheet, a pleated filter is more compact in space using and allows for more effective filtration area for a given cross section. It is stated in Liu (1995) that more filtering area allows more particles to be captured in a fixed volume of space and so reduces the pressure drop across the filter due to the decrease of the effective filtration velocity. Designs of a pleated filter seek minimum pressure drop at given geometry and filter medium, which implies in general a pleated filter causes less pressure drop and captures more particles than a flat sheet of filter for the same filtration area and velocity.

In the present experiment (results will be presented later in Chapter VI), a pleated filter (a production model: Purolator Products, A13192) was used and rearranged for the current geometry. For the micro-scale flow a pleated filter is very different from a homogeneous one. However for the macro-scale the effect of the filter is to cause more pressure drop and the pressure drop is largely proportional to the bulk upwind velocity. It should be noted that in the pure fluid, viscous resistance is largely proportional to the velocity gradients. For a CFD model it is important to choose the right parameters for the porous medium to produce the right pressure drop in the flow. A pleated filter produces less pressure drop than a single sheet of the media of which it is made with the same cross section. This is because the effective upwind surface for the pleated filter is much larger than for the flat sheet, which has an effective velocity equal to the velocity in the channel. For instance the area of the filter sheet, from which the pleated filter is fabricated, is about 15 times as much as the cross section area. Then the effective velocity for the pleated filter is about one fifteenth of the mean velocity of the channel in which the filter is placed. In the extended Darcy's law there is a second order term of velocity, the pressure drop could decrease more than 15 times when velocity is large. Due to the complexity of the pleated filter, most theoretical and numerical researches consider the pleated filters as homogeneous media, as in the present CFD model. Tebbutt(1995) computed the flow field inside a pleated filter, however the results are not yet ready for applications.

Tebbutt (1995) found the two constants in the extended Darcy's equation by setting up a pipe flow and measuring the average velocity and the pressure drop over a

single sheet of the filter media, using the media from Purolator A13192 filter. In

Tebbutt's experiment the extended Darcy's equation was:

$$\Delta P = \frac{\mu t}{K} U + \frac{b \rho t}{2} U^2$$

where

t = media thickness

U = average velocity on the cross section

P = pressure

K = media permeability

b = inertial factor.

It should be noted that the inertial factor here is different from the factor B in equation in section 2.4.2. However the basic relation between pressure and the velocity is the same, so we have $b = B/K$. Tebbutt measured the pressure drop over the velocity range of 0 to 15 m/s and used the least squares method to derive the two constants. The maximum pressure drop at velocity of 15 m/s is about 1 meter of water, which is about 10,000 Pa. These two constants are independent of the thickness and Tebbutt (1995) verified that by applying the procedure to two layers of filter sheets, which yielded the same results. The values from Tebbutt (1995) are

$$K = 7.8e - 11 m^2 \text{ and } b = 6.8e + 4 m^{-1}.$$

The thickness of the filter sheet used in Tebbutt's experiment was one millimeter, which is very small for the present CFD model to incorporate into the grids of the flow domain. Present CFD configurations of the flow domain are based on the experimental setup of Armaly (1983), in which the length scale to normalize the equations is 5.05 mm, the half height of the channel h. In the present computation the grid size in the x-

direction, which is the direction to measure the thickness of the filter, is $.3h$. Since the flow would undergo significant changes at the interfaces between the filter and the pure fluid, multiple grids are needed to simulate the fluid flow inside the filter. For laminar flows the porous medium occupies 10 grids in the x direction, which is $3h$ and equal to about 15 mm if the experimental parameters of Armaly et al. are used. If the same filter media in Tebbutt's experiment is used, it will need 15 layers of the filter sheets and the pressure drop will be practically too big. In a real engineering application, it is more likely that a pleated filter is used. Therefore we can assume that a pleated filter is used, which is made of the same media used in Tebbutt's experiments and is 15 times as thick as a single sheet. This would be very close to geometrical parameters of the real Purolator A13192 filter. A pleated filter will cause less pressure drop, however it is very difficult to estimate the pressure drop of a pleated filter based on the properties of the single sheet. It is the pressure drop in the CFD that is the most important variable that should be matched with the experimental results. Therefore modifications were made to the two constants to keep the pressure drop the same for a filter medium that is 15 times as thick as in Tebbutt's experiment. That is

$$K_e = K \times 15 \text{ and } b_e = b / 15$$

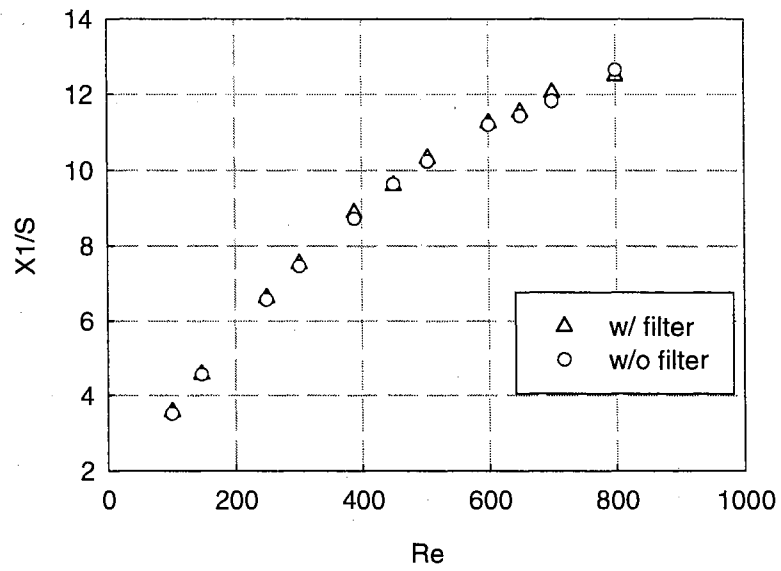
In the computation the two constants were normalized by the length scale as in the experiment of Armaly et al. and converted to be compatible with the equations in section 2.4.2.

5.2.2 Porous Medium Present Far Downstream:

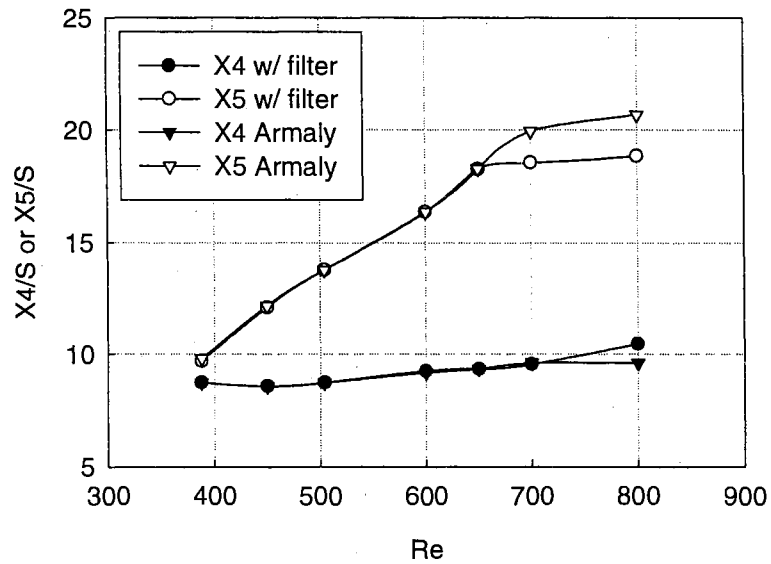
For this case, the filter is placed at $20.55h$ downstream of the step, which is the location of the left side (upstream) of the filter, with h the half height of the channel. The

filter is $3h$ thick. In the Reynolds number range that we are interested in here, the non-step side vortex reaches about $19h$ at the most and the reattachment length is less than $14h$. Therefore the $20.55h$ is a proper position to be considered far downstream and the filter does not directly disturb the vortices in the flows. The right side, downstream, of the filter is at $23.55h$, which leaves adequate room for the flow downstream to recover to the outlet of $30h$. From the computed flow fields that will be shown later, it can be seen that the flow is smooth and parallel at the outlet, which indicates that the fully developed outlet condition applies. Additionally due to the resistance of the filters, the downstream conditions have less impact on the flow upstream of the filter. The thickness of the filter is $3h$, which is about 15mm if the parameters of Armaly et al. (1983) are used. The reasons to choose $3h$ are that the actual thickness would be close to a real air-filter's thickness for a regular experimental setup and also there is enough room for the flow to evolve inside the porous medium.

First of all we will see how the filter affects the size and location of the vortices upstream of the filter. The definitions are the same as in previous sections. $X1$ is the reattachment length; $X4$ and $X5$ are the upstream and downstream edges of the secondary vortex respectively. The reattachment length and the location of the non-step side vortex are shown in Figure 5.7. The presence of the filter has little effect on the reattachment length for the whole Reynolds number range and has no effect on the non-step side vortex up to Reynolds number 600.



(a)



(b)

Figure 5.7. Comparison of flows with and without the filter, the upstream edge of the filter is at $20.55h$. (a) Reattachment length. (b) Locations of the secondary vortex.

The pressure upstream of the filter certainly increases due to the resistance of the filter, which changes the velocity field in its vicinity. However Figure 5.7 indicates that the velocity field away from the filter is not affected. This is like a case in which the pressure field is increased uniformly far upstream of the filter. From the basic equations we know that if the pressure gradients stay the same, the velocity field in that area will not be altered by the uniform variation of the pressure field. At $Re = 700$ and 800 , the downstream edges of the non-step side vortices are stretched further, very significant changes compared with the flow without the filter, as shown in Figure 5.7(b). Any pressure field changes may affect the flow in its upstream vicinity. Nevertheless the computation does not converge very well at these two Reynolds numbers; further research is needed.

From Figure 5.7, we may conclude that when the filter is placed far downstream, the filter does not affect the flow recirculation upstream. This can be confirmed by looking at the flow field of $Re=600$, shown in Figure 5.8. The velocity field is significantly altered at the vicinity of the filter, however the velocity field is still the same as the non-filter flow field (shown in Figure 5.5) behind the step up to $5h$ upstream of the filter.

It is also noted that the flow is considerably straightened by the presence of the filter at Reynolds number 600, not only downstream of the filter, but also at its vicinity upstream. The same effect is also found in Reynolds numbers of 800. The viscous effects are proportional to first order of velocity and the inertial force is proportional to the square of the velocity, which means inertial effect is less important at low Reynolds numbers. Inside the filter, there is an extra viscous term that is proportional to the

velocity, not like the conventional viscous terms, which are proportional to the derivatives of velocity. This indicates that the filter can suppress the velocity fluctuations due to the resistance that is proportional to the velocity. Since there is no outside driving pressure gradient in the vertical direction, the vertical velocity can be reduced considerably, which implies smooth and stable flow because the contours tend to be straight.

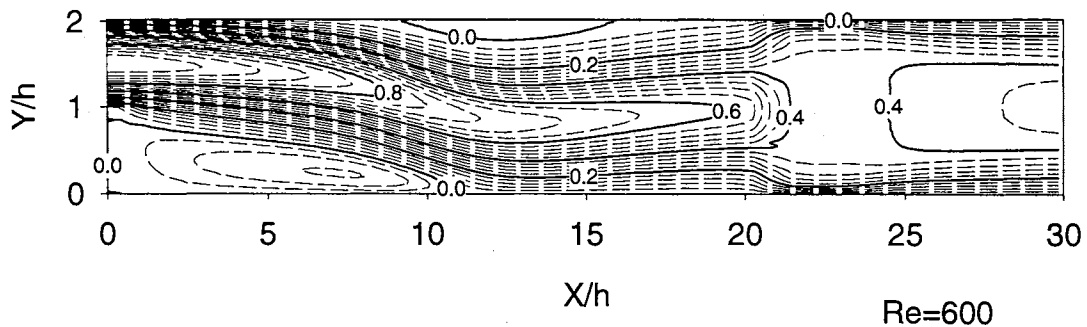


Figure 5.8. Contour of velocity u with the filter's leading edge at $20.55h$, $Re=600$.

By the u - v vector field with the filter at $20.55h$, shown in Figure 5.9, it is more clearly demonstrated how the filter affects the velocity profiles around the filter. If we compare Figure 5.9 with Figure 5.5, the u -contour of the flow without filter at the same Reynolds number 450, it can be seen the velocity distributions are altered significantly by the introduction of the filter. Upstream of the filter and downstream of the recirculation zone, the flow is horizontally parallel at first, the velocity profiles tend to be parabolic. The velocity in the center is much higher than the velocity close to the wall and the velocity changes gradually from the zero at the wall to its maximum at the center. When

it is approaching the filter, the vertical velocity v becomes considerably larger. At the upper half of the channel the velocity v is positive (upward) while at the lower half v is negative (downward), which indicates the fluid flows to the two sides symmetrically. The flow is redistributed toward uniform flow because of the resistance of the filter. Once inside the filter, velocity is horizontally parallel again, which indicates no visible vertical movements. The flow is almost uniform in most of the channel. At the wall region inside the filter, the velocity gradient is very large due to the enhanced viscous effect of the filter. Downstream of the filter the velocity profiles have a defect in the center at first, and then the flow gradually evolves to fully developed channel flow. This will be discussed later.

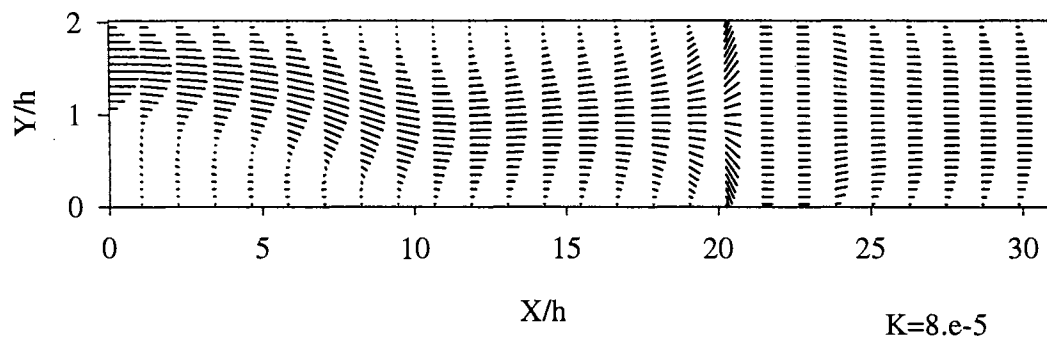


Figure 5.9. The u - v vector field of flow with the filter's leading edge at $20.55h$, $Re=450$.

The value of the permeability, 8×10^{-5} , used in the present computation is the value derived from the experimental data of Tebbutt (1995). To look at how the permeability value influences the flow field, three different values were chosen for the

filter at $x=20.55h$ and the flow fields are shown in Figure 5.10. These are the u velocity contour fields at the same Reynolds number with the permeability varied from 8×10^{-5} to 8×10^{-3} . The smaller the permeability; the higher the resistance of the filter. First of all it can be seen from the u -contours that the resistance of the filter has little effect on the flow far upstream. This agrees with the observation of the reattachment length and the locations of the non-step side vortex when the filter is far downstream. However the flow inside the filter and downstream are different due to the existence of the filter and the values of the permeability. Immediately upstream of the filter the u -contour becomes flatter as the permeability decreases, which indicates the flow decelerates more in the center. Downstream of the filter the velocity profiles appear to have defects in the center, consistent with Figure 5.9. It certainly takes longer for the flow with higher resistance to recover at the outlet to the parabolic profiles. The choice of the permeability has some influence on the flow field in the immediate vicinity of the filter; nonetheless it does not have much effect on the flow patterns and the flow field far upstream of the filter.

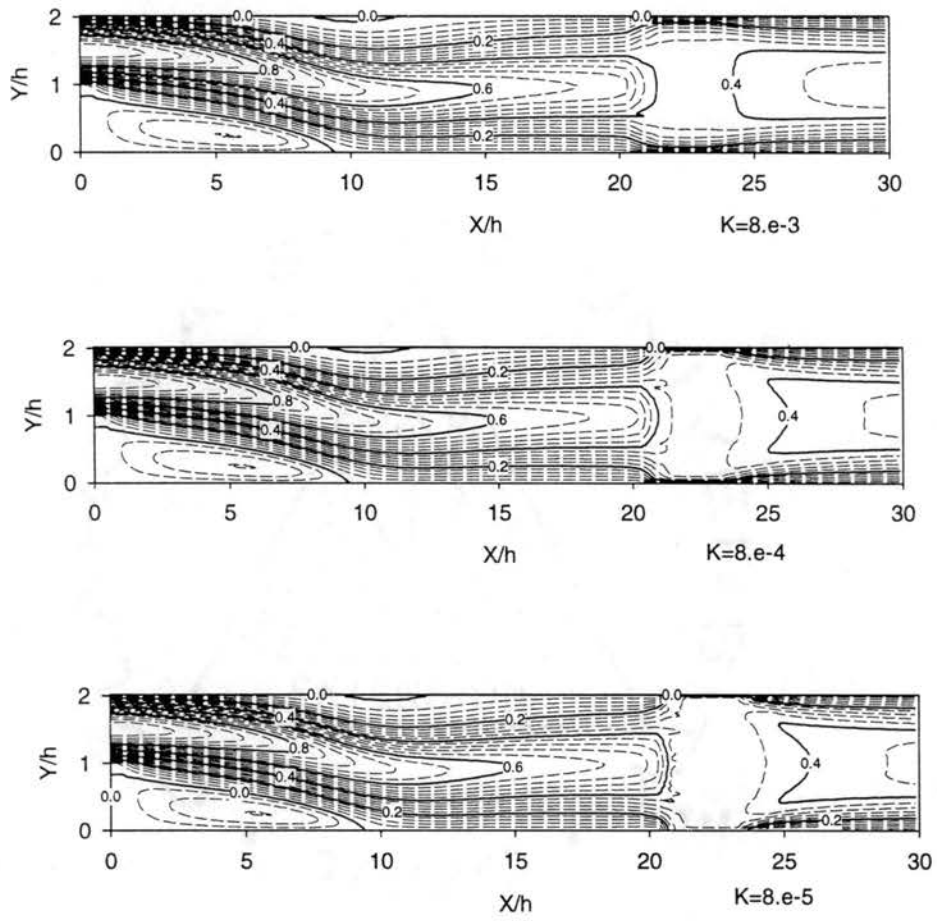
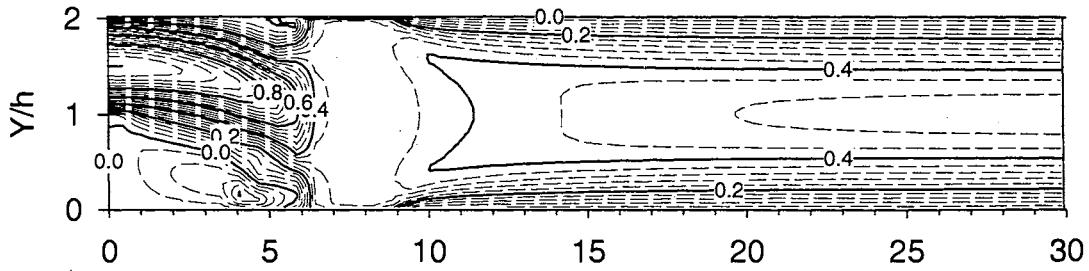


Figure 5.10. Contour of velocity u at different permeability value K 's.
Filter's leading edge at $20.55h$, $Re=450$.

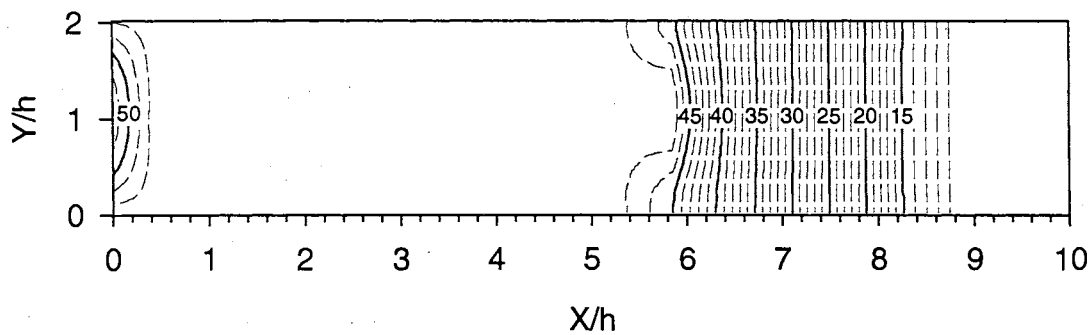
5.2.3 Filter Deep inside the Non-Filter Flow Separation Zone

When the filter is far downstream of the step, the results presented in the previous section show that it does not have very much impact on the flow upstream. However when the filter is placed inside the circulation zone, the flow field is altered significantly. As shown in Figure 5.11, (a) is the contour field of the velocity u and (b) is the contour field of the pressure. The Reynolds number is 450. The filter is placed between 5.85 to 8.85 half channel heights from the step. Downstream of the filter, velocity distributions become broader and the flow becomes parallel, compared with the flow field depicted in Figure 5.9, where the filter is further downstream and the Reynolds number is the same. This agrees with the results in the previous section that show that the filter makes the flow smoother and the velocity profiles broader. Since the filter is close to the step and there is no reversing flow downstream of the filter, the flow clearly has more room to recover, which can explain why the flow is smoother at the outlet. It is blank inside the filter of Figure 5.11 (from 7 to 9h), the same as in Figure 5.10, which indicates that the velocity profiles are uniform in most part of the channel inside the filter.

At $Re=450$, the reattachment length is about $9.5h$ and the secondary vortex is located around $10h$ when the filter is not present. When the filter is placed at $5.85h$ the two circulation flows at both sides of the channel are pushed upstream of the filter. From the previous section we already know that the filter forces the flow to redistribute with the velocity profiles becoming broader in the vertical direction upstream of the filter. That implies the large velocity in the center decreases and the small velocity close to the wall increases. When the flow accelerates it is less likely to separate from the wall, so the circulation zone stops upstream of the filter where the flow is accelerating.



(a) Contour of velocity u of the flow with filter at 5.85h to 8.85h, $Re=450$



(b) Pressure contour over the filter, filter at 5.85-8.85h, $Re=450$.

Figure 5.11. Flow field with filter close to the step at 5.85h, $Re=450$.

When the filter is placed far downstream, it does not have much impact on the flow upstream. The difference is that the velocity profiles far downstream are flatter than the profiles behind the step, where the primary vortex exists. With the existence of the vortex behind the step, nearly one quarter of the channel width is occupied by reversing flow; velocity varies rapidly across the channel. The non-filter flow is strongly separated at the location of the filter. Therefore the flow redistribution when the filter is placed close to the step causes much more change in the velocity distributions than the case with

the filter placed far downstream.

It should be noted that when the filter is at $5.85h$, the secondary vortex at the non-step side does not disappear, although it is moved upstream and its shape has changed considerably. It may be more adequate to say the conventional secondary vortex is eliminated by the filter and a new vortex is produced at the non-step side upstream of the filter. It is understood that the conventional vortex disappears due to the flow accelerations. The formation of the new vortex may be caused by the fact that the filter forces the contour line curve farther away from the wall upstream of the filter at the upper boundary. Comparing Figures 5.8 and 5.9, it can be seen clearly that the contour lines upstream of the filter incline to the lower boundary, much more in Figure 5.11 where the new secondary vortex is formed than the same location in Figure 5.10. Because the reversing area at the step side around $x=5h$ is reduced dramatically, the direction of the main flow is much more inclined to the lower boundary.

The pressure contour lines in Figure 5.11 demonstrate clearly that the pressure is higher in the center than in the wall region upstream of the filter, which implies vertical fluid flow. The pressure gradient in the x direction is large and negative at the wall region upstream of the filter, which indicates flow accelerations at the areas.

It is more clear to look at the pressure distributions upstream and inside the filter, as in Figure 5.12, where $Y/h = 0$ is the upper non-step side wall. At $x=5.55h$, which is one grid upstream of the filter, the pressure is almost uniform. That indicates that the pressure gradient across the channel, in the vertical direction, is very small. However at the interface between the pure flow and the filter, $x=5.85h$, the pressure is much higher in the center and smaller near the wall. There is a big pressure gradient in the vertical

direction to produce velocity in that direction. The pressure distributions inside the filter are nearly symmetric with respect to the center line, with the gradient at the step side a bit steeper. This indicates that the redistribution of the flow is stronger for the step side than the non-step side.

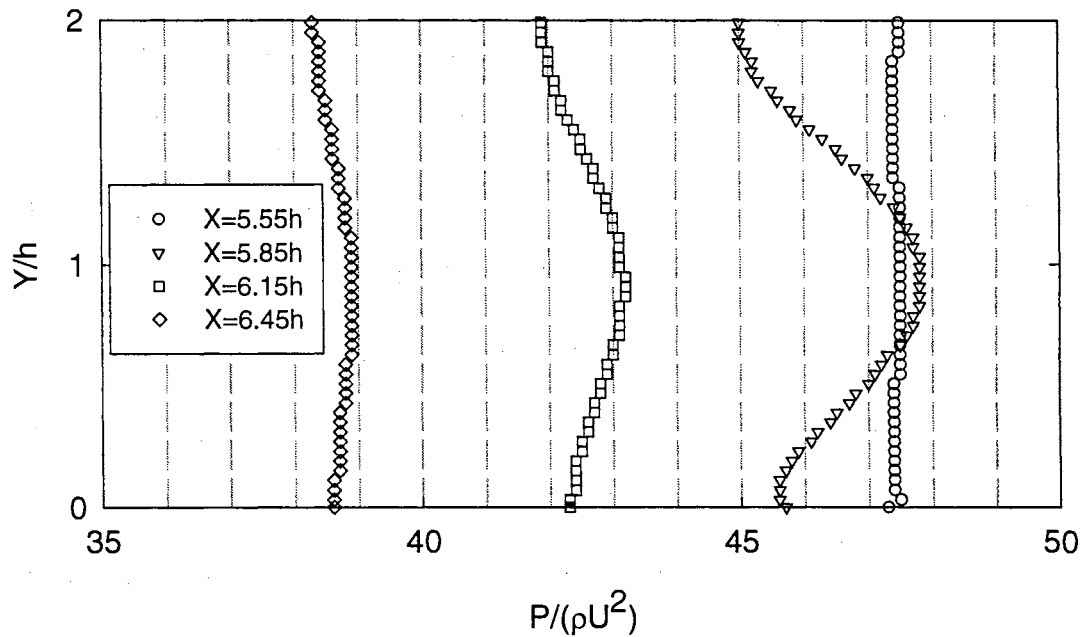


Figure 5.12. Pressure distribution at the upstream side of the filter. $Re=450$, filter's leading edge at $5.85h$

The pressure gradient in the stream-wise direction can be estimated by the difference between the pressure at two adjacent grids. We can see that the gradient in the center is positive and close to the wall the pressure gradient is large and negative by simply compare the two profiles at $x=5.55h$ and $5.85h$, which are the pressure profiles upstream and at the filter surface respectively. The pressure distributions explain two phenomena clearly. One explanation is that fluids are flowing from the center to the sides, most significantly at the upstream surface of the filter since the pressure difference

between the center and the wall is the largest at the location. Since the velocity in the center is higher, this makes the velocity profiles flatter. Another explanation is that the pressure gradient near the wall is large and negative just upstream of the filter. This is favorable to reattachment and prevents the flow from separating at the wall.

Inside the filter, the pressure distribution curves are similar; however they get flatter and flatter downstream. Eventually the pressure is uniformly distributed at the downstream part of the filter as shown in Figure 5.11(b). In the process the flow becomes parallel and nearly uniform across most of the channel. It should be noted that inside the filter the governing equations are different from those of the pure fluids. Inside the filter the resistance, mainly caused by viscous effects following Darcy's law, is largely proportional to velocity, with the viscous terms for the pure fluids much smaller. Therefore the pressure distribution tends to be similar to the velocity distribution and follows the changes in the velocity. In the pure fluids the resistance is mainly the viscous terms at low Reynolds number, which is proportional to the velocity gradients. Therefore the velocity distribution in the vertical direction tends to be parabolic since the flow maintains a constant shear in the vertical direction, that is close to uniform pressure distribution in the direction, as shown by $x=5.55h$ of Figure 10. At the upstream side of the porous media, the velocity profiles are close to parabolic, however the relation between the velocity and the pressure changes instantly at the interface. To maintain a parabolic velocity profile requires a similar parabolic pressure profile in the vertical direction as the change of the governing equations, as shown by the pressure distribution at the interface $x=5.85h$ in Figure 10. This explains the dramatic changes in pressure distributions at the interface between pure fluids and the filter. The velocity profiles over

the upstream side of the filter are shown in Figure 5.13. Comparing Figure 5.13 and Figure 5.12, it may be observed that velocity cannot change as fast as the pressure does. The flow is considered incompressible because the velocity is much less than the speed of sound. The pressure therefore can change very fast, nearly in no time. However the velocity of the fluid cannot change instantly, since it takes time for momentum transfer. The velocity distribution maintains its shape and changes gradually. The pressure profiles change because the velocity profiles do not change when the relationship between the two changes. The reverse process happens when the fluids leave the filter. At the downstream part of the filter, the pressure and the velocity are both nearly uniform cross most of the channel, as shown at $x=8.55h$ in Figure 5.14 (velocity profile one grid upstream of the right side interface) and Figure 5.11(b) (pressure). Fluid flow follows the Darcy's law at the downstream interface; a nearly uniform velocity profile corresponds to a nearly uniform pressure profile in most parts of the channel except the wall region. They match well because of the development through the filter. In the channel flow downstream of the filter, pure fluids tend to have parabolic velocity and uniform pressure distributions. Then the pressure profile does not need to change since it is already nearly uniform while the velocity profiles change gradually back to parabolic. Because in pure fluids the viscous effects are dependent on the velocity shear, the velocity distribution changes the most where the velocity gradients are the largest. It is obvious that the velocity gradients are much larger near the wall, therefore the velocity changes the most at the wall region. It should be noted that the velocity profiles change much faster upstream of the filter than downstream of the filter in pure fluids. In Figure 5.13, the change covers a distance in x of $1.2h$ and in Figure 5.14, it covers a distance of $3.6h$, even

though the changes in Figure 5.14 are much smaller. This is because the filter produces large pressure changes upstream, which forces flow to change quickly.

Figure 5.13 shows the velocity distributions entering the filter. The interface of the filter and the pure fluid is at $x=5.85h$, where the velocity profile is nearly parabolic except at the wall region. At $x=5.55h$, one grid upstream of the filter, there is a small area of negative velocity near the $Y/h = 2$ upper wall, which is the non-step side. We can see the vortex at the non-step side in Figure 5.11(a) at the corner just upstream of the filter, though very small. However at the step side wall the reversing velocity area is smaller, barely existing at the location. At $x=5.85h$, which is the interface, the profile is flatter except near the wall. At the step side the velocity is positive very close to the wall, however the velocity is negative at a very small portion away from the wall around $Y=.15h$. This is very interesting since the flow field at the step side would be totally inside the separation zone of the non-filter flow. The filter's presence pushes the reattachment of the step side vortex upstream; it stops around the upstream interface. It is clearly shown in Figure 5.13 that the flow is accelerating in the region close to the wall, and that the acceleration is very strong inside the filter. This explains why the flow cannot separate once inside the filter. In contrast, at the non-step side the flow becomes separated upstream of the filter at the location where the non-filter flow is not separated.

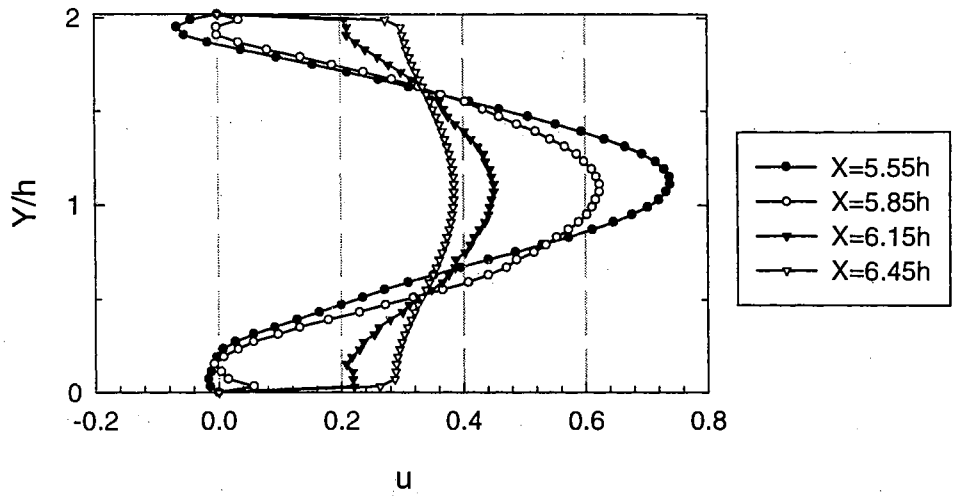


Figure 5.13. Velocity distributions entering the filter, filter's leading edge at 5.85h
 $Re=450$.

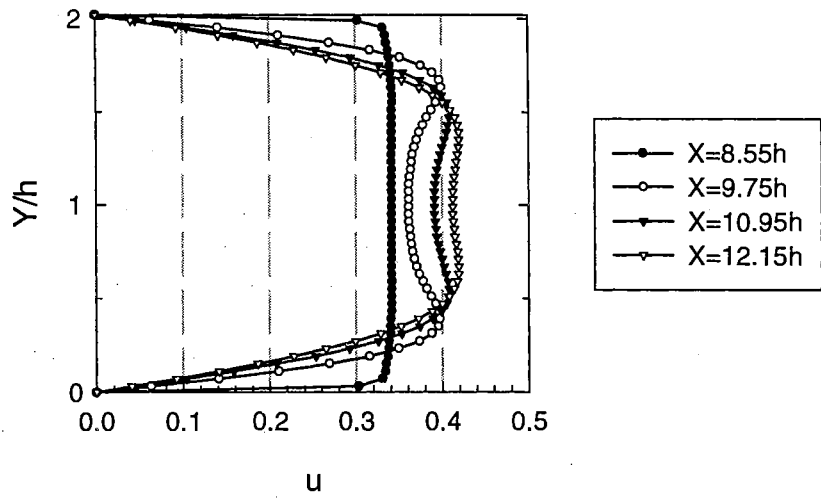


Figure 5.14. Velocity distributions after leaving the filter, filter's leading edge at 5.85h,
 $Re=450$.

Figure 5.14 depicts the opposite process as flow leaves the filter at the downstream side of the filter. The downstream interface between pure fluid flow and the filter is at $x=8.85h$. The $x=8.55h$ point is inside the filter, one grid upstream of the interface. The velocity profile is nearly uniform in most of the cross section. Very close to the wall the velocity gradient is very steep. This occurs because inside the filter the viscous resistance is mainly dependent on the velocity and the resistance produced by the Newtonian shear stress is much smaller. This may have two effects on the flow. Firstly the resistance that is proportional to velocity tends to make the flow uniform since the higher the velocity, the higher the resistance. Secondly the velocity gradient at the wall can be higher since the pure shear needed for the steep change of velocity produces a relatively small amount of resistance compared with the resistance from the filter. Once outside the filter, the profiles tend to be more and more parabolic.

Moreover, compare the two velocity profiles at the location upstream of the interface ($x = 5.55h$) in Figure 5.16. We found that the presence of the filter causes the maximum point of the velocity profile to move significantly from the non-step side in the direction of the centerline of the channel. This shift implies that the velocity increases in the step side where the flow is negative (inside the separation zone of the non-filter flow) and the velocity decreases at the non-step side where flow becomes separated due to the presence of the filter. This is still the same principle that the flow distribution becomes flatter when the filter is present; low velocities increase and high velocities decrease while the maximum velocity decreases. Compare the two profiles with the filter in Figure 5.15; one is one grid upstream ($x=5.55h$) of the interface and the other is two grids upstream ($x=4.95h$). We can see what is happening at the corner as the flow approaches

the filter. Roughly, the non-step side half of the flow is decelerating and the step side half of the flow is accelerating. This clearly explains why the flow at the step side is reattaching and at the other side is separating. At the Reynolds number 450, the non-filter flow is very close to separation at $x=5.5h$ of the non-step side. With the addition of the filter, the flow becomes separated.

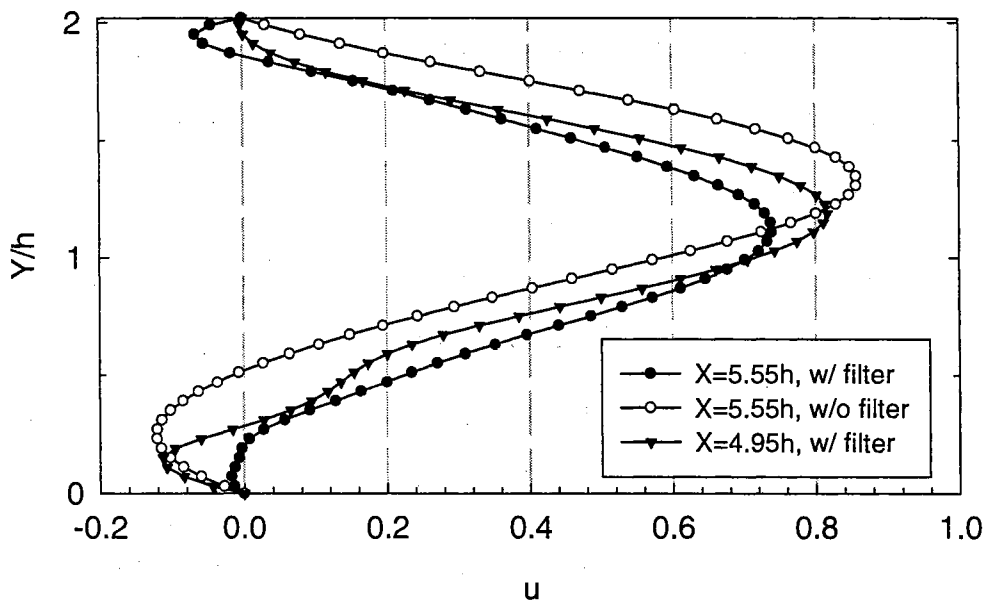


Figure 5.15. Velocity distributions upstream of the filter with and without the filter, filter's leading edge at 5.85h, $Re=450$

If the filter is placed even closer to the step at $x=2.85h$, deeper inside the recirculation region of the non-filter flow, similar results can be seen in Figure 5.16 to those when the filter is placed at $x=5.85h$. Figure 5.16(a) demonstrates the flow fields with the filter at $x=2.85$ to $5.85h$ for two Reynolds numbers, it indicates that the Reynolds number does not have much effect on the flow field for these conditions. Because the recirculation region would go much farther downstream than the location of the filter if there were no filter present, the development of the primary vortex at the step

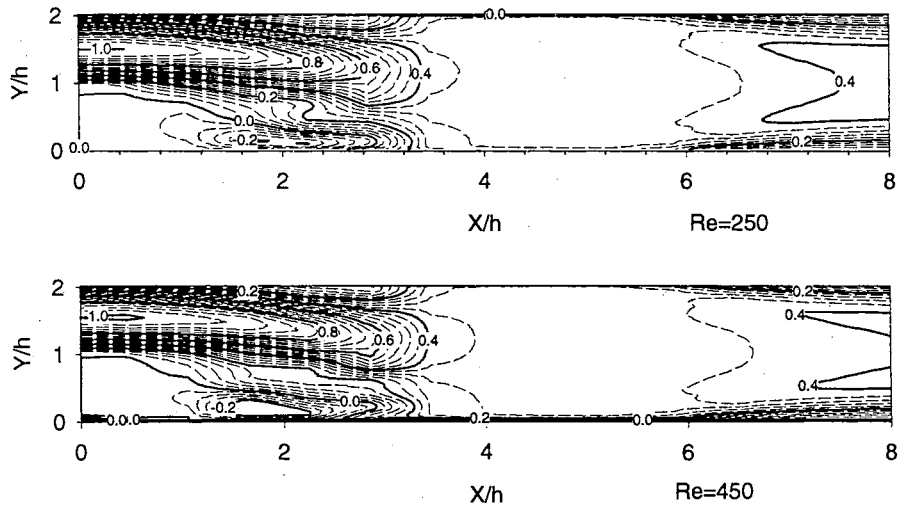
side is no longer very much controlled by the Reynolds number. The dominant factor is the interaction between the filter and the separated flow. Figure 5.16(b) demonstrates clearly that the velocity profiles at the upstream interface of the filter are basically similar. There are some outstanding differences at the regions near the two walls. At the non-step side wall, the area of reversing velocity at $Re = 450$ is much larger than at $Re = 250$, although both are small. At the lower step side wall, the flow of $Re=450$ is attached at the wall while the velocity is negative at a small area away from the wall. The front point (the downstream end) of the primary vortex is not at the wall and is beyond the reattachment location at the wall in Figure 5.16(a). This is also found in Figure 5.11(b) when the filter is placed at $5.85h$ at $Re=450$. The reason may be that the flow acceleration is not very strong around the point of $Y=.25h$ while the acceleration is much bigger at $Y=0.1h$, as shown in Figure 5.15 by the two profiles with the filter. The velocity profiles in Figure 5.16(b) do not show that at $Re=250$ the nose of the primary vortex moves away from the wall, because the nose goes further downstream than the flow of $Re=450$, which can be found in Figure 5.16(a).

When the filter is placed so close to the step, there is very little room for the separating flow behind the step to develop. The flow becomes unstable, even at a very low Reynolds number 250. The contour lines are not as smooth as they are when the filter is farther downstream. In all the u-contour plots, the labels on the lines are the velocity values the lines represent. The values are the non-dimensional velocity, which is normalized by the maximum velocity in the inlet, for instance .4 means the velocity on the line is $.4 U_{\max}$. The contour line of .2 at $Re=250$ has large wiggles at about $x=2.2h$, which is an indicator of instability in the region. For the flow at $Re=450$, the contour

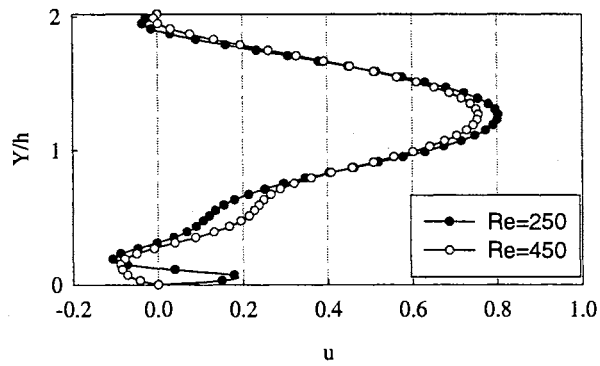
lines around the filter interfaces have small fluctuations, which is another indicator that the computed flow is not very stable at the current conditions.

When the filter is placed inside the recirculation region of the non-filter flow, the reattachment point is pushed upstream of the filter due to the flow acceleration there. The reversing area there is dramatically reduced compared with the case without the filter. The flow at the non-step side is likely separated upstream of the filter due to the deceleration at the region. The flow inside and downstream of the filter is smoother because of the filter. It appears that the separating flow does not penetrate into or pass through the filter.

Further study is needed to see if the wiggles found in the flow with the filter very close to the step, are due to the fluctuations of the flow or numerical instability.



(a) Velocity contour with filter at 2.85h to 3.85h



(b) Velocity distribution at $x=2.55h$, $3h$ upstream of the filter

Figure 5.16. Flow fields of different Reynolds numbers, filter's leading edge at 2.85h.

5.2.4 The Effect of Reynolds Number

For pure fluid flow at low Reynolds numbers, the reattachment length is dependent upon the Reynolds number. We already know that if the filter is placed far downstream, it does not have a significant influence on the reattachment length of the step flow. When the filter is placed close to the step, the flow reattaches just upstream of the filter. What will happen for different Reynolds numbers if the filter is placed at a fixed location? Figure 5.17 shows the reattachment length over a Reynolds number range of 100 to 800 with the filter placed at $9.45h$.

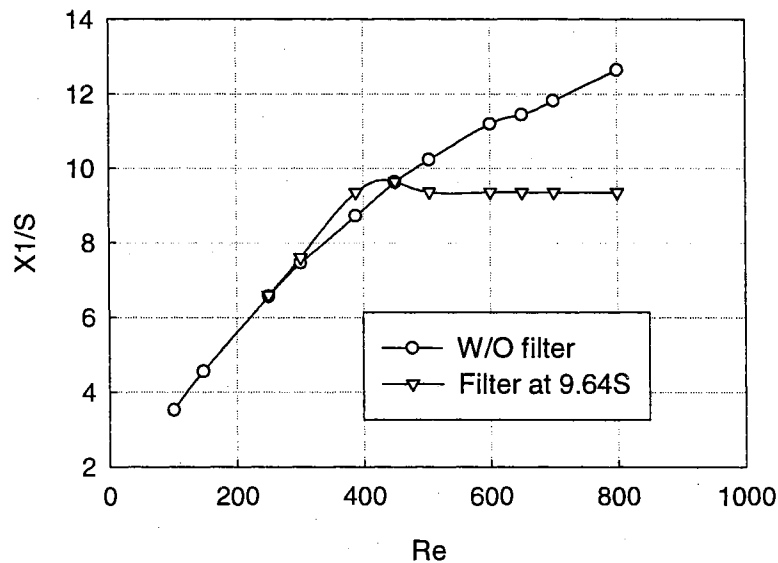


Figure 5.17. Reattachment length vs. Reynolds number with filter's leading edge at $9.64S$.

The location of $9.45h$ (h is the half width of the channel) is $9.64S$ (S is the step height) for the current configuration and about the reattachment length of the flow at $Re=450$. The computed reattachment length for non-filter flow varies between 3.5 to

12.5S for the Reynolds number range of 100 to 800. The 9.64S can provide different cases with the filter located far downstream of the reattachment point, deep inside the separation region and around the reattachment point as the Reynolds number increases from 100 to 800. Comparing the reattachment lengths of the flow with and without the filter as in Figure 5.17, the filter does not have a significant impact on the reattachment length at Reynolds numbers 300 and lower. This is the case of the filter downstream of the reattachment point. Additionally, there is no secondary vortex at the non-step side wall at such low Reynolds numbers. This agrees well with the results from previous sections. At Reynolds number 500 and above, the reattachment length becomes constant. The filter is at 9.64S; the separating flow stops at 9.32S. This is the case with the filter is placed inside the separation zone. The filter forces the flow to reattach upstream of it. However at Reynolds number 388, the reattachment length becomes larger due to the filter. The location of the filter is close to and outside of the separation zone. From Figures 5.16 or 5.2 we can see that without the filter the secondary vortex is at about 8.7S to 9.7S, which implies that the filter is inside the separation zone at the non-step side. Therefore the flow at the upper non-step side accelerates and the flow at the step side decelerates, so that the separation zone at the step side is enlarged. This is a case with the filter placed at the location where the non-filter flow is not separated at one side of the channel and separated at the other side. At previous sections, the results were mostly for one Reynolds number of 450. The conclusions from the previous sections can be confirmed here for different Reynolds numbers with the location of the filter fixed.

Our study has emphasized the effect of the filter on the primary vortex behind the step. It is also important to study how the secondary vortex would behave when the filter

is positioned at the non-filter flow vortex location. The locations and sizes of the secondary vortex are shown in Figure 5.18 with Reynolds number from 400 to 800. X4 is the upstream edge and X5 is the downstream edge of the reversing flow region at the non-step side.

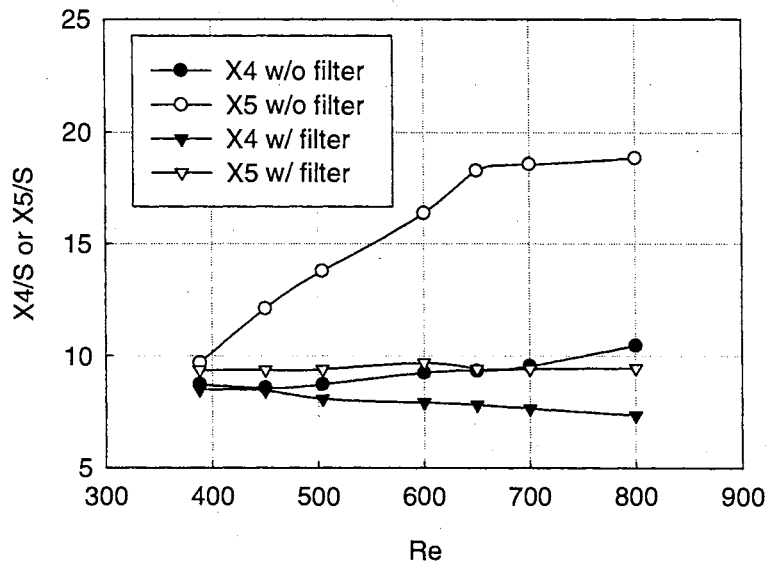


Figure 5.18. Locations of the secondary vortex vs. Reynolds number without and with filter, filter's leading edge is at 9.64S.

As for the case shown in Figure 5.17, the filter is placed at 9.64S (9.45h), which is inside the location of non-step side vortex of the non-filter flow. For Re=800, the filter is even upstream of the whole vortex of the non-filter flow. At Reynolds numbers lower than 350, there is no secondary vortex at the non-step side, so the Reynolds numbers here are 388 and above. At Reynolds number 388, the filter is not inside the primary vortex at the step side. At higher Reynolds numbers, we already know that the flow reattaches upstream of the filter. For the non-filter flow, X5 increases significantly as the Reynolds number increases, which indicates the downstream edge of the vortex extends to as far as 20 step heights. When the filter is placed at 9.64S, the separation flow does not go

beyond the filter; $X5$ is nearly a constant around $9.4S$. While the downstream edge of the vortex is fixed upstream of the filter, the upstream edge of the vortex is pushed upstream, as shown by $X4$ in Figure 5.18. For the non-filter flow, the vortex moves downstream as the Reynolds number increases, that is both $X4$ and $X5$ increase as the Reynolds number increases. However when the filter is placed at $9.64S$, the $X4$ values decrease slightly as the Reynolds number increases. This indicates that as Reynolds number increases the size of the vortex increases; the same trend as in the non-filter flow. Because the downstream edge of the vortex is fixed at the upstream of the filter, the vortex can grow only by moving upstream.

There is something new here. At Reynolds number 500 and above, the non-filter flow is separated at both sides of the channel at $9.64S$ and the flow becomes reattached when the filter is placed there. This is a case that is not covered in previous sections. It is well understood that the presence of the filter forces the flow to redistribute, the flow in the center decelerates and the flow at the sides accelerates. When the flow is separated at both sides, the acceleration will be very strong and can cause the separated flow to reattach as is shown in Figures 5.15 and 5.16.

5.3 SUMMARY

The following conclusions may be drawn from the computations of flows with Reynolds numbers 800 and less.

The difference method and the codes work properly for the two-dimensional backward facing step flows with and without the filter present. The computation predicts correctly and accurately the reattachment length and the location of the secondary vortex at low Reynolds numbers compared with existing experimental results of pure fluid flows.

When the filter is placed at a location where the non-filter flow is not separated, the introduction of the filter does not affect the properties of the upstream separated flow very much. The filter forces the flow immediately upstream of it to redistribute, the velocity in the center decreases and the velocity near the walls increases.

Separating flow does not appear to penetrate into the filter. If the filter is placed at the location where the non-filter flow is separated at one side and not separated at the other side, the separated flow reattaches and the flow at the other side separates because of the presence of the filter. The reattachment of the separated flow is a result of the acceleration at the side of the channel and the separation at the other side is caused by the deceleration required to maintain the constant flow rate.

When the filter is placed very close to the step, where a large part of the cross section would be reversing flow at the step side for the non-filter flow, the separated flow stops upstream of the filter. The secondary vortex is pushed upstream toward the inlet, its downstream edge ends upstream of the filter while its upstream edge moves upstream as the Reynolds number increases.

CHAPTER VI

EXPERIMENTAL RESULTS OF STEP FLOW WITH FILTER

The interaction between the separated flow and the filter is very interesting and there has been little study of the issue in the past. We have some results from by the CFD model in the previous chapter, but we will have more confidence in them if they can be verified by experiment. A wind tunnel with a transparent test section that incorporates a two-dimensional backward facing single step; as shown in Figure 2.3 was designed and constructed to conduct such experiments. The aspect ratio is 1:2, so the step height is the same as the half width of the channel h , which is 25 mm. The filter was placed at two locations relative to the step. The velocity profiles upstream of the filter will be presented and the effect of the filter on the flow field is studied by comparing the profiles with the filter and the profiles without the filter. The separation region is significantly altered when the filter is placed close to the step, in the region that separation occupies in the non-filter case. More interesting phenomena are found when the filter is placed further downstream, where it is close to the reattachment locations of the non-filter flow.

The coordinate system for the step is the same as in the previous chapters, as shown in Figures 1.2 and 3.1. The z -direction is the direction that is perpendicular to the step plane (x - y plane), which is referred as the span-wise direction.

6.1 INLET FLOW

The flow two-dimensionality is examined by measuring the velocity profiles at the inlet centerline in the span-wise direction (normal to the step plane) in the range of more than 10 times the step height. As shown in Figure 6.1(a) for Reynolds number 2000, the deviation of the mean velocity in the z direction from the average velocity of all points measured along the z-axis (in the span-wise direction) is within $\pm 5\%$. The RMS (root mean square) velocity distribution is not scattered very much, as shown in Figure 6.1(b). The values are about 0.8% along the z-axis, which further indicates that the flow is two-dimensional.

The results in Figure 6.1 are for the lowest Reynolds number of the four Reynolds numbers studied. Measurements demonstrate that at higher Reynolds number the velocity distribution in the z-direction is also uniform and the maximum deviation from the mean is less than 0.5%. This is quite adequate for the present study. At the highest Reynolds number, 10000, the fluctuations (RMS over the mean velocity) are larger than at $Re=2000$. At the upper two thirds of the channel they are less than 1%, at the other part of the channel the RMS is less than 1.6%.

At lower Reynolds number (1,500 and less) the inlet flow is not two-dimensional to acceptable accuracy. This is most likely caused by the introduction of the seeding for LDA measurement, since the airflow carrying the seeding particles is not introduced into the flow uniformly in the span-wise direction, as shown in Figure 3.3. The velocity at the entrance of the channel is very small, about one tenth of the average velocity at the inlet of the step. If the Reynolds number is 1500, the average velocity at the inlet is about 0.8 m/s. The velocity at the entrance of the channel is about 0.08 m/s.

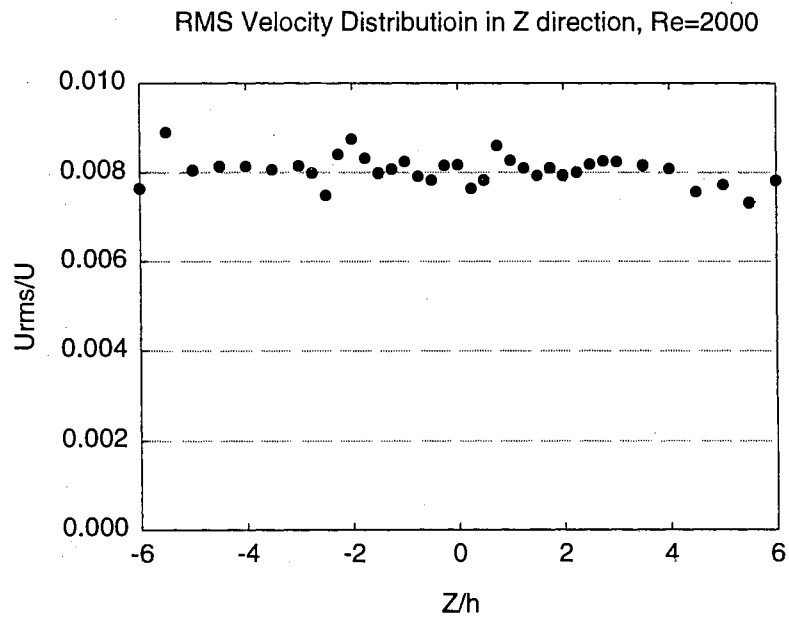
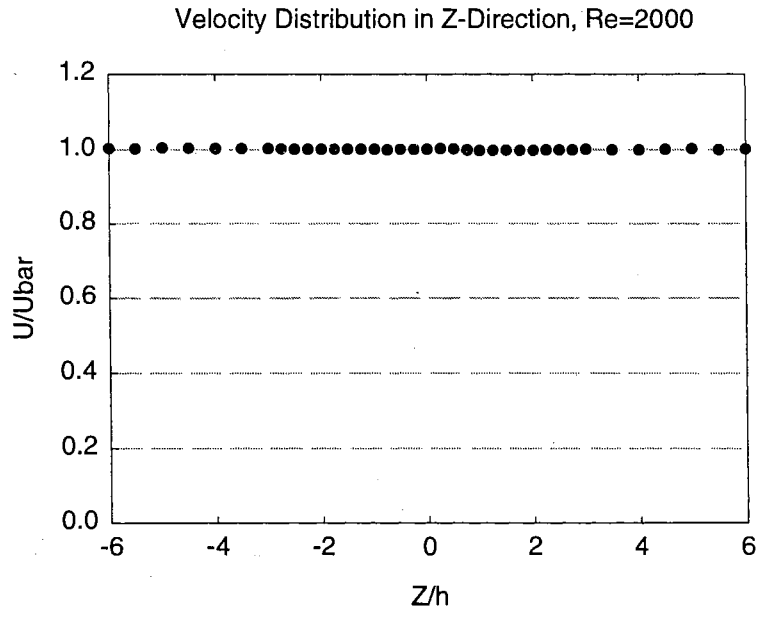


Figure 6.1. Two dimensionality of the inlet flow, $x=0$, $y=.5h$.

For such a slow flow, small disturbances may alter the velocity distribution at the channel entrance and the variations is not smoothed since there is little mixing in the developing section at such small velocities. This will result in either corrupt inlet velocity profiles in the vertical direction or non-uniformity in the spanwise direction. It is a remaining problem how to introduce particles and maintain the two-dimensional flow at the wind tunnel entrance at low Reynolds numbers.

The inlet velocity profiles in the vertical direction (across the section) are shown in Figure 6.2 for all the four Reynolds numbers. The profiles are normalized by their maximum velocities for easy comparison. At the Reynolds number 2,000 the inlet profile is very close to parabolic, the profile of fully developed laminar channel flows. It is just a bit flatter than the dotted line, which is derived from the equation: $1 - 3.5(Y/h - .5)^2$. This indicates the length of the development section is marginally proper for the Reynolds number to achieve fully developed flow at the entrance. It also implies that the length is proper for higher Reynolds number since it requires less length for higher Reynolds number flow to fully develop due to the stronger shear and mixing. As the Reynolds number increases the profile is getting flatter and flatter in the center. Consider that the velocity at the wall ($Y/h = 0$ or 1) is zero, the velocity gradient at the wall region increases significantly as the Reynolds number increases. It should be noted that the inlet flow is not the same as the flow downstream of the step, since the step is a very big disturbance to the flow downstream. In the experiments of Armaly et al. (1983) the flow downstream of the step becomes fully turbulent at Reynolds number 6,600 and transitional at Reynolds number 600. That does not imply the flow at the inlet is fully turbulent or transitional at the Reynolds numbers.

From Figures 6.1 and 6.2 we can conclude that the inlet flow is two-dimensional and symmetric in the vertical y -direction for the present Reynolds number range. It completely satisfies the design criteria described in chapter 3.

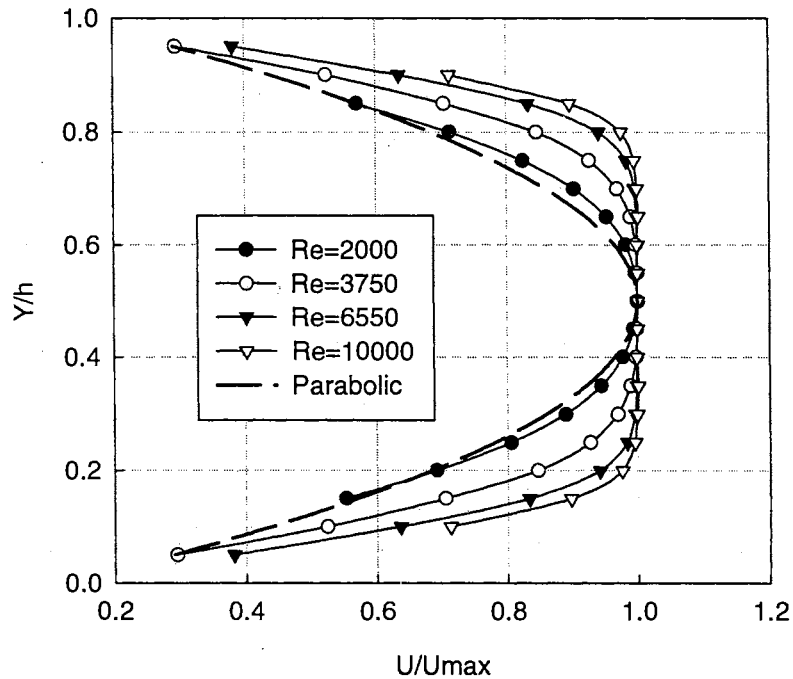


Figure 6.2. Inlet velocity profiles at different Reynolds numbers.

6.2 FLOW FIELDS WITH FILTER PRESENT

It is expected that the filter has little impact on the flow field upstream when it is placed far downstream. The CFD results in the previous chapter, performed at low Reynolds numbers, have shown that. Similar results can be found in the computations of Liu (1995) in a channel flow. He stated that the velocity distributions upstream of the filter are not altered by increasing the pressure drop of the filter in a very large range. Therefore the case with the filter far downstream of the step is not studied here. In the

present study the filter is first placed in the field at $6.75h$ behind the step, where it is close to the reattachment locations of the non-filter flows. Since in the range of the Reynolds numbers here the reattachment length varies with the Reynolds number, $6.75h$ provides cases for which the reattachment length of the non-filter flow is larger or shorter than the distance of the filter from the step. We do not have the case that the filter is placed exactly at the reattachment location because it is too delicate to adjust the Reynolds number to match the reattachment location with the filter since the flow is transitional; its dependence on Reynolds number is not monotonic. To study the stronger interactions between the reversing flow and the filter, the filter was then moved closer to the step at $4.25h$. In the present Reynolds number range, the reattachment lengths of the non-filter flow are far larger than that.

At $Re=2,000$ to $10,000$, the flow behind the step is in the transitional and then turbulent regimes, according to Armaly et al. (1983). In this range the flow undergoes many changes, which provides a chance to study different flow patterns although the filter is only placed at one of the two places. At each Reynolds number, the flow has some distinguishable properties. The results will therefore be presented by Reynolds number. The instantaneous reattachment points and the separation lines at those Reynolds number range are not still. The results presented later in this chapter are all obtained from mean velocity fields. The mean velocity is measured over a time period that is more than 100 times the characteristic time scale of the flow, defined by the step height divided by the maximum inlet velocity. The reattachment points and the separation lines are therefore the mean locations, which are steady. The mean flow fields are also representative of the overall effects of the filter.

6.2.1 Measured Flow Field of Step Flow at $Re=2000$.

In the present experiments, the reattachment point was not measured. Instead the separation lines were measured in the flow field. These lines, where stream-wise mean velocity is zero, are shown for the different cases in Figure 6.3. $Y=0$ is the step side wall, $Y=h$ is the location of the step edge and $Y=2h$ is the upper, non-step side wall. X is the distance from the step. The separation starts at the step edge, where $X=0$ and $Y=h$. The locations of zero velocity are found by interpolation between two adjacent points of opposite signs in the mean velocity profiles, assuming linear velocity distribution between the two points. Velocity profiles were measured at the vicinity of the separation line, not throughout the channel. The increment between two measured points is $.05h$, which insures the location is determined accurately.

There are two reasons we measure the separation lines instead of reattachment locations. One is that it is very difficult to detect the location of the reattachment. The velocity in the wall region is very small and the LDA signals are not good there because of the strong reflection from the wall. In the experiments of Armaly et al. (1983), an integration was used to project the reattachment point, which is theoretically defined as the location where the velocity gradient is zero at the wall. The direct approach to measure the velocity gradient at the wall by LDA is to find the velocity value at a point as close to the wall as possible. Knowing the velocity is zero at the wall, the gradient can be obtained assuming a linear velocity distribution between the measured point and the wall. There will be large errors if we cannot measure the velocity extremely close to the wall accurately. When a filter is placed in the flow field, it is extremely difficult to get reliable LDA measurements at the corner of the wall and the filter. Furthermore, the shape of the

entire vortex gives more information about the interaction between the filter and the recirculating flow.

Figure 6.3 demonstrates the effects of the presence of the filter on the shape of the step side (the primary) vortex. These separation lines do not tell the exact size of the vortex, however provide good indications of its size. Under the lines is the area of the mean reversing flow. When there is no filter placed in the field, the separation line is beyond seven at $Y=0.2h$. The reattachment will certainly happen downstream of $7.5h$ since the separation line has not dropped sharply, as it should at the vicinity of the reattachment location, where the vertical velocity gradient is close to zero. Because at $X=8h$ of the test section there are flanges that block LDA laser beams, there are no measurements downstream of $x=7.5h$.

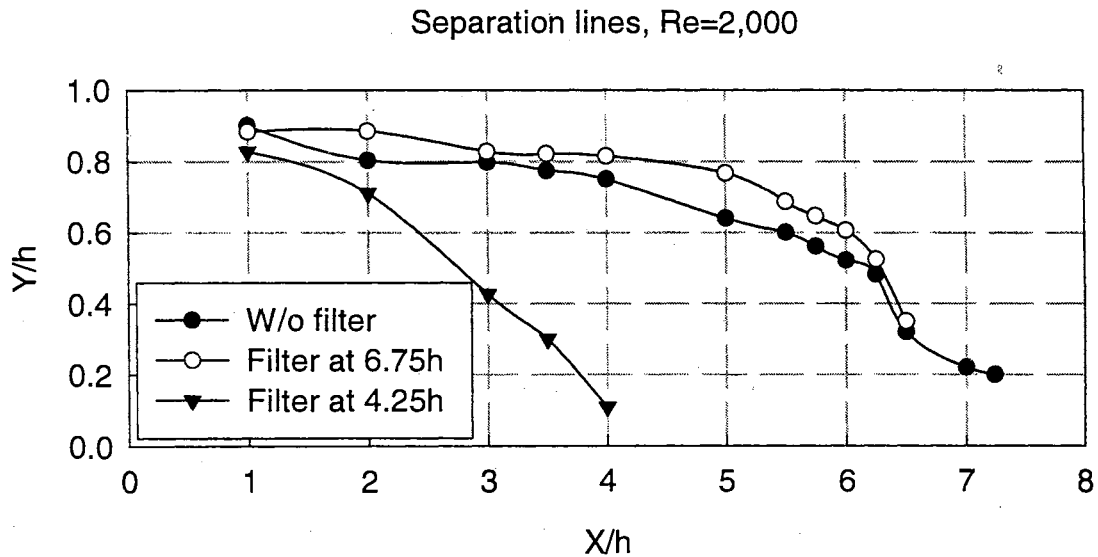


Figure 6.3. Separation line of the primary vortex at $Re=2000$.

When the filter is placed at $X=6.75h$, the separation line is higher from the step to $X=6.5h$, which indicates that the vortex is bigger in the region close to the step.

Downstream of $X=6h$, the line drops sharply, implying that it is close to the nose of the vortex at $x=6.5h$. Since the filter is at $X=6.75h$, the closest point that can be measured is at $6.5h$. We can only predict from the shapes of the two separation lines that the reversing flow most likely stops at the filter. The two lines are close, the difference is within the error bar for the measurement. However collectively all the points except the first two at the left side indicate that with the filter the reversing area is smaller. It will make a stronger case when the filter is placed at $4.25h$. It is clearly demonstrated that the reversing flow stops at the filter. The size of the vortex is considerably reduced both in the vertical and the horizontal directions. At $x=4h$, the closest measured point to the filter, the separation is at $.1h$ away from the wall. This indicates that the reversing flow is in a very small region immediately upstream of the filter if there is any.

The three separation lines in Figure 6.3 strongly suggest that the separating flow does not go beyond the filter. When the filter is at $6.75h$, the flow appears to reattach around $6.5h$. When the filter is placed closer to the step at $4.25h$, the separation stops around $4h$. This agrees with the CFD results in the previous chapter, even though the Reynolds number is 2000 for the experiment and less than 800 for the computations.

To study more about the effects of the filter on the flow field, velocity profiles are measured at $.5h$ upstream of the filter. Compared with the velocity profiles that are measured at the same location without the filter present, as shown in Figure 6.4, the effects of the filter are not very significant at this condition. There are hardly any effects on the RMS (root mean square) velocity, which represents the velocity fluctuations.

In the experiments the two Reynolds numbers for the flows with and without filter are not exactly the same, since the introduction of the filter requires adjustment in the

controlling valves of the blower controller. In the cases presented here that difference is controlled within 1% of the value of the Reynolds number. This implies that there is a very small difference between the maximum inlet velocities, which is used to calculate the Reynolds numbers. To assure the difference will have a minimum effect on the comparison, all the profiles are normalized by the maximum inlet velocity. Since the test channel is wider than the inlet channel, the maximum velocities in the profiles are all less than one.

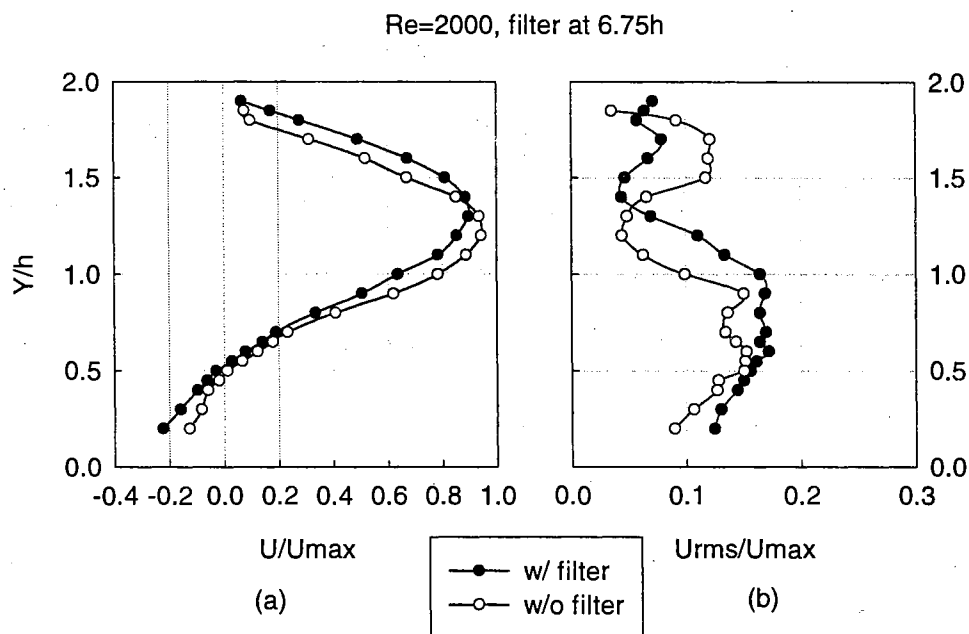


Figure 6.4. Velocity distributions at $x=6.25h$ without filter and with filter at $6.75h$, $Re=2000$.

In the velocity distributions of Figure 6.4, the profile with the filter at $6.75h$ shifts a bit, compared with the profile without the filter, to the upper non-step side, $Y=2h$. The velocity increases approximately at the one third upper side (non-step side) and the velocity decreases at the lower side, that is the step side of the channel. This is in line with the results of the separation line, which indicated that the primary vortex is getting

thicker in the vertical direction. It agrees well qualitatively with the CFD results of Chapter 5 that the separation zone increases when the velocity decreases.

When the filter is placed closer to the step, its effect on the flow field is much larger, as already shown in the separation lines of Figure 6.3. Figure 6.5 depicts the velocity distributions $.5h$ upstream of the filter for the flow with the filter present at $x=4.25h$ and without the filter present. The same as the case when the filter is placed at $6.75h$, the fluctuation (RMS velocity) is nearly the same with and without the filter present, although this time the velocity profiles and the separation zone are greatly altered by the filter. The velocity profile with the filter is nearly symmetric with respect to the centerline. Surprisingly there appears little effect of the step, which is supposed to make the flow domain unsymmetrical. When the filter is not placed in the field, at $x=3.75h$ the profile shows that about one third of the flow at the step-side is reversing flow (negative streamwise velocity). The maximum velocity is at about three-quarters of the channel width away from the bottom (step side) wall. The profile appears symmetric in the upper half (non-step side) of the channel with respect to the maximum velocity. Because of the presence of the filter, the velocity decreases a great deal at the upper side and increases at about the same amount at the step side. Additionally the maximum velocity of the profile with the filter is much smaller than that of the profile without the filter. The velocity at the non-step side of the channel, where the non-filter flow velocity is larger, decreases while the velocity at the other side increases. This implies that the filter tries to even the flow across the channel as found by the CFD models in the previous chapter in laminar flows. Because of the dramatic increase of velocity at the step side, the flow becomes more favorable to reattachment and the reversing flow area reduces from about $.8h$ to

.25h. On the other side where the velocity decreases considerably, the flow becomes separated because of the deceleration due to the filter. We can assume that the farther upstream of the filter, the less the effects of the filter on the velocity profiles. The velocity profiles farther upstream with the filter present should be like something between the profiles at 3.75h with and without the filter. The current profiles without the filter can therefore to some extent suggest the profiles upstream with the filter. Thus we can analyze the profile changes in the streamwise direction for flow with the filter by comparing the profiles with and without the filter at one location.

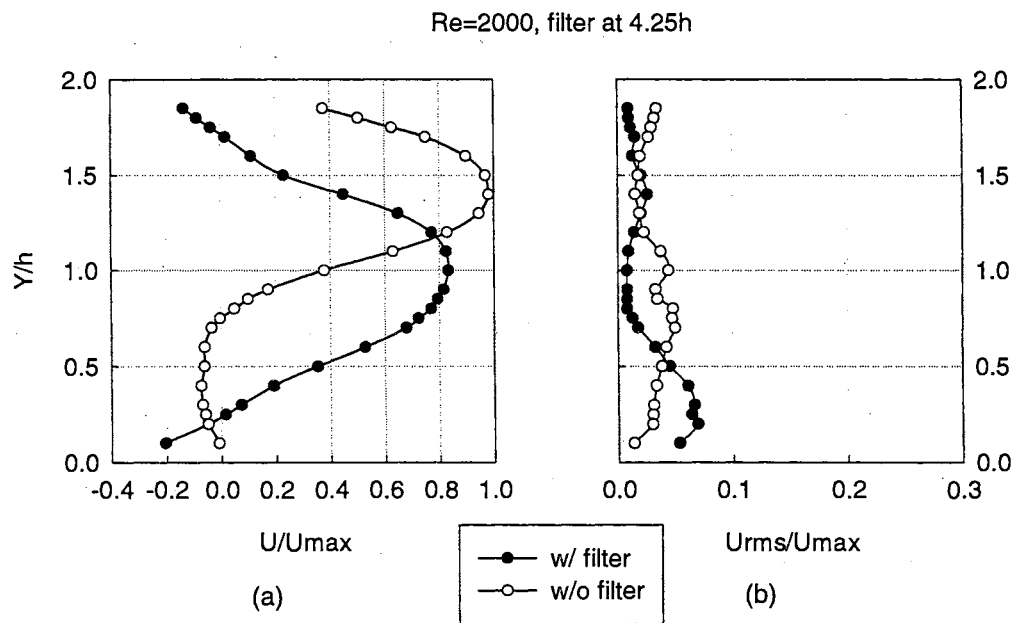


Figure 6.5. Velocity profiles at $x=3.75h$ without and with the filter at $4.25h$, $Re=2000$.

Inside the reversing flow area, the maximum reversing velocity is greater with the filter than without the filter, as shown by Figure 6.5. The velocity gradients are larger with the filter and the RMS velocity is a bit larger due to the increase of the velocity gradient $\frac{\partial u}{\partial y}$. When the velocity gradient is larger, the turbulence energy production term

$(\overline{u'v'}) \frac{\partial u}{\partial y}$) will be larger. Then the flow at that location will tend to have larger RMS

velocity. The velocity gradient increase is the result of the shift of the maximum velocity to this side of the channel, which makes the velocity gradient larger in the whole half channel and the momentum transfer stronger.

From the analysis above, we can come to some conclusions for this Reynolds number. Introducing the filter into the flow field alters greatly the shape and size of the primary vortex. At 4.25h, close to the step, the filter makes the velocity profiles broader, significantly increasing the velocity at the step side and decreasing the velocity at the other side of the channel. In the process the primary vortex is reduced dramatically in size and at the non-step-side the flow becomes separated. There is a small change in the RMS velocity distributions, however it is not very significant. When the filter is placed at 6.75h, the primary vortex becomes wider (larger in vertical direction) and shorter (smaller horizontally). There is some change, though not as dramatic, in the velocity distribution .5h upstream of the filter because of the filter. The velocity increases at the non-step side of the channel where the velocity is in average much larger than the velocity at the other side. The velocity at the other side decreases. This is different from the case with the filter at 4.25h.

6.2.2 Measured Flow Field of Step Flow at Re=3750

At Reynolds number 3750, the flow without the filter is very different from the flow of Re=2000 at the location of $x=6.25h$. Although the filter is still placed at the same location its effect on the flow is very different, as shown in Figure 6.6. In all the figures in this section, $Y=0$ is the step-side wall. At this Reynolds number the flow without the

filter is not separated at $x=6.25h$ on the step side, however it is separated on the non-step side as the velocity profile indicates. As the filter is placed at $6.75h$, the velocity profile at $x=6.25h$ is greatly altered, unlike the cases of $Re=2000$. The profiles are nearly the mirror images of each other.

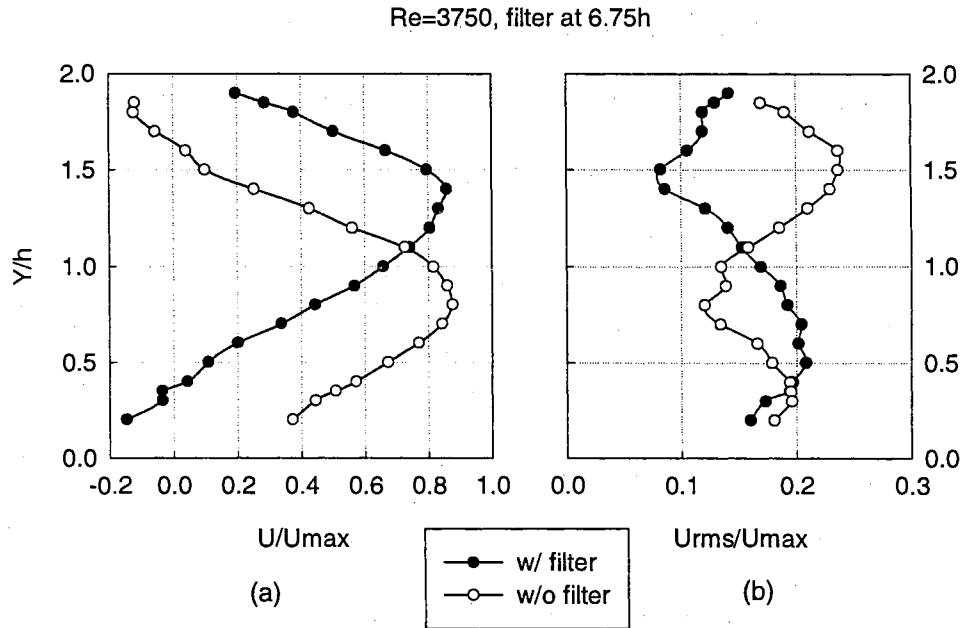


Figure 6.6. Velocity profiles at $x=6.25h$ without and with the filter at $6.75h$, $Re=3750$.

At the step side half, where there is no reversing flow for the non-filter case, the velocity decreases and the flow separates. On the other side of the channel velocity increases a great deal and the flow becomes reattached from reversing flow because of the filter. The RMS velocity is about the same at the step side and it is reduced a bit at the non-step side because the filter removes the reversing flow there.

Although this appears very different, it is still working in the same principles as at lower Reynolds numbers. However, in this case the separation is at the non-step side of the channel. When the filter is introduced into the field, it accelerates the flow at the

lower velocity side because it decelerates the flow at the higher velocity side. At the non-step side, we can see from the profile of the non-filter flow that the reversing flow penetrates into the flow field about $.4h$ from the wall. This implies that the location of the filter is inside the separation area of the non-filter flow. It is similar to the situation at the step side in the case of $Re=2000$ with the filter placed at $4.25h$, when the flow acceleration reduced the reversing area significantly. The difference here is that the reversing flow is not as strong as behind the step. Therefore the flow acceleration removes the reversing flow entirely.

At the current condition, the reversing flow at the step side is reattached at about $x=6.0h$ when the filter is not present, as shown by the separation line in Figure 6.7. When the filter is placed at $6.75h$ behind the reattachment point, the flow is decelerating at the step side, which promotes separation, so the separating flow extends further downstream of $6.25h$. It is clearly demonstrated in Figure 6.7 that the separation zone is much longer and wider when the filter is placed at $x=6.75h$ compared to the flow without the filter. This is a special case with the filter placed at the location about $.5h$ downstream of the reattachment point when the filter is not present. The results indicate that the filter enlarges the primary vortex. However since it happens that the other side of the channel flow is separated, this may affect the balance of acceleration and deceleration caused by the filter. It is not clear yet whether these two events are connected or independent of each other. At the step side the pressure increase due to the filter may enlarge the reversing area upstream, which implies flow deceleration there. The deceleration at the step side may induce the flow acceleration at the other side of the channel, which eliminates the reversing flow. On the other hand, the flow redistribution caused by the

filter implies deceleration in the center of the channel and acceleration at the two sides near the wall. However the acceleration at the upper wall may be stronger than at the other side because of the reversing flow at the upper wall. This may change the balance of continuity in the entire cross section and force the flow at the other side to decelerate rather than accelerate. Since it could be explained either way, the problem needs more study.

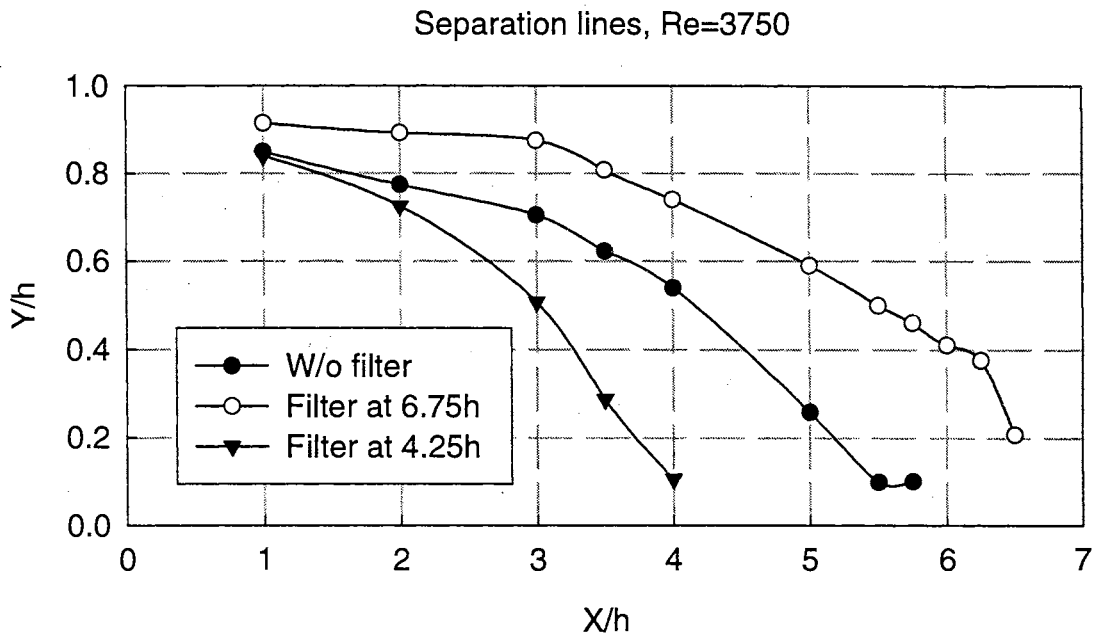


Figure 6.7. The separation lines of flows with and without filter, $Re=3750$.

When the filter is placed at $x=4.25h$, its effect on the separation line is nearly the same as at Reynolds number 2000. As shown in Figure 6.7, the reversing flow area is considerably reduced and the reattachment location is at about the same location as the filter. The velocity and its RMS distributions at $.5h$ upstream of the filter are shown in Figure 6.8. The velocity profile of the non-filter flow is similar to that of $Re=2000$, but the reversing flow area is much smaller at this Reynolds number. Although the profile

without the filter does not have negative values at the non-step side, the velocity at $Y=1.9h$, the one at the top end, is nearly zero. It indicates that the flow is likely separated between this point and the wall at $2.0h$.

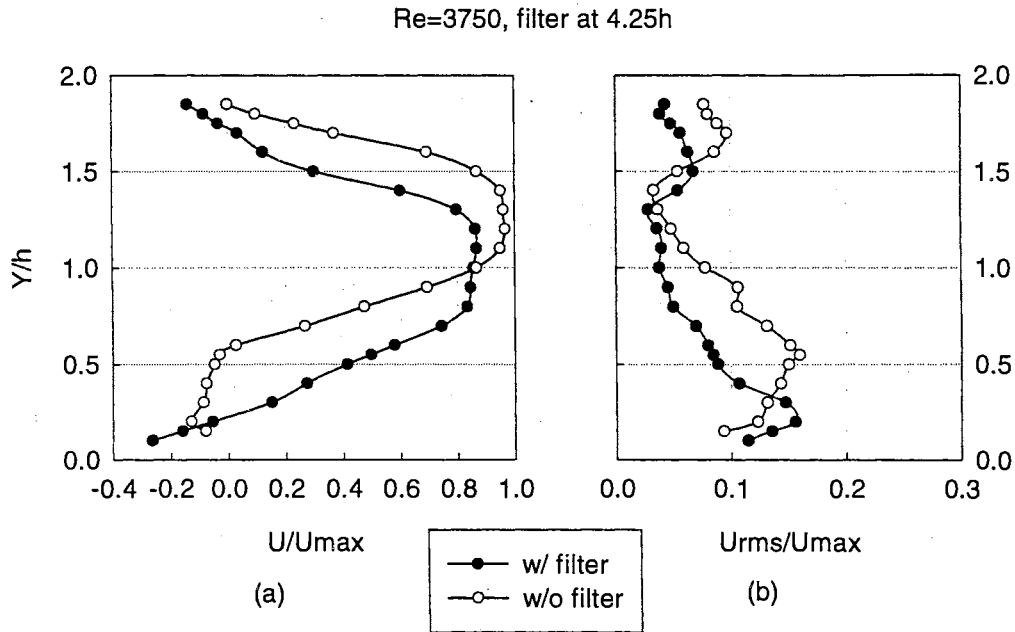


Figure 6.8. Velocity profiles at $x=3.75$ without and with the filter at $4.25h$, $Re=3750$.

The velocity profile with the filter is nearly symmetric with respect to the centerline. There are reversing flows of substantial sizes at the walls of both sides. The fluctuating velocity (RMS) profiles are nearly the same with and without the filter

6.2.3 Measured Flow Field of Step Flow at $Re=6550$ and $Re=10000$

At the Reynolds number 6600 and above the flow behind the step should be fully developed turbulent as stated in Armaly et al. (1983). The present experiment results show that at $Re=6550$ and 10,000, the properties measured here do not change much with Reynolds number. This agrees with Armaly et al. (1983). Therefore primarily the results

of 6550 will be analyzed, since similar results can be found for $Re=10,000$. Figures showing the results at $Re=10,000$ will be presented briefly at the end of this chapter.

When there is no filter in the flow field, the reattachment lengths for the two Reynolds numbers are about 6 step heights. This is different from Armaly et al. (1983), who found that the reattachment length for fully developed turbulent flow is about 8 step heights. The aspect ratio here is 2 and in Armaly's experiments it was 1.94. There are many factors that can affect the reattachment length. The inlet velocity profiles and the magnitudes and distributions of the fluctuating velocity definitely have influences on the separation development behind the step. The present velocity and RMS velocity profiles at the entrance are not likely to be the same with Armaly et al. Additionally the RMS velocity may be larger than Armaly et al. Those data are not found in the paper of Armaly et al., so that further analysis cannot be conducted. However it is not critical here since we are interested in the interaction of the filter and the separated flow, not the reattachment length. The effects of the presence of the filter on the separating flow are studied by placing the filter relative to the reattachment locations, which are determined by measured velocity profiles. The flows with and without the filter are the results of the same inlet conditions, the comparisons of the two flows give the difference caused only by the presence of the filter. The relationship between the reattachment length and the Reynolds number should not have any influence on the mechanism of the interaction between the separating flow and the filter, as long as the locations of the reattachment are the real locations for the flow.

Since the reattachment length is about $6h$, the filter is outside the separation region when it is placed at $6.75h$. This is similar to the case of $Re=3750$ when the

reattachment length is also about $6h$. However there is one big difference; no separation is found at the non-step side of the channel at these two Reynolds numbers of 6550 and 10000. According to Armaly et al. (1983), the flow is turbulent at the Reynolds number, and the non-step side vortex does not form.

Unlike the flow at $Re=3750$, the filter has little impact here on the flow field $.5h$ upstream when it is placed at $6.75h$. As in Figure 6.9(a), the velocity and its RMS profiles are practically the same with and without the filter in the field. However, when the filter is placed at $4.25h$, the same major effects are obtained as for lower Reynolds numbers. The reversing flow area is greatly reduced and it appears to stop at the filter. The velocity profiles at $.5h$ upstream give the same results as the other Reynolds numbers. The results are shown in Figure 6.9(b). From the separation lines of Figure 6.10 we can note that the presence of the filter enlarges the reversing flow area a bit in the vertical Y-direction. However around the reattachment point at $6h$, the two lines with the filter at $6.75h$ and without the filter nearly merge as one. That indicates that the filter has some small effects on the flow field upstream, but has no impact on the reattachment of the separated flow if it is placed outside the circulation zone. However at $Re=3750$, the filter enlarges the primary vortex when it is placed outside the recirculation zone. At that Reynolds number, the non-filter flow at the non-step side is separated at the location of the filter other than attached at the higher Reynolds numbers. Thus at $Re=3750$, the enlargement of the reversing area at the step side is a result of the elimination of the separating flow at the non-step side wall due to the introduction of the filter.

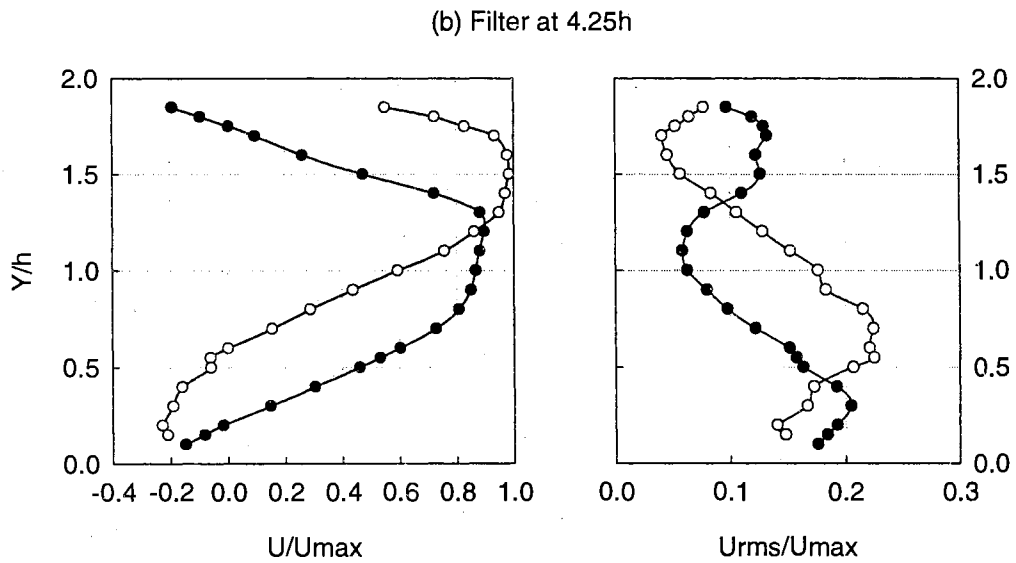
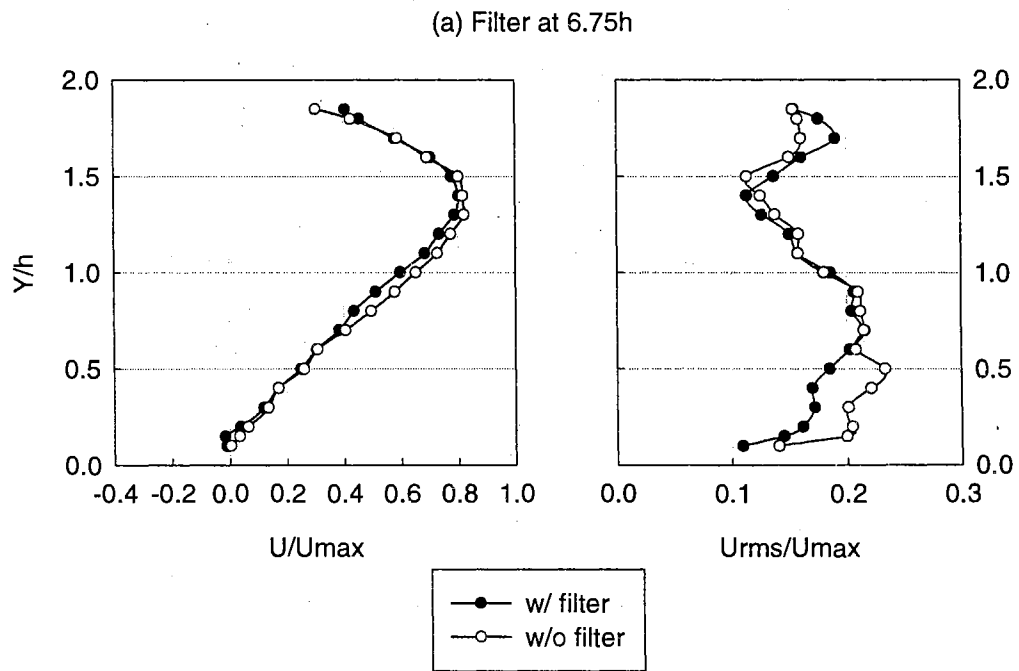


Figure 6.9. Velocity profiles .5h upstream of the filter with and without the filter, $Re=6550$. (a) Filter at 6.75h. (b) Filter at 4.25h.

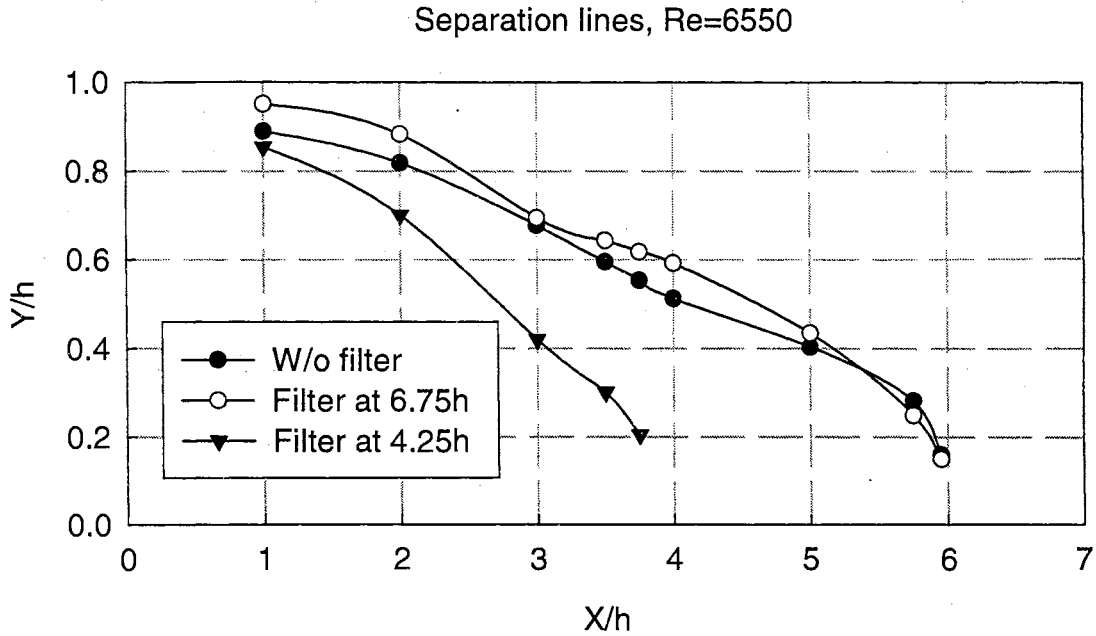


Figure 6.10. The separation lines of flows with and without the filter, Re=6550.

6.2.4 The Dependence of the Separation Areas on Reynolds Number

It is well understood that the recirculating flow depends on the Reynolds number in the laminar and transitional regimes. The fully developed turbulent flow is expected to have the same reattachment lengths independent of the Reynolds number, as stated by Armaly et al. (1983). However the reversing areas may vary because of the stronger momentum transfer at higher Reynolds numbers.

Figure 6.11 depicts the separation lines of the primary vortex at the step side for different Reynolds numbers when the filter is placed at 6.75h. The reversing flow area is defined as the area under the separation lines, where the velocity is negative. It shows clearly the trend that the reversing flow area decreases as the Reynolds number increases, although the filter at 6.75h confines the reattachment location at the filter or upstream. When the filter is placed at 4.25h, as shown in Figure 6.12, the Reynolds number does

not affect very much the main properties of the flow even at lower Reynolds number. The interaction between the filter and the step side primary vortex dominates the flow patterns.

In Figure 6.12 we can see that the separation lines are nearly the same for the three Reynolds numbers. At all four Reynolds numbers the separation lines join at $x=4h$, which may imply the same reattachment locations for the different Reynolds numbers. However at the highest Reynolds number, 10,000, the separation line is closer to the side wall, indicating a smaller reversing flow area. This is likely because the stronger shear at $Re=10,000$ leads to more momentum transfer and results in a flatter velocity profile in the center and higher velocity gradient in the wall region. The tendency can also be found in Figure 6.5 and 6.8 at Reynolds numbers of 2000 and 3750.

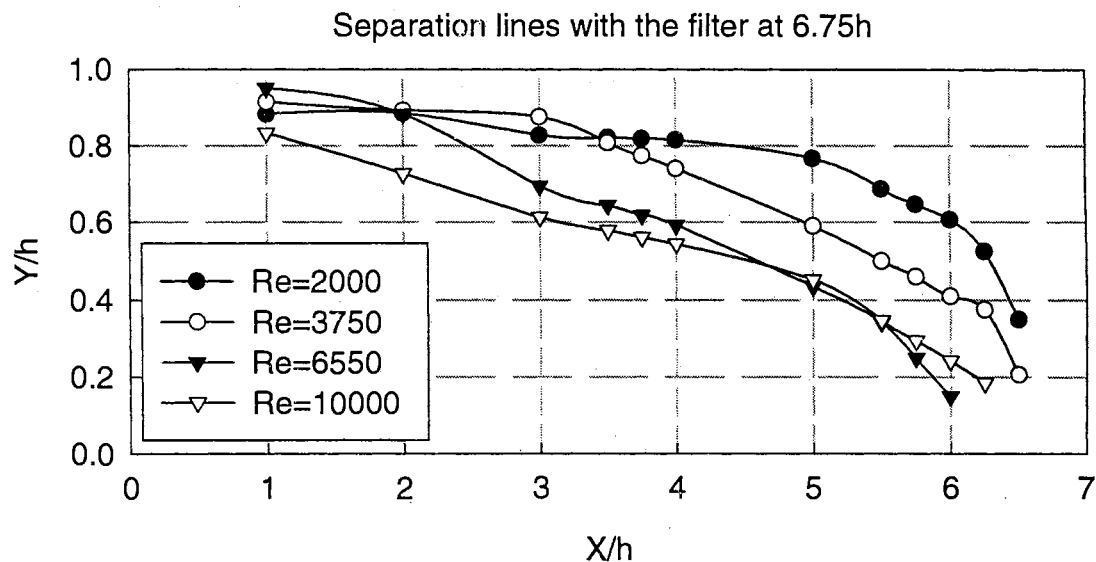


Figure 6.11. The dependence of the separation line on Reynolds number, filter at 6.75h.

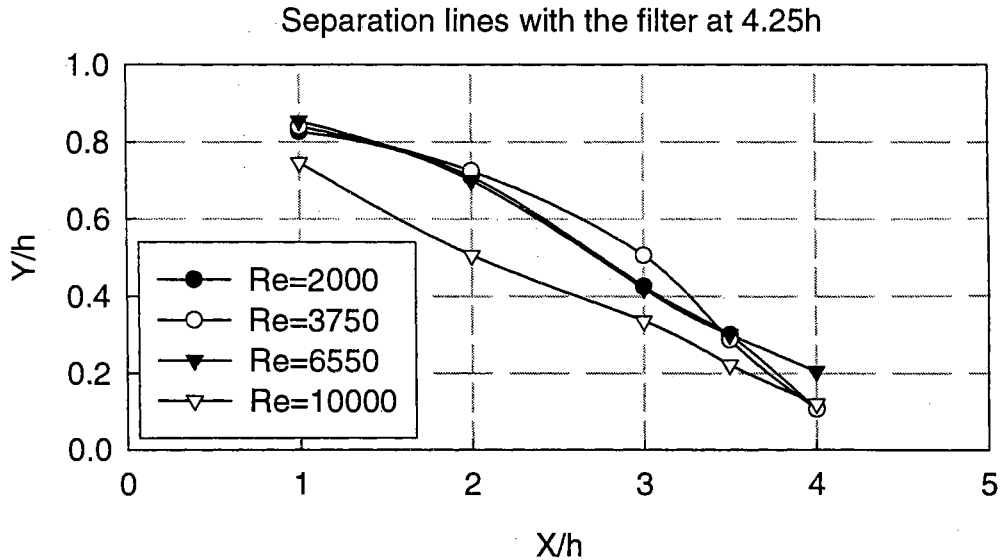


Figure 6.12. The dependence of the separation line on Reynolds number, filter at 4.25h.

For the non-filter flow, the separation lines have similar trends. As the Reynolds number increases, the reversing area decreases and the reattachment length becomes shorter, as shown in Figure 6.13. One exception is found at $Re=3750$ as a result of the existence of the non-step side separation at 6.25h in the non-filter case. One should note that the exception does not occur when the filter is placed at 6.75h and there is no vortex at the non-step side. This further proves that the exception is caused by the existence of the non-step side vortex. The advantage of using the separation line to analyze the effects of the presence of the filter is that it provides an overall flow pattern of the separating flow. However since the velocity measurement is point by point, this is not the real separation line, which is moving all the time. The separation lines presented in this paper are determined by the mean velocity field. Thus we lose the information of the instantaneous separation lines, which is very important for dynamic analysis. However the mean velocity is stable and accurate, which is very important for the comparisons

between the flows with and without the filter. As described in chapter 3, the accuracy of the mean velocity measurement in this study is 1%. Although we cannot apply the 1% accuracy directly to the separation line measurements, it certainly gives us much confidence in the results. Another factor may affect the determination of the separation line is the accuracy of the location control. We are using a traversing system controlled by stepping motors, of which the minimum increment is 12.5 μm . To avoid any errors caused by the backlash of the traversing system, the movement of the probe is always in one direction for each experiment. The step height is 250mm, the typical increment of measuring points in the profiles is $.05h = 12.5 \text{ mm}$. Therefore we can assume that the measuring location control is sufficiently accurate. Additionally since the separation line is at the point of zero mean velocity LDA velocity biasing effects may be considered to be of little importance.

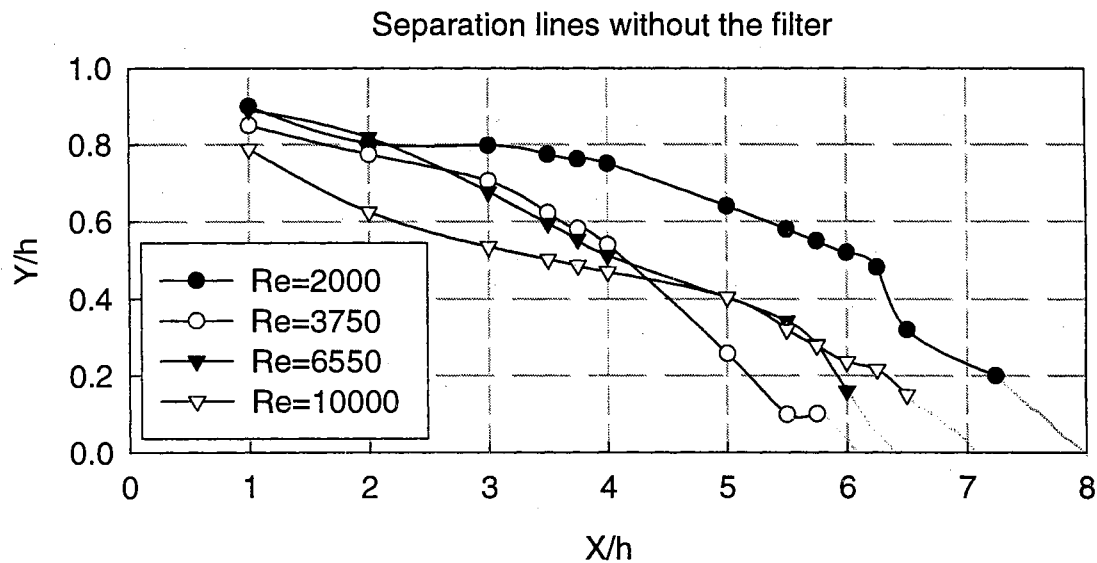


Figure 6.13. The dependence of the separation line on Reynolds number without the filter.

6.3 SUMMARY

Qualitatively the experiments in this chapter gave the same results as do the computational studies presented in chapter V. The filter removes separation flows at the place it occupies and forces the flow to redistribute; the velocity decreases at the side of the channel where velocity is higher and the velocity at the other side increases accordingly.

If the filter is placed downstream of the separation zones at both sides of the channel, it does not have much impact on the flow upstream.

If the filter is placed at a location where the non-filter flow is separated at one side of the channel and not separated at the other side, the separated flow reattaches due to flow acceleration and the flow at the other side separates due to flow deceleration.

When the filter is placed deep into the separation zone of the non-filter flow, the flow reattaches upstream of the filter. The reversing flow area is reduced dramatically and nearly independent of the Reynolds number over Reynolds number range of this study. In most cases, the area of the reversing flow decreases as Reynolds number increases.

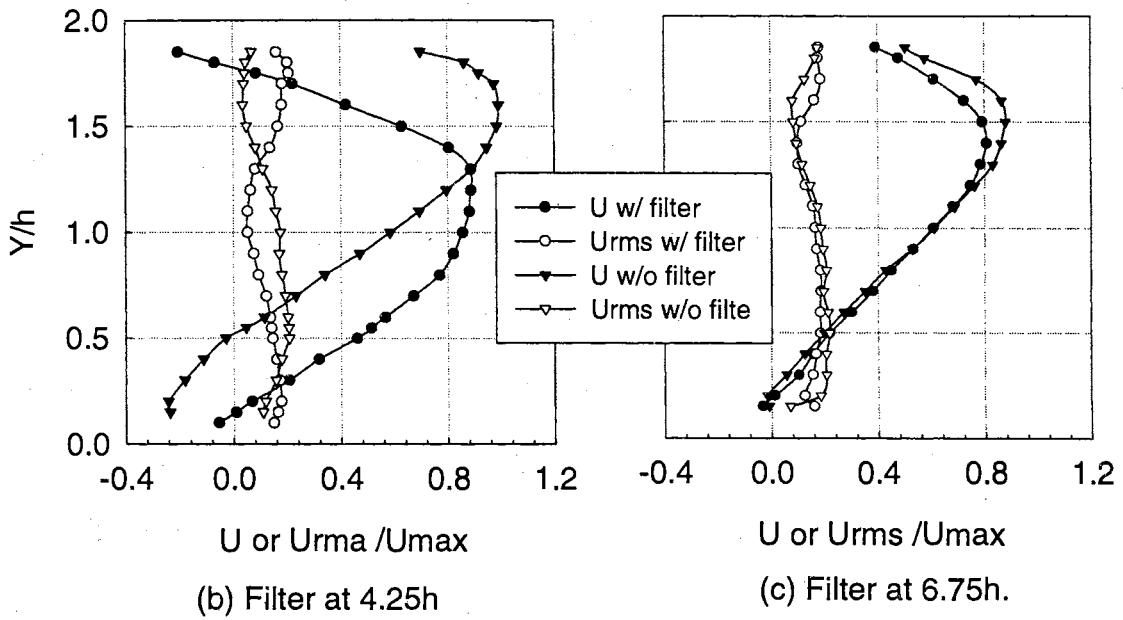
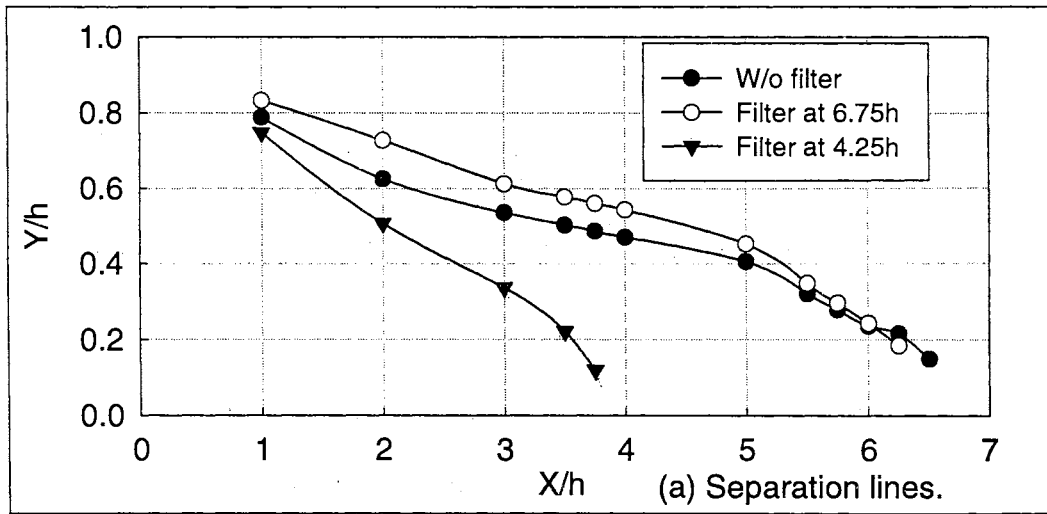


Figure 6.14. Results of $Re=10000$. (a) The separation lines with and without the filter. (b) Velocity profiles .5h upstream of the filter without and with the filter at 4.25h. (c) Velocity profiles .5h upstream of the filter without and with the filter at 6.75h.

CHAPTER VII

LARGE EDDY SIMULATION OF TWO DIMENSIONAL TURBULENT STEP FLOW

Flows in engineering applications are mostly turbulent flows. Simulation of laminar flow can provide some physical understandings about the fluid flow, however simulation of turbulent flows at high Reynolds numbers is the ultimate goal of computer simulation. In Chapters 5 and 6, laminar step flows at very low Reynolds numbers were studied with the air-filter present in the flow domain. One of the problems we encountered with the laminar flow simulation was the numerical stability. At Reynolds number 650 and up, the computed flow did not converge. The flow is three-dimensional at the Reynolds number range of 600-6600, as reported by Armaly et al. (1985). Therefore a two dimensional model is not appropriate for that Reynolds number range. For a flow with Reynolds number higher than 6600, the mean flow is two-dimensional as measured by Armaly et al. As a preliminary study, a two-dimensional Large Eddy Simulation was performed for turbulent flow at Reynolds number 10000. Smagorinsky's eddy viscosity model was used for a two-dimensional mean flow. At the very close wall region, a wall model was used to the first points away from the top and bottom walls. Since the fluctuating velocity of turbulent flows is always three-dimensional, the present model is not a complete simulation. However the present study will give us some

knowledge about large eddy simulation models and a starting point for a better three-dimensional simulation.

The mesh system was the same as for the laminar flow simulation. The flow domain is the same as the experimental setup described in Chapter 6, with the step height the half channel width. The outlet was placed at 30 step heights downstream of the step. 101×101 grid points were used. We already showed that this number of grid points is enough to solve the vortex behind the step for laminar flow. Therefore they are fine enough for LES too, since the vortex behind the step in turbulent flow is of about the same size as in the laminar flow. Silveira et al. (1993) and Karniadakis et al. (1993) used less grid points on the step plane with their LES models. Their three dimensional computations yielded good results.

7.1 INLET FLOW CONDITIONS AND WALL MODELS

As we have already seen in Chapter 6, the velocity at the inlet is dependent upon the Reynolds number. At very low Reynolds number, the flow is laminar and the channel flow at the inlet profile is mostly parabolic. At higher Reynolds number, the profiles can be approximated by the seventh power law or the log law. However since we had the measured inlet velocity profiles, a regression curve was used as the inlet mean velocity profile, as shown in Figure 7.1. As mentioned in section 2.3 of chapter 2, a computer generated random fluctuating velocity is superimposed to the mean velocity. The magnitude is adjustable and uniform cross the inlet. The magnitude of the fluctuating velocity is 1% of the maximum velocity at the inlet in this chapter, which is close to the RMS velocity measured at the entrance of the step flow.

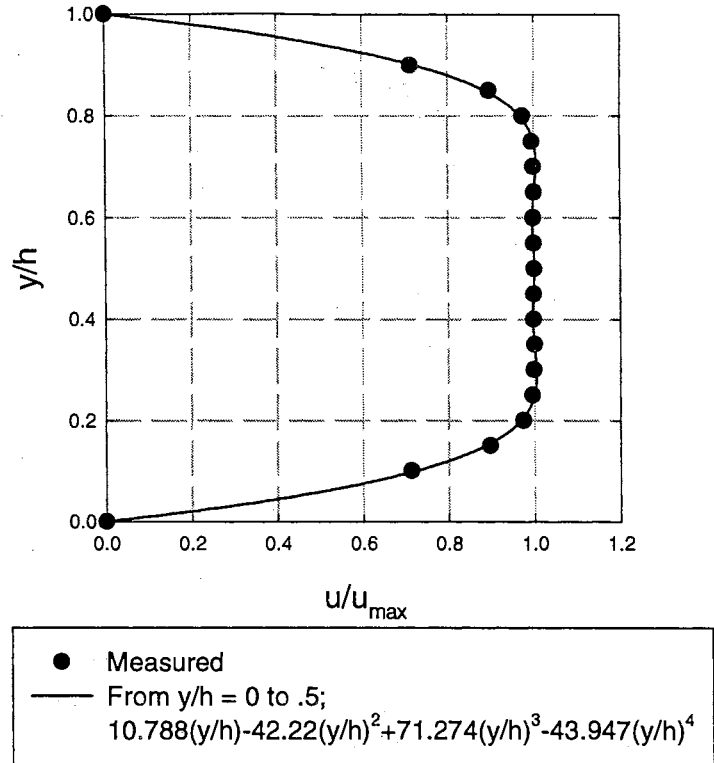


Figure 7.1. The fitted inlet curve for $Re=10000$.

Preliminary computation with Smagorinsky's model (described in section 2.2.2) yielded very large eddy viscosity values near the wall. This is a common problem for the model since it is derived from homogeneous turbulent flows. The velocity gradient is very large near the wall, therefore very fine grid points are needed to solve correctly the velocity fields there. Coarse grids would give very large velocity at the point adjacent to the wall. If the non-slip condition is applied, this may yield excessive velocity gradients and give very large eddy viscosity with Smagorinsky's model. As mentioned in chapter 2, a wall model is used for the first point away from the wall. The non-slip conditions would require a large number of grid points near the wall. Since the emphasis here is on the entire flow domain, not on the flow characteristics at the near wall region, the log law

method will be used as in Silverira et al. (1993). The total shear stress is assumed to be constant and equal to the wall shear across the interval between the wall and the first grid point. A logarithmic velocity profile will be used for the mean velocity as in the case of a turbulent boundary layer. The mean velocity will be calculated when the computation runs in time step by step and the wall shear stress can be obtained by the mean velocity profile, referred to as the log law:

$$U = u^* \left[\frac{1}{\kappa} \log\left(\frac{y_1 u^*}{\nu}\right) + 5 \right], \quad u^* = \sqrt{\tau_w / \rho}, \quad \kappa = .4.$$

where y_1 is the distance between the first point and the wall and τ_w is the wall shear stress. If normalizing the above equation with the step height and the maximum inlet velocity, we will have the following non-dimensional log law formula:

$$\bar{u} = u^* \left[\frac{1}{\kappa} \log(y_1 u^* Re) + 5 \right]$$

In the equation above, only the u^* is unknown. It is numerically solved at each time step corresponding to the mean velocity. After the wall-friction velocity u^* is known, the local turbulent eddy viscosity can be found in the non-dimensional form as:

$$\nu_t = Re \frac{(u^*)^2}{\partial u / \partial y|_{wall}}.$$

The values of eddy viscosity at the wall region were about 2 with the model, reduced from 40 without the model.

7.2 TURBULENT STEP FLOW WITHOUT THE FILTER, RE=10000

The exact location of the reattachment for the non-filter flow is needed for considering where to put the filter to study the filter's effects. The turbulent flow at

$Re=10000$ is first computed without the filter. The experimental results of Armaly et al. (1985) and Eaton & Johnston, (1980, cited from Silveira et al. 1993) indicate that the reattachment location is independent of the Reynolds number in the turbulent regime. The reattachment is at about 8 step heights behind the step. The secondary vortex at the non-step side of the wall does not form in a turbulent flow. The experimental results reported in chapter 6 showed that the reattachment happens at about 6 to 7 step heights. However the present two dimensional simulation predicts that the reattachment happens at 6 step heights, as shown in Figure 7.2. We can see that the separation lines in Figure 7.2 are very similar in shape, although the measured separation is much further downstream. This means that the reversing flow area predicted by the present computation is much smaller than the measured one.

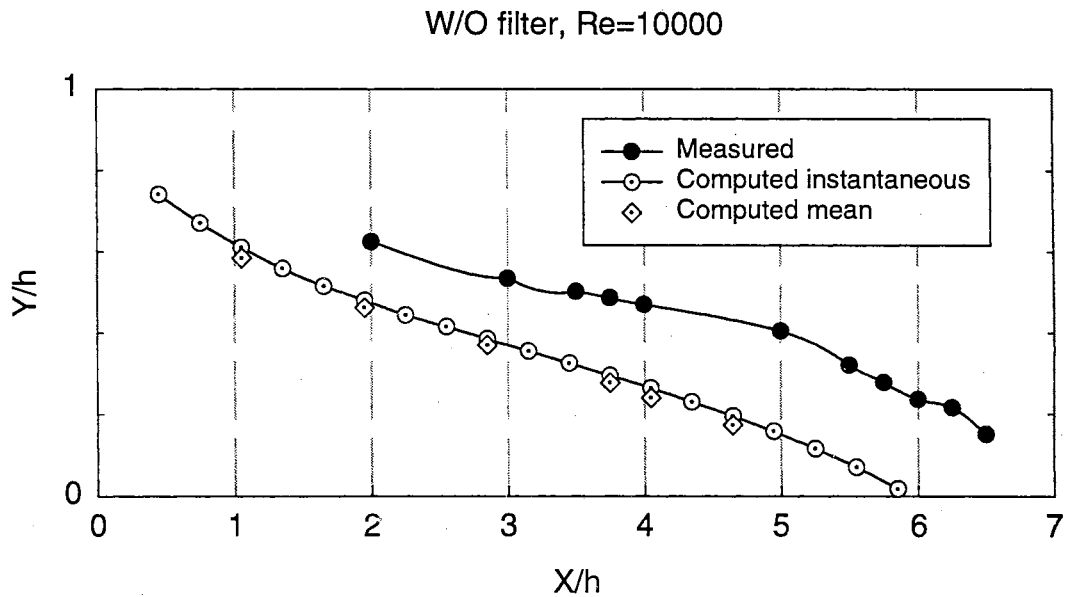


Figure 7.2. Computed separation line compared with the measured, $Re=10000$.

The square points in Figure 7.2 are the zero velocity points from the mean velocity profiles. The line with the round circle is the separation line that was obtained by

the instantaneous velocity field. The difference between the mean and the instantaneous line is very small. The possible explanations for the small reversing flow area could be that the Large Eddy Simulation model is excessively dissipative, especially in the near wall region. Le et al. (1997) stated that the reattachment location moves in the span-wise direction due to its three dimensional structures. The current two dimensional model cannot simulate three dimensional turbulence structures. However from the separation line we can see that the simulation is reasonably close to the measured line. This gives us confidence that a three dimensional simulation with a better LES model should be able to predict well the separation characteristics of the step flow.

The velocity profiles at $x=3.75$ in Figure 7.3 indicate that the LES model is working fairly well at the center region of the channel. It does not work well at the near wall region. A wall model was used to damp Smagorinsky's eddy viscosity at the wall region. It appears not to be working well. Additionally the computed RMS velocity is very small, less than .5% compared with the measured 10% or larger at the same location of the channel. Further study is needed to understand the reason for this poor simulation. Since the predicted separation line is reasonably close to the measured one, we can perform a preliminary study of the separation flow with the filter downstream of the step.

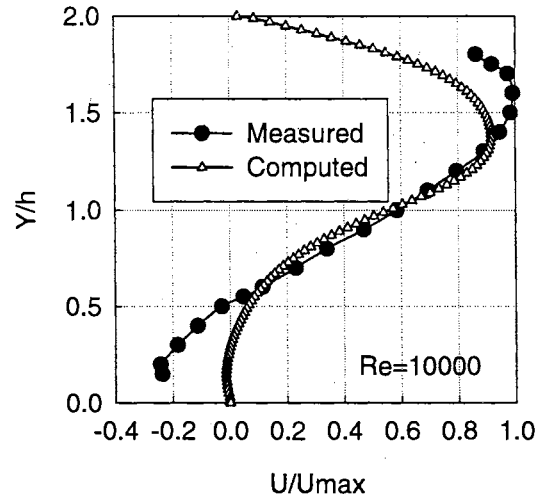


Figure 7.3. Comparison of the computed and the measured velocity profiles.

7.3 TURBULENT STEP FLOW WITH FILTER AT 4.35, RE=10000

In Chapter 6, the filter was placed at two locations, one at 4.25S and another at 6.75S. Those arrangements provided a variety of situations to study. The LES simulation shows the reattachment points at about 6S. In this case the location of 6.75S is no longer necessary. The case of 4.25S will be studied by the LES simulation. For the convenience of the computation, the filter is placed at 4.35S to 7.95S, compared with the experimental setup of 4.25S to 8.00S. The parameters for the Darcy's law are the same as in Chapter 5. The experimental setup is now the step flow shown in Figure 3.1, with the step height of 25 mm. The non-dimensional parameters used in the computation are adjusted accordingly. Figure 7.4 shows the separation line at the Reynolds number of 10000 with the filter at 4.35. The separation line is close to the measured line with the filter at 4.25h. Although the simulation of the non-filter case did not yield very good results compared with the experiments, the computation results with the filter are very encouraging. This

strongly suggests that when the filter is placed close to the step, the interaction between the separated flow behind the step and the filter is dominant.

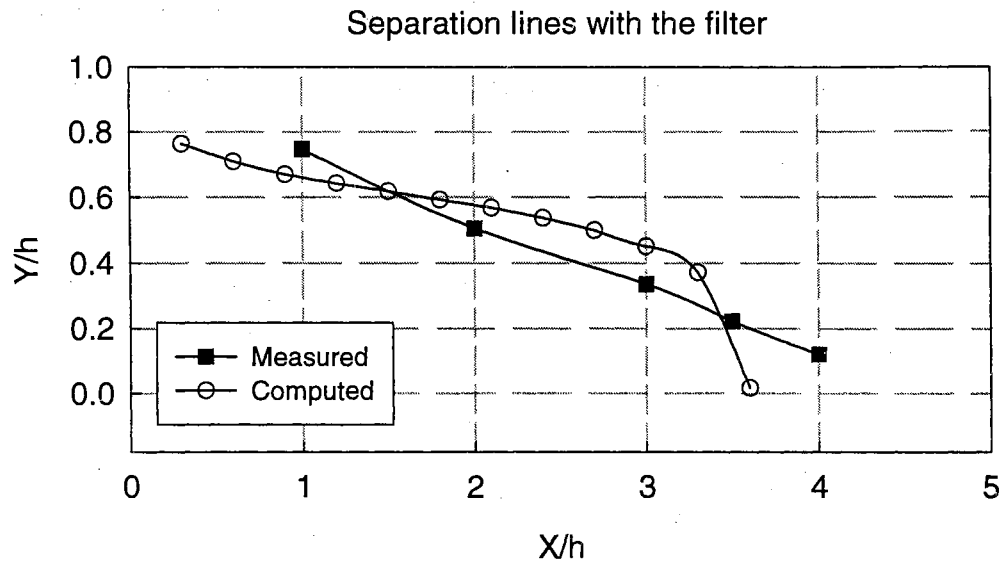


Figure 7.4. The computed separation line compared with the measured at $Re=10000$.

The velocity profiles at $.5h$ upstream of the filter are shown in Figure 7.5. We can see in the velocity at the upper side of the channel, where the flow is not separated, that the introduction of the filter caused the flow to decelerate. The flow at the other side of the channel is accelerated due to the placement of the filter. This reduces the reversing flow at the step side (bottom side). In this case the flow is reattached. The effects of the filter work in the same way as we reported before for laminar flow. However the details are quite different if we compare the computed profile with the measured profile at Figure 7.5. The shape of the computed profile with the filter is similar to the measured. At the wall region, especially at the step side where the non-filter flow is separated, the simulated velocity profile is very different from the measured one. At both sides of the channel the measured flow with the filter is separated, while the simulated flow does not separate at either side. This may again indicate that the LES model used in this paper

does not work very well at the wall region, especially where the flow is separated, for two-dimensional simulation. Although the simulation does not give us results that are close to the measured flow field, it demonstrated that the effects of the filter on the separating flow behind the step are so strong that the features observed in the previous chapters also appear in the computations.

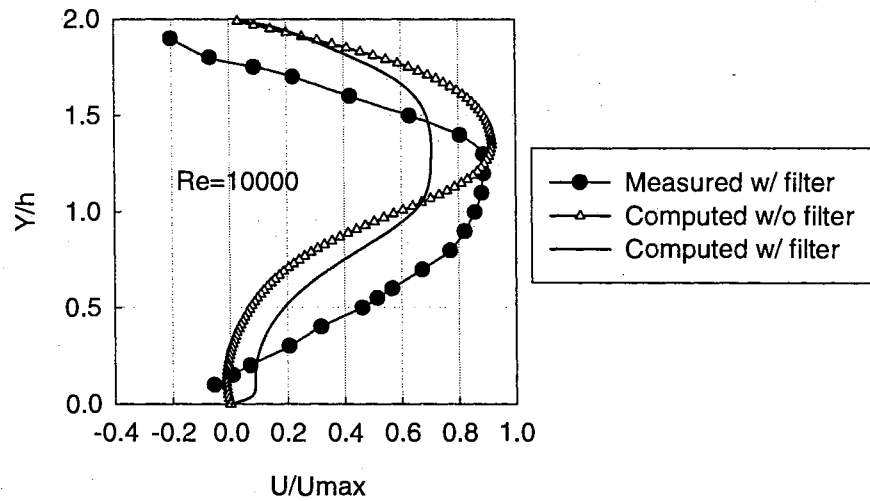


Figure 7.5. Computed and measured velocity profiles .5h upstream of the filter at $Re=10000$.

CHAPTER VIII

CONCLUSIONS

Velocity field measurement by LDA in a real automotive air-filter-housing model demonstrated that the flow is highly non-uniform and fluctuates violently. About 40% of the filter upwind surface is inside separated flow areas, where the mean velocity is very small or negative. The velocity distribution is not good for efficient filtration. This experiment indicates that the interaction between the separated flow and the filter is an important issue for a better understanding of the flow inside the filter housing. However there is little research on the issue up to this author's knowledge. The flow inside the real housing is aerodynamically similar to a backward facing step flow with a filter present. A step flow is a good prototype flow for fundamental research and there are many known results with which to compare. It is simple for us to study extensively experimentally and numerically, while the flow is sophisticated enough to provide flow characteristics similar to practical engineering applications. Therefore a two dimensional backward facing step flow was employed as a model to study the important features of the flow inside the real housing.

8.1 COMPUTATION OF LAMINAR FLOW WITH AND WITHOUT FILTER

The two-dimensional step flow was studied extensively using CFD at low Reynolds numbers (up to 800). The finite difference method and the codes work properly for the flow with and without a filter present. The computation predicts correctly and

accurately the reattachment length and the location of the secondary vortex at low Reynolds numbers compared with existing experimental results of flows without the filter.

When the filter is placed at a location where the non-filter flow is not separated and smooth, the introduction of the filter does not affect the flow properties behind the step very much. Close to the filter, it forces the flow upstream to redistribute; the velocity in the center decreases and the velocity at the two sides increases. This is the case when the filter is placed far downstream of the step.

Separating flow does not appear to penetrate into the filter, no matter how close to the step the filter is placed. If the filter is placed at the location where the non-filter flow is separated at one side and not separated at the other side, the separated flow reattaches and the flow at the other side separates because of the presence of the filter. The reattachment of the separated flow is a result of the acceleration at that side of the channel and the separation at the other side is caused by the deceleration required to maintain the constant flow rate. These events can be observed when the filter is placed at the location of the secondary vortex at the upper non-step side or at the location inside the primary vortex at lower Reynolds numbers.

When the filter is placed very close to the step, where a large part of the cross section is reversing flow at the step side for the non-filter case, the separating flow appears to end upstream of the filter. The secondary vortex is pushed upstream toward the inlet, its downstream edge ends upstream of the filter. It is the same as the separating flow at the step side, the secondary separating flow does not penetrate into the filter or passes the filter.

8.2 LDA MEASUREMENTS OF STEP FLOW WITH AND WITHOUT FILTER

Two-dimensional backward facing step flow was studied by LDA measurements at four Reynolds numbers from 2,000 to 10,000. The flow behind the step was in the transitional and turbulent regimes. A filter was placed at two locations, very close to the step and close to the reattachment positions of the non-filter flows. Velocity distributions were measured by LDA 0.5 step height upstream of the filter.

Qualitatively the experiments gave the same results as obtained by two-dimensional computations at lower Reynolds numbers. The filter removes separation flows at the place it occupies and forces the flow to redistribute; the velocity decreases at the higher average velocity side of the channel and the velocity at the other side increases to keep the flow rate constant in the cross section.

As found in the computations of lower Reynolds number flows, if the filter is placed at a location where there is no reversing flow at both sides of the channel, it does not have much impact on the flow upstream.

If the filter is placed at a location where the non-filter flow is separated at one side of the channel and not separated at the other side, the separated flow reattaches due to acceleration and the flow at the other side separates due to flow deceleration. The same was observed in the computations, although the Reynolds numbers are different.

When the filter is placed deep into the separation zone of the non-filter flow, the flow reattaches upstream of the filter, the reversing flow area is dramatically reduced and nearly independent of the Reynolds number at the current Reynolds number range. In most cases, the reversing area of the flow decreases as Reynolds number increases.

8.3 THE LARGE EDDY SIMULATION AT $Re=10000$

The large eddy simulation at higher Reynolds number ($Re=10000$) does not agree very well with the measurements. However it showed the same effects of the filter on the separating flow downstream of the step. The results showed that the flow field was not well simulated at the near wall region. A better LES model or three-dimensional simulation may be needed improve the results.

The same effects of the filter on the separating flow downstream of the step were observed by the laminar numerical simulation, the LDA measurements and the Large Eddy Simulation.

The velocity the profiles of turbulent flow in Chapter 7 are much flatter in the center than the profiles of laminar flow in Chapter 5. This is an indication that the turbulence simulation is partly working. Without the LES model the computation is unstable at Reynolds number of 800. With the LES model, we were able to compute the flow at $Re=10000$. Those are encouraging results for future studies.

REFERENCES

- 166 Adams, E. W. and Eaton, J. K. (1988) An LDA study of the backward-facing step flow, including the effects of velocity bias. *Journal of Fluids Engineering*, **110**, 275-282.
- Al-Sarkhi, A., S. H. Yao and Chambers F. W., (1997) Flow distribution dependence on housing geometry for tangential inlet automotive air filter housings. *Proceedings of the 10th Annual Technical Conference of the American Filtration and Separations Society*, Minneapolis, MN, April, 1997, Advances in Filtration and Separation Technology, E.R. Baumann and L. Weisert, Editors, Vol. 11, 1997, 210-215.
- Al-Sarkhi, A., S. H. Yao and Chambers, F. W., (1999) Effects of vehicular air filter housing configuration and filter resistance on flow distributions and filtration. Society of Automotive Engineers Technical Paper 1999-01-0007.
- 166 Armaly, B. F., Durst, F., Pereira, J. C. F. and Schönung, B. (1983) Experimental and theoretical investigation of backward facing step flow. *Journal Fluid Mech.*, **127**, 473-496.
- 166 Badran, O. O. and Bruun, H. H. (1999) Comparison of flying-hot-wire and stationary-hot-wire measurements of flow over a backward-facing step. *Journal of Fluids Engineering*, **121**, 441-445
- X Cabot, W. and Moin, P. (1993) Large eddy simulations of scalar transport with dynamic subgrid scale model. In *Large Eddy Simulation of Complex Engineering and Geophysical Flows* (ed. B. Galperin & S. A. Orszag), 141-158, Cambridge University Press.
- X Chapman, D. R. and Kuhn, G. D. (1986) The limiting behavior of turbulence near a wall. *Journal of Fluid Mech.*, **170**, 265-292.
- 166 Chen, F. and Chen, C. F. (1992) Convection in superposed fluid and porous layers. *Journal of Fluid Mech.*, **234**, 97-119.
- X Chwang, A. T. and Chan A. T. (1998) Interaction between porous media and wave motion. *Ann. Rev. Fluid Mech.*, **20**, 53-84.
- X Deardorff, J. W. 1970, A numerical study of three-dimensional turbulent channel flow at large Reynolds numbers. *Journal of Fluid Mech.*, **41**, 453-480.

- ✓ Driver, D. and Seegmiller, H. L., (1985) Features of a reattaching turbulent shear layer in divergent channel flow. *AIAA Journal*, **23**, No. 2, 163-171.
- ✗ Duran, R., (1995) Improvement of flow uniformity and modeling of filtration efficiencies for automotive air filter test housings, MS Thesis, School of Mechanical and Aerospace Engineering, Oklahoma State University, Stillwater, Oklahoma.
- ✗ Durbin, P. A. (1995) Separation computations with κ - ϵ - ν model. *AIAA Journal*, **33**, No. 4, 633-635.
- ✗ Durst, F., Melling, A. and Whitelaw, J. H. (1976). Principles and practice of laser-Doppler anemometry. New York, NY, Academic Press.
- ✗ Ferziger, J. H. (1993). Subgrid-scale modeling. In *Large Eddy Simulation of Complex Engineering and Geophysical Flows*. (ed. B. Galperin & S. A. Orszag), 37-54, Cambridge University Press.
- ✗ Gurumoorthy, V. (1990) Computational fluid dynamic modeling of air induction system. MS Thesis, Dept. of Mechanical Engineering, University of Rhode Island.
- ✓ Jovic, S. and Driver, D. M. (1995) Reynolds number effects on the skin friction in the separated flows behind a backward facing step flow. *Experiments in Fluids*, **18**, 464-467.
- ✓ Kaiktsis, L., Karniadakis, G. E. and Orszag, S. A. (1991) Onset of three-dimensionality, equilibrium and early transition in flow over a backward-facing step. *Journal of Fluid Mech.*, **231**, 501-528.
- ✗ Karniadakis, G. E. and Orszag, S. A. and Yakhot, V. (1993) Renormalization group theory simulation of transitional and turbulent flow over a backward facing step. In *Large Eddy Simulation of Complex Engineering and Geophysical Flows*. (ed. B. Galperin & S. A. Orszag), 159-177, Cambridge University Press.
- ✓ Kim, J. and Moin, P. (1985) Application of a fractional-step method to incompressible Navier-Stokes equations. *Journal of Comput. Phys.*, **59**, 308-323.
- ✗ Kim, J. and Moin, P. (1986) The structure of the vorticity field in turbulent channel flow, part 2: study of ensemble averaged fields. *Journal of Fluid Mech.*, **162**, 339-363.
- ✗ Ku, H. C., Hirsh, R. S. Taylor, T. D. and Rosenberg, A. P. (1989) A pseudospectral matrix element method for solution of three-dimensional incompressible flows and its parallel implementation. *Journal of Comput. Phys.*, **83**, 260-291.
- ✓ Le, H., Moin, P. and Kim, J. (1997) Direct numerical simulation of turbulent flow over a backward facing step flow. *Journal of Fluid Mech.*, **330**, 349-374.

- X Lesieur, M. and Métais, O. (1996) New trends in large-eddy simulations of turbulence. *Ann. Rev. Fluid Mech.*, **28**, 45-82.
- X Liu, G. J. (1995) Velocity measurement and CFD predictions of flow redistribution through air filters. MS Thesis, School of Mechanical and Aerospace Engineering, Oklahoma State University, Stillwater, OK.
- X Mason, P. J. & Callen N. S. (1986) On the magnitude of the subgrid-scale eddy coefficient in Large-Eddy Simulation of turbulent channel flow. *Journal of Fluid Mech.*, **162**, 439-462.
- Moin, P. & Kim, J. (1982), Numerical investigation of turbulent channel flow, *Journal of Fluid Mech.*, **118**, 341-377.
- Morel, T. (1977), Design of two dimensional wind tunnel contractions. *Journal of Fluids Engineering*, **99**, No. 6, 372-377.
- Newman R.A. (1995), Uniformity of air flow in automotive test housing and its effects on the efficiency of fibrous filters, MS Thesis, School of Mechanical and Aerospace Engineering, Oklahoma State University, Stillwater, OK.
- Newman, R. A., Duran, R. and Chambers, F. W. Air filter housing velocity profile effects on filter efficiency. Society of Automotive Engineers Technical Paper 970554.
- Piomelli, U. (1993a) Applications of large eddy simulations in engineering: an overview. In *Large Eddy Simulation of Complex Engineering and Geophysical Flows*. (ed. B. Galperin & S. A. Orszag), 119-137, Cambridge University Press.
- Piomelli U. (1993b) High Reynolds number calculations using the dynamic subgrid-scale stress model. *Phys. Fluids*, **A5(6)**, 1484-1490
- Piomelli U., Ferziger J. H., Moin P. and Kim J., 1989, New approximate boundary conditions for Large Eddy Simulations of wall-bounded flows, *Phys. Fluids*, **A1**, 1061-1068
- Rodi, W. and Scheuer, D. (1986) Scrutinizing the κ - ϵ model under adverse pressure gradient conditions. *Journal of Fluids Engineering*, **108**, 174-180
- Rogallo, R. S. and Moin, P. (1984) Numerical simulation of turbulent flows. *Ann. Rev. Fluid Mech.*, **16**, 99-137
- Scarano, F. and Riethmuller, M. L. (1999) Iterative multigrid approach in PIV image processing with discrete window offset. *Experiments in Fluids*, **26**, 513-523
- Schlichting, H. (1979) *Boundary layer theory*. 7th ed. , McGraw-Hill, New York.

- ✓ Schumann, U. (1975) Subgrid scale model for finite difference simulations of turbulent flows in plane channel and annuli. *Journal of Comput. Phys.*, **18**, 376-404
- ✓ Silveira Neto, A., Grand, D., Métais, O. and Lesieur, M. (1993) A numerical investigation of coherent vortices in turbulence behind a backward-facing step. *Journal of Fluid Mech.*, **256**, 1-25
- ✓ Tebbutt, C. B. (1995) CFD model of flow through air filter pleats, MS Thesis, School of Mechanical and Aerospace Engineering, Oklahoma State University, Stillwater, OK.
- ✓ Yoo, J. Y. and Baik, S. J. (1992) Redeveloping turbulent boundary layer in the backward-facing step flow. *Journal of Fluids Engineering*, **114**, 522-529

RECOMMENDED PAPERS

- Abbott, D. E. and Kline, S. J. (1961) Theoretical and experimental investigation of flow over single and double backward-facing steps. Report MD-5, Thermosciences Div., Mech. Engrg. Dept., Stanford.
- Arnal, M. and Friedrich, R. (1993) Large eddy simulations of a turbulent flow with separation. In *Turbulence Shear Flows 8* (ed. F. Durst, R. Friedrich, B. E. Launder et al) 169, Springer, New York.
- Bardina, J. , Ferziger, J. H. and Reynolds, W. C. (1980) Improved subgrid scale models for large eddy simulation. AIAA paper 80-1357.
- Bradshaw, P. and Wong, F. Y. F. (1972) The reattachment and relaxation of turbulent shear layers. *Journal of Fluid Mech.*, **152**, 113-135.
- Chapman, D. R. (1979) Computational aerodynamics development and outlook. *AIAA Journal*, **17**, 1293-1313.
- Clark, R. A., Ferziger, J. H. and Reynolds, W. C. (1979) Evaluation of subgrid-scale models using an accurate simulated turbulent flow. *Journal of Fluid Mech.*, **91**, 1-16.
- Eaton, J. K. and Johnston, J. P. (1980) Turbulent flow re-attachment: an experimental study of the flow and structure behind a backward-facing step. Stanford University, Rep. MD-39.
- Friedrich, R. and Nieuwstadt, F. (1994). LES of pipe flows. *ERCRAFTAC Bull.*, **22**, 19-25.
- Germano, M., Piomelli U., Moin P. & Cabot W. H. (1991), A dynamic subgrid-scale eddy viscosity model. *Phys. Fluids.*, **A3**, 1760-1765.
- Ghosal, S., Lund, T. S., Moin, P., and Akselvoll, K., (1995) A dynamic localization model for simulation of turbulent flows. *Journal of Fluid Mech.*, **286**, 229-255.
- Jovic, S. and Driver, D. (1994) Backward-facing step measurement at low Reynolds numbers. NASA TM, 108807.
- Kaltenbach, H. J., Schumann, U., and Gerz, T. (1994) Large-eddy simulations of turbulent diffusion in stably-stratified flow. *Journal of Fluid Mech.*, **280**, 1-40.

- Kim, J., Kline, S. J. and Johnson, J. P. (1978) Investigation of separation and reattachment of a turbulent shear layer flow over a backward-facing step. Report MD-37, Thermosciences Div., Dept of Mechanical Engineering., Stanford University, Stanford, CA.
- Ko, S. (1993) Computation of turbulent flows over backward and forward facing steps using near wall Reynolds stress model. Center for Turbulence Research, Stanford University, Annual Research Briefs, 75-90.
- Leonard, A. (1974) Energy cascade in large-eddy simulation of turbulent fluid flows. *Adv. Geophys*, **18A**, 237-248.
- Lilly, D. K. (1992) A proposed modification of the Germano subgrid-scale closure method. *Phys. Fluids*, **A4**, 633-635.
- McMillan O. J., Ferziger, J. H. & Reynolds W. C. (1980) Test of new subgrid scale models in strained turbulence. *AIAA paper* **80-1339**.
- Perot, J. B. (1993) An analysis of the fractional step method. *Journal of Comput. Phys.*, **108**, 51-58.
- Piomelli U., Ferziger J. H. and Moin P. (1987) Models for large eddy simulations of turbulent channel flows including transpiration. Report TF-31. Dept. of Mechanical Engineering, Stanford University, Stanford, CA.
- Piomelli U., Moin P. & Ferziger J. H. (1988) Model consistence in large eddy simulation of turbulent channel flows. *Phys. Fluids*, **31**, 1884-1891.
- Piomelli, U., Cabot, W. H. Moin, P. and Lee, S. (1991) Subgrid-scale backscatter in turbulent and transitional flow. *Phys. Fluids*, **A3**, 1766-1771.
- Smagorinsky, J. (1963) General circulation experiments with the primitive equations, I. the basic experiment. *Monthly Weather Rev.*, **91**, 99-164.
- Sreedhar M., Ragab, S. (1994) Large-eddy simulation of longitudinal stationary vortices. *Phys. Fluids*, **6(7)**, 2501-2514.
- Stummel, F. and Hainer, K., Introduction to Numerical Analysis, (1980) (Ed: N. Everitt and translated by E. R. Dawson), Scottish Academic Press, Edinburgh.

APPENDICES

A. LES FILTER PROCESS:

For an arbitrary function f , the filter operation can be expressed as:

$$f = \bar{f} + f'$$

$$\bar{f}(x_1, x_2, x_3) = \int_D \prod_{i=1}^3 G_i(x_i, x'_i) f(x'_1, x'_2, x'_3) dx'_1 dx'_2 dx'_3$$

where G_i is the filter function in the i -direction and the integral is extended over the whole flow field. This is a weighted averaging process. Because turbulence length scale varies considerably in the direction normal to the walls, x_1 , one should use a filter with a variable width. Moin and Kim (1982) used a sectionally continuous 'top hat' filter function in their 3-D channel flow LES computation. In Moin and Kim, $x_{i,j}$ is the location of the j -th computational grid point in the i -direction normal to a wall of the channel; the filter function G_i is defined for the control volumes surrounding the point as follows:

$$G_i(x_i, x'_i) = \begin{cases} (\Delta^+(x_i) + \Delta^-(x_i))^{-1} & \text{for } x_i - \Delta^-(x_i) < x'_i < x_i + \Delta^+(x_i) \\ 0 & \text{for } x'_i < x_i - \Delta^-(x_i) \quad x'_i > x_i + \Delta^+(x_i) \end{cases}$$

$$\text{where } \left. \begin{aligned} \Delta^+(x_i) &= \frac{1}{2}(x_{i,j+1} - x_{i,j}) = \Delta_{i,j}^+ \\ \Delta^-(x_i) &= \frac{1}{2}(x_{i,j} - x_{i,j-1}) = \Delta_{i,j}^- \end{aligned} \right\} \text{for } \frac{1}{2}(x_{i,j} + x_{i,j-1}) < x_i < \frac{1}{2}(x_{i,j+1} + x_{i,j})$$

The functions Δ^+ and Δ^- are sectionally constant functions of x_i , therefore in the open area surrounding each computational grid point

$$x_i - \Delta^- < x_i < x_i + \Delta^+, \quad d\Delta^+ / dx_i = d\Delta^- / dx_i = 0$$

This property of Δ^+ and Δ^- is very important because it provides the commutativity of the filter function and partial-differential operators in this computational area, particularly at the grid points. That is:

$$\frac{\overline{\partial f}}{\partial x_i} = \frac{\partial \bar{f}}{\partial x_i}$$

When a uniform mesh is used for the direction, it is simply:

$$G_i(x_i, x'_i) = \begin{cases} 1/h_i & \text{for } x_i - h_i/2 < x'_i < x_i + h_i/2 \\ 0 & \text{for } x'_i < x_i - h_i/2 \quad x'_i > x_i + h_i/2 \end{cases}$$

By Simpson numerical integration:

$$f(\bar{x}_{k,i}) = \frac{1}{6(\Delta_{k,i}^- + \Delta_{k,i}^+)} [\Delta_{k,i}^- f(x_{k,i} - \Delta_{k,i}^-) + 5(\Delta_{k,i}^- + \Delta_{k,i}^+) f(x_{k,i}) + \Delta_{k,i}^+ f(x_{k,i} + \Delta_{k,i}^+)]$$

For 2-D

$$\bar{f}(x_{1,i}, x_{2,j}) = f(\bar{x}_{1,i}, \bar{x}_{2,j}) = \frac{1}{6(\Delta_{1,i}^- + \Delta_{1,i}^+)} [\Delta_{1,i}^- f(x_{1,i} - \Delta_{1,i}^-, \bar{x}_{2,j}) + 5(\Delta_{1,i}^- + \Delta_{1,i}^+) f(x_{1,i}, \bar{x}_{2,j}) + \Delta_{1,i}^+ f(x_{1,i} + \Delta_{1,i}^+, \bar{x}_{2,j})]$$

From 2-D to 3-D, the same procedure applies.

B. NON-UNIFORM COMPUTATIONAL GRID:

Three factors influence the choice of the computational grid. First, the mesh size should be small enough to resolve the important scales in the flow. Secondly the computational domain should be large enough that the applied boundary conditions do not influence the statistics of the solution in an undesirable way. Thirdly, the availability of computer resources restricts the size of calculation that can be done.

At near wall region, the velocity gradient in the direction normal to the wall is very large and the dominant flow structures are small in space. Very fine grids are needed in the wall region to simulate the flow structures there. However in the region far away from the wall, flow is smooth and the turbulent structures are mostly very large. Relatively coarse grids can be used in the core region. If non-uniform grids are used, more grids in the wall region and less grids in the core region, it can save significantly computer memories and CPU time.

In the direction normal to the wall usually non-uniform grids are employed. Moin and Kim (1982) used the following grid system in the direction normal to the wall:

$$y_j = \frac{1}{2} \tanh(\zeta_j \alpha \tanh(\alpha))$$

$$\zeta_j = -1 + 2(j-1)/(N_2 - 1) \quad j = 1, 2, 3, \dots, N_2$$

N_2 is the total number of grid points in that direction. α is the adjustable parameter of the transformation ($0 < \alpha < 1$); a large value of α distributes more points near the walls.

Moin and Kim stated there were sufficient points to resolve the viscous sublayer ($y^+ < 5$) if $N_2 = 63$ and $\alpha = .98346$ were employed, a total 516,096 grid points were used for a channel flow of $Re = 13,800$.

In the present computation, uniform grids are used in the two directions. The non-uniform algorithm may be useful for future improvements.

C. FINITE DIFFERENCE SCHEME

To discretize the equations (2.9) by the procedure mentioned in section 2.4 yields:

$$\begin{aligned} \frac{\hat{u}_i^{n+1} - u_i^n}{\Delta t} = F_i^n + \hat{F}_i^{n+1} = & \frac{1}{2}(3H_i^n - H_i^{n-1}) + \frac{1}{2\text{Re}} \left\{ \frac{\delta}{\partial x_1} \left[\left(1 + \frac{v_T}{\nu}\right) \frac{\delta}{\partial x_1} \right] \right. \\ & \left. + \frac{\delta}{\partial x_2} \left[\left(1 + \frac{v_T}{\nu}\right) \frac{\delta}{\partial x_2} \right] + \frac{\delta}{\partial x_3} \left[\left(1 + \frac{v_T}{\nu}\right) \frac{\delta}{\partial x_3} \right] \right\} (\hat{u}_i^{n+1} + u_i^n) \end{aligned} \quad (\text{C.1})$$

$$H_i^n = -\frac{\delta}{\partial x_j} u_i u_j \text{ is the convective terms}$$

$$\frac{u_i^{n+1} - \hat{u}_i^{n+1}}{\Delta t} = -G(\phi^{n+1}) \quad (\text{C.2})$$

$$D_i(u_i^{n+1}) = 0 \quad (\text{C.3})$$

ϕ is a scalar to be determined associated with pressure, $\delta/\delta x$ represents discrete finite difference operators, and G and D represent discrete gradient and divergence respectively. The second-order-explicit Adams-Bashforth scheme is used for convective terms, and the second-order-implicit Crank-Nicholson for the viscous and the SGS terms. All the spatial derivatives are approximated with second-order central differences on a staggered grid as shown in Appendix G. The overall accuracy of this splitting method is second order, (Moin and Kim 1982). The pressure can be found as follows:

$$\begin{aligned} u_i^{n+1} &= u_i^n + \frac{\partial u_i^n}{\partial t} \Delta t + O(\Delta t^2), \quad \frac{\partial u_i^n}{\partial t} = F_i^n - \nabla P \quad \text{and} \quad \hat{u}_i^{n+1} = u_i^n + (F_i^n + \hat{F}_i^{n+1}) \Delta t \\ u_i^{n+1} &= u_i^n + (F_i^n - \nabla P) \Delta t = \hat{u}_i^{n+1} - \hat{F}_i^{n+1} \Delta t - \nabla P \Delta t \\ \nabla^2 \phi^{n+1} &= (\nabla \cdot \hat{u}_i^{n+1}) / \Delta t \\ P &= \phi + \frac{\Delta t}{2\text{Re}} \left[\nabla \cdot \left(1 + \frac{v_T}{\nu}\right) \nabla \right] \phi \end{aligned}$$

So we know that ϕ is a second order approximation of pressure and can be treated as pressure.

Moin and Kim (1985) used a special procedure to save considerably the computation needed to solve the equation. (C.1) can be rewritten as

$$(1 - A_1 - A_2 - A_3)(\hat{u}_i^{n+1} - u_i^n) = \frac{\Delta t}{2}(3H_i^n - H_i^{n-1}) + 2(A_1 + A_2 + A_3)u_i^n \quad (\text{C.4})$$

$$A_j = \frac{\Delta t}{2\text{Re}} \left[\frac{\delta}{\partial x_j} \left(1 + \frac{v_T}{v} \right) \frac{\delta}{\partial x_j} \right] \quad j = 1, 2, 3$$

Then (C.4) can be approximated as follows:

$$(1 - A_1)(1 - A_2)(1 - A_3)(\hat{u}_i^{n+1} - u_i^n) = \frac{\Delta t}{2}(3H_i^n - H_i^{n-1}) + 2(A_1 + A_2 + A_3)u_i^n \quad (\text{C.5})$$

$$(\text{C.5}) - (\text{C.4}) = (A_1A_2 + A_2A_3 + A_3A_1 - A_1A_2A_3)(\hat{u}_i^{n+1} - u_i^n) = O(\Delta t^3)$$

Equation (C.5) is an $O(\Delta t^3)$ approximation to (C.4). It requires inversion of tridiagonal matrices rather than inversion of a long sparse matrix, as in the case of equation (C.4).

This results in significant reduction in computing cost and memory.

For cells not adjacent to the boundaries, the ϕ equation takes the form of the

Poisson discrete equation:

$$\left(\frac{\delta^2}{\partial x_1^2} + \frac{\delta^2}{\partial x_2^2} + \frac{\delta^2}{\partial x_3^2} \right) \phi^{n+1}(i, j, k) = \frac{1}{\Delta t} D(\hat{u}^{n+1}) \equiv Q(i, j, k)$$

$$i = 2, 3, \dots, N_1 - 1, \quad j = 2, 3, \dots, N_2 - 1, \quad k = 2, 3, \dots, N_3 - 1$$

For cells adjacent to the boundaries, for example $j=1$:

$$\left(\frac{\delta^2}{\partial x_1^2} + \frac{\delta^2}{\partial x_3^2} \right) \phi^{n+1}(i, 1, k) + \frac{1}{x_2(\frac{3}{2}) - x_2(\frac{1}{2})} \frac{\phi^{n+1}(i, 2, k) - \phi^{n+1}(i, 1, k)}{x_2(2) - x_2(1)}$$

$$= \frac{1}{\Delta t} \left[D(\hat{u}^{n+1}) - \frac{u_2^{n+1}(i, \frac{1}{2}, k) - \hat{u}_2^{n+1}(i, \frac{1}{2}, k)}{x_2(\frac{3}{2}) - x_2(\frac{1}{2})} \right] \equiv Q(i, j, k)$$

$$i = 2, 3, \dots, N_1 - 1, \quad k = 2, 3, \dots, N_3 - 1$$

where the gradient of ϕ is approximated by $G(\phi) = -(u^{n+1} - \hat{u}^{n+1})\Delta t$.

Boundary conditions for the intermediate velocity field in time splitting method are generally a source of ambiguity. At each complete time step, only the boundary conditions for the velocity field are given. Those for the intermediate velocity field are unknown. If the boundary conditions for the intermediate velocity field are not chosen to

be consistent with the governing equations, significant numerical errors may occur to the solution as noted by Kim and Moin (1985). They derived the appropriate boundary conditions for the intermediate velocity field as follows:

$$\hat{u}_i^{n+1} = u_i^{n+1} + \Delta t \frac{\partial \phi^n}{\partial x_i} + O(\Delta t)^2$$

which is a second order approximation in time and is used in this paper.

D. OVER-RELAXATION ITERATION TO SOLVE POISSON EQUATION

In the two-step time split method, pressure is solved by the Poisson equation. For 2-D staggered grid:

$$\begin{aligned} T_p^{n+1} &= T_p^n + \frac{1}{4} w \bullet R_p \\ R_p &= T_N + T_S + T_E + T_W - 4T_p \end{aligned}$$

where w is the relaxation coefficient, over-relaxation means that $1 < w < 2$.

$$w_{opt} = 2 - \pi \left[\frac{2}{p^2} + \frac{2}{q^2} \right]^{1/2}$$

p and q are the number of mesh intervals in two directions. By the procedure, the formula for three dimensions also can be obtained.

E. DIFFERENCE EQUATIONS OF 2-D LES FOR STEP FLOWS

PART I: Solve \hat{u}_i^{n+1} , $i = 1, 2$

As noted in Chapter 2, the intermediate velocity can be solved without knowing pressure. The pressure will be solved in part 2 when the intermediate velocity is known.

E.1. The Basic Equations:

In all the notations later, n denotes the current time when all the variables are known; $n+1$ denotes the next time step and $n-1$ the previous time step. To make the non-linear Navier-Stokes equations linear, the inertial terms are approximated by their values at the current time and the previous time steps. This procedure practically disassociates the two velocity components u and v , which enable us to solve the two components separately at one time step. The subscripts here follow the Einstein rules.

$$(1 - A_1)(1 - A_2)(\hat{u}_i^{n+1} - u_i^n) = \frac{\Delta t}{2}(3H_i^n - H_i^{n-1}) + 2(A_1 + A_2)u_i^n \quad (\text{E.1})$$

$$A_j = \frac{\Delta t}{2\text{Re}} \frac{\partial}{\partial x_j} \left(1 + \frac{v_T}{\nu}\right) \frac{\partial}{\partial x_j} \quad H_i^n = -\frac{\partial}{\partial x_j} u_i u_j$$

E.2. Detonations:

For the convenience of typing and implementing into program code, the following detonations will be used. Subscript 1 stands for the direction of u and 2 stands for direction of v . From now on i denotes the grid point in horizontal x direction and j denotes the points in vertical y direction.

$$\begin{aligned} ut1 = \hat{u}_1^{n+1}, \quad ut0 = u_1^n, \quad ut0m = u_1^{n-1}, \quad ut2 = u_1^{n+1}, \quad YU = yu_1 \\ vt1 = \hat{u}_2^{n+1}, \quad vt0 = u_2^n, \quad vt0m = u_2^{n-1}, \quad vt2 = u_2^{n+1}, \quad YV = yu_2, \quad vst = 1 + \frac{v_T}{\nu} \end{aligned}$$

E.3. Staggered Grid

The two dimensional staggered mesh is shown in Fig. E.1. The momentum equations are evaluated at velocity nodes and the continuity equation is enforced for each cell. One important advantage of using staggered mesh is that pressure boundary conditions are not required.

Velocity is not evaluated at the center of the staggered grid cell. However its values there can be computed by linear interpolation, which is still second-order accurate as the difference scheme requires (Deardorff, 1970). The subgrid eddy viscosity is evaluated at the center of the cell, as the pressure terms.

$$\begin{aligned}u_{i,j+\frac{1}{2}} &= \frac{u_{i,j} + u_{i,j+1}}{2}, & u_{i,j-\frac{1}{2}} &= \frac{u_{i,j} + u_{i,j-1}}{2} \\v_{i+\frac{1}{2},j} &= \frac{v_{i,j} + v_{i+1,j}}{2}, & v_{i-\frac{1}{2},j} &= \frac{v_{i,j} + v_{i-1,j}}{2}\end{aligned}$$

E.4. Difference Equations at Right Side

Since the two velocity-components u and v are not evaluated at the same grid locations, the forms of difference are not exactly the same for u and v , although their basic equations are the same. Some terms are computed by averaging as in section E.3. The relations of the grid points and the evaluations at the nodes are shown in Figure E.1. To ensure second-order accuracy, sometime four points are used for first order derivatives.

$$\begin{aligned}
HU0 &= H_1^n = -\frac{\partial}{x}(ut0)^2 - \frac{\partial}{y}(ut0 * vt0) \\
&= \frac{(ut0_{i-1,j} + ut0_{i,j})^2 - (ut0_{i,j} + ut0_{i+1,j})^2}{4\Delta x} + \frac{(vt0_{i-1,j} + vt0_{i,j}) * (ut0_{i,j-1} + ut0_{i,j})}{4\Delta y} \\
&\quad - \frac{(vt0_{i-1,j+1} + vt0_{i,j+1}) * (ut0_{i,j} + ut0_{i,j+1})}{4\Delta y}
\end{aligned}$$

$$\begin{aligned}
HU0M &= H_1^{n-1} = -\frac{\partial}{x}(ut0m)^2 - \frac{\partial}{y}(ut0m * vt0m) \\
&= \frac{(ut0m_{i-1,j} + ut0m_{i,j})^2 - (ut0m_{i,j} + ut0m_{i+1,j})^2}{4\Delta x} + \frac{(vt0m_{i-1,j} + vt0m_{i,j}) * (ut0m_{i,j-1} + ut0m_{i,j})}{4\Delta y} \\
&\quad - \frac{(vt0m_{i-1,j+1} + vt0m_{i,j+1}) * (ut0m_{i,j} + ut0m_{i,j+1})}{4\Delta y}
\end{aligned}$$

$$\begin{aligned}
HVO &= H_2^n = -\frac{\partial}{x}(ut0 * vt0) - \frac{\partial}{y}(vt0)^2 \\
&= \frac{(ut0_{i,j-1} + ut0_{i,j}) * (vt0_{i-1,j} + vt0_{i,j}) - (ut0_{i+1,j-1} + ut0_{i+1,j})(vt0_{i,j} + vt0_{i+1,j})}{4\Delta x} \\
&\quad + \frac{(vt0_{i,j-1} + vt0_{i,j})^2 - (vt0_{i,j} + vt0_{i,j+1})^2}{4\Delta y}
\end{aligned}$$

$$HVO M = H_2^{n-1} = -\frac{\partial}{x}(ut0m * vt0m) - \frac{\partial}{y}(vt0m)^2$$

$$\begin{aligned}
A1U &= A_1(u_1^n) = \frac{\Delta t}{2 \text{Re}} \frac{\partial}{x} \left(\left(1 + \frac{v_T}{v}\right) \frac{\partial}{x} \right) u_1^n = \frac{\Delta t}{2 \text{Re}} \frac{\partial}{x} \left(vst \frac{\partial}{x} \right) u_1^n = \frac{\Delta t}{2 \text{Re}} \left(\frac{\partial vst}{\partial x} \frac{\partial ut0}{\partial x} + vst \frac{\partial^2 ut0}{\partial x^2} \right) \\
&= \frac{\Delta t}{2 \text{Re}} \left(\frac{vst_{i,j} - vst_{i-1,j}}{\Delta x} \frac{ut0_{i+1,j} - ut0_{i-1,j}}{2\Delta x} + \frac{vst_{i,j} + vst_{i-1,j}}{2} \frac{ut0_{i+1,j} - 2 * ut0_{i,j} + ut0_{i-1,j}}{\Delta x^2} \right) \\
&= \frac{\Delta t}{2 \text{Re} \Delta x^2} [vst_{i,j} ut0_{i+1,j} + vst_{i-1,j} ut0_{i-1,j} - (vst_{i,j} + vst_{i-1,j}) ut0_{i,j}]
\end{aligned}$$

$$\begin{aligned}
A1V &= A_1(u_2^n) = \frac{\Delta t}{2 \text{Re}} \frac{\partial}{x} \left(\left(1 + \frac{v_Y}{v}\right) \frac{\partial}{x} \right) u_2^n = \frac{\Delta t}{2 \text{Re}} \frac{\partial}{x} \left(vst \frac{\partial}{x} \right) u_2^n = \frac{\Delta t}{2 \text{Re}} \left(\frac{\partial vst}{\partial x} \frac{\partial vt0}{\partial x} + vst \frac{\partial^2 vt0}{\partial x^2} \right) \\
&= \frac{\Delta t}{2 \text{Re}} \left(\frac{vst_{i+1,j} + vst_{i+1,j-1} - vst_{i-1,j} - vst_{i-1,j-1}}{4\Delta x} \frac{vt0_{i+1,j} - vt0_{i-1,j}}{2\Delta x} \right. \\
&\quad \left. + \frac{vst_{i,j-1} + vst_{i,j}}{2} \frac{vt0_{i+1,j} - 2 * vt0_{i,j} + vt0_{i-1,j}}{\Delta x^2} \right)
\end{aligned}$$

$$\begin{aligned}
A2U &= A_2(u_1^n) = \frac{\Delta t}{2 \text{Re}} \frac{\partial}{\partial y} \left(\left(1 + \frac{v_T}{\nu}\right) \frac{\partial}{\partial y} \right) u_1^n = \frac{\Delta t}{2 \text{Re}} \frac{\partial}{\partial y} \left(vst \frac{\partial}{\partial y} \right) u_1^n = \frac{\Delta t}{2 \text{Re}} \left(\frac{\partial vst}{\partial y} \frac{\partial ut0}{\partial y} + vst \frac{\partial^2 ut0}{\partial y^2} \right) \\
&= \frac{\Delta t}{2 \text{Re}} \left(\frac{vst_{i-1,j+1} + vst_{i,j+1} - vst_{i-1,j-1} - vst_{i,j-1}}{4\Delta y} \frac{ut0_{i,j+1} - ut0_{i,j-1}}{2\Delta y} \right. \\
&\quad \left. + \frac{vst_{i-1,j} + vst_{i,j}}{2} \frac{ut0_{i,j+1} - 2 * ut0_{i,j} + ut0_{i,j-1}}{\Delta y^2} \right) \\
A2V &= A_2(u_2^n) = \frac{\Delta t}{2 \text{Re}} \frac{\partial}{\partial y} \left(\left(1 + \frac{v_T}{\nu}\right) \frac{\partial}{\partial y} \right) u_2^n = \frac{\Delta t}{2 \text{Re}} \frac{\partial}{\partial y} \left(vst \frac{\partial}{\partial y} \right) u_2^n = \frac{\Delta t}{2 \text{Re}} \left(\frac{\partial vst}{\partial y} \frac{\partial vt0}{\partial y} + vst \frac{\partial^2 vt0}{\partial y^2} \right) \\
&= \frac{\Delta t}{2 \text{Re}} \left(\frac{vst_{i,j} - vst_{i,j-1}}{\Delta y} \frac{vt0_{i,j+1} - vt0_{i,j-1}}{2\Delta y} + \frac{vst_{i,j-1} + vst_{i,j}}{2} \frac{vt0_{i,j+1} - 2 * vt0_{i,j} + vt0_{i,j-1}}{\Delta y^2} \right) \\
&= \frac{\Delta t}{2 \text{Re} \Delta y^2} [vst_{i,j} vt0_{i,j+1} + vst_{i,j-1} vt0_{i,j-1} - (vst_{i,j-1} + vst_{i,j}) vt0_{i,j}]
\end{aligned}$$

Then we have the right side terms of the equations.

$$\begin{aligned}
YU_{i,j} &= \frac{\Delta t}{2} (3 * HU0 - HU0M) + 2 * (A1U + A2U) \\
YV_{i,j} &= \frac{\Delta t}{2} (3 * HV0 - HV0M) + 2 * (A1V + A2V)
\end{aligned} \tag{E4.1}$$

The difference equations are as follows.

$$\begin{aligned}
(1 - A_1)(1 - A_2)(ut1 - ut0) &= YU_{i,j}, \quad i = 3, nx, j = 2, ny - 1 \\
(1 - A_1)(1 - A_2)(vt1 - vt0) &= YV_{i,j}, \quad i = 2, nx - 1, j = 3, ny - 1
\end{aligned} \tag{E4.2}$$

The values of eddy viscosity are needed at $i=2, nx$ and $j=2, ny-1$.

E.5. Solving $ut1$

The difference equations can be solved by two steps; first to solve UTY then to solve $ut1$. This can reduce the computation tremendously. However it needs extra boundary conditions for UTY, a function of second derivative of $ut1$ with respect to y . Fortunately the boundary conditions for UTY can be derived from the boundary conditions of $ut1$ at the current arrangement: no more conditions are needed. It would be more difficult if UTX, a function of $ut1$ derivative with respect to x , is solved first.

$$(1 - A_1)UTY = YU_{i,j}, \quad (1 - A_2)(ut1 - ut0) = UTY_{i,j}$$

$$[A][B][u] = YU, \quad u = ut1 - ut0$$

$$(1 - \frac{\Delta t}{2 \text{Re}} \frac{\partial}{\partial x} (vst \frac{\partial}{\partial x})) UTY = YU_{i,j}$$

$$(1 - \frac{\Delta t}{2 \text{Re}} \frac{\partial}{\partial y} (vst \frac{\partial}{\partial y})) (ut1 - ut0) = UTY_{i,j} \quad (\text{E5.1})$$

E.5.1 Matrices: A and B:

$$u_{i,j} - \frac{\Delta t}{2 \text{Re}} \left(\frac{vst_{i-1,j+1} + vst_{i,j+1} - vst_{i-1,j-1} - vst_{i,j-1}}{4\Delta y} \frac{u_{i,j+1} - u_{i,j-1}}{2\Delta y} \right. \\ \left. + \frac{vst_{i,j} + vst_{i-1,j}}{2} \frac{u_{i,j+1} - 2 * u_{i,j} + u_{i,j-1}}{\Delta y^2} \right) = UTY_{i,j}$$

The above algebraic equation set can be expressed by matrices:

$$Aa_{i,j}u_{i,j-1} + Ab_{i,j}u_{i,j} + Ac_{i,j}u_{i,j+1} = UTY_{i,j}$$

$$Aa_{i,j} = \frac{\Delta t}{2 \text{Re}} \frac{1}{8\Delta y^2} [vst_{i-1,j+1} + vst_{i,j+1} - vst_{i-1,j-1} - vst_{i,j-1} - 4(vst_{i,j} + vst_{i-1,j})]$$

$$Ab_{i,j} = 1 + \frac{\Delta t}{2 \text{Re}} \frac{1}{\Delta y^2} * (vst_{i,j} + vst_{i-1,j}) \quad (\text{E5.2})$$

$$Ac_{i,j} = -\frac{\Delta t}{2 \text{Re}} \frac{1}{8\Delta y^2} [vst_{i-1,j+1} + vst_{i,j+1} - vst_{i-1,j-1} - vst_{i,j-1} + 4(vst_{i,j} + vst_{i-1,j})]$$

$$i = 3, nx, \quad j = 3, ny - 2$$

At the wall the eddy viscosity is the molecular viscosity, that is $vst = 1$. At the inlet the flow is known, no subgrid model is needed, vst is also one. Therefore the coefficients are different at boundaries

$$Aa_{i,2} = \frac{\Delta t}{2 \text{Re}} \frac{1}{8\Delta y^2} [vst_{i-1,2} + vst_{i,2} + vst_{i-1,3} + vst_{i,3} - 4 - 4(vst_{i,2} + vst_{i-1,2})]$$

$$Ab_{i,2} = 1 + \frac{\Delta t}{2 \text{Re}} \frac{1}{\Delta y^2} * (vst_{i,2} + vst_{i-1,2})$$

$$Ac_{i,2} = -\frac{\Delta t}{2 \text{Re}} \frac{1}{8\Delta y^2} [vst_{i-1,2} + vst_{i,2} + vst_{i-1,3} + vst_{i,3} - 4 + 4(vst_{i,j} + vst_{i-1,j})]$$

The grid cells and their numbers are shown in Figure E.2. At boundaries the intermediate velocity (Kim & Moin, 1985) is

$$\begin{aligned}\hat{u}_i^{n+1} &= u_i^{n+1} + \Delta t \frac{\partial \phi^n}{\partial x_i} \\ \Rightarrow ut1 &= ut2 + \Delta t \frac{\partial \phi^n}{\partial x} \quad \text{and} \quad vt1 = vt2 + \Delta t \frac{\partial \phi^n}{\partial y}\end{aligned}\tag{E5.3}$$

For the velocity of left boundary at $n+1$, the lower half of the flow domain is the solid wall and the upper half is the inlet. At the wall the non-slip condition applies and at the inlet known velocity profiles are given. At the outlet two different boundary conditions can apply: the velocity gradient in streamwise direction is zero or the continuity condition. Here the zero gradient condition will be used, which implies fully developed flow at the outlet.

$$\frac{\partial u_i^{n+1}}{\partial x} = \frac{\partial u_i^n}{\partial x} = 0; \quad \frac{\partial vt2}{\partial x} = \frac{\partial vt0}{\partial x} = 0\tag{E5.4}$$

At outlet, from the Navier-Stokes equation and (E5.4) we have:

$$\begin{aligned}ut2_{nx+1} &= ut2_{nx-1}, \quad ut0_{nx+1} = ut0_{nx-1}, \quad u = ut1 - ut0 \\ \frac{\partial}{\partial x} \left(\frac{\partial p}{\partial x} \right)_{nx,j} &= 0, \quad \text{then} \quad \frac{\partial}{\partial x} \left(\frac{\partial \phi}{\partial x} \right)_{nx,j} = 0, \quad \frac{\partial u}{\partial x}_{nx,j} = 0 \\ u_{nx+1,j} &= u_{nx-1,j}, \quad \text{for all } j\end{aligned}$$

Then

$$\begin{aligned}\frac{\partial \mathcal{A}TY}{\partial x}_{nx,j} &= \frac{\partial}{\partial x} [(1 - A_2)u]_{nx,j} = (1 - A_2) \frac{\partial u}{\partial x}_{nx,j} = 0 \\ Ba_{nx,j} &= Ba_{nx,j} + Bc_{nx,j}\end{aligned}$$

Note that the operator A_2 is the derivative with respect to y .

At the inlet the eddy viscosity is one, since everything at inlet is known.

$$ut1_{2,j} = ut1_{bin} = u_{inlet} + \Delta t \frac{\partial \phi}{\partial x}, \quad ut2_{2,j} = u_{inlet}.$$

$$u_{2,j} = u_{inlet} + \Delta t \frac{\phi_{2,j} - \phi_{1,j}}{\Delta x} - ut0_{2,j}$$

$$\text{then } UTY_{2,j} = u_{2,j} - \frac{\Delta t}{2 \text{Re}} \frac{u_{2,j+1} - 2u_{2,j} + u_{2,j-1}}{\Delta y^2}$$

$$YU_{3,j} = YU_{3,j} - Ba_{3,j} UTY_{2,j}$$

The boundary condition at left lower half is non-slip. Similar to the above, just

$$ut1_{2,j} = \Delta t \frac{\partial \phi}{\partial x}, \quad ut2 = 0$$

E.5.3. Boundary Conditions for the Intermediate Velocity u

At top and bottom where $y=0$ or $y=2h$, the boundaries are a solid wall as shown in

Figure E.2. That is:

$$ut2 = vt2 = 0, \quad ut1_b = \Delta t \frac{\partial \phi}{\partial x}, \quad vt1_b = \Delta t \frac{\partial \phi}{\partial y} \quad (\text{E5.5})$$

Then:

$$\begin{aligned} ut1_{i,b1} &= 2\Delta t \frac{\partial \phi}{\partial x_{i,b1}} - ut1_{i,b1} \quad u = ut1 - ut0: \\ u_{i,b1} &= \Delta t \frac{\partial \phi}{\partial x_{i,b1}} - \frac{ut0_{i,1} - ut0_{i,2}}{2} = \Delta t \frac{\phi_{i,1} + \phi_{i,2} - \phi_{i-1,1} - \phi_{i-1,2}}{\Delta x} - \frac{ut0_{i,1} - ut0_{i,2}}{2} \\ u_{i,1} &= 2u_{i,b1} - u_{i,2} \end{aligned}$$

Similarly:

$$\begin{aligned} u_{i,bny} &= \Delta t \frac{\phi_{i,ny-1} + \phi_{i,ny} - \phi_{i-1,ny-1} - \phi_{i-1,ny}}{\Delta x} - \frac{ut0_{i,ny-1} + ut0_{i,ny}}{2} \\ u_{i,ny} &= 2u_{i,bny} - u_{i,ny-1} \end{aligned}$$

Hence:

$$\begin{aligned} Ab_{i,2} &= Ab_{i,2} - Aa_{i,2}, \quad UTY_{i,2} = YU_{i,2} - Aa_{i,2} * 2u_{i,b1} \\ Ab_{i,ny-1} &= Ab_{i,ny-1} - Ac_{i,ny-1}, \quad UTY_{i,ny-1} = YU_{i,ny-1} - Ac_{i,ny-1} * 2u_{i,bny} \end{aligned}$$

It is now ready to solve $utl = u + ut0$ at inbound, that is for $i = 2, nx + 1, j = 1, ny$. The values of utl at $i = 1$ will be discussed later.

E.6. Solving vtl

The same procedure to solve utl can be applied to vtl . The difference is that VTX , a function of second derivative of vtl with respect to x , is solved first. The reason is that it is easy to derive boundary conditions for VTX .

$$\begin{aligned}
 (1 - A_2)VTX &= YV_{i,j}, & (1 - A_1)(vt1 - vt0) &= VYX_{i,j} \\
 [A][B][v] &= YV \quad v = vt1 - vt0 \\
 \left(1 - \frac{\Delta t}{2 \text{Re}} \frac{\partial}{\partial y} (vst \frac{\partial}{\partial y})\right) VTX &= YV_{i,j} \\
 \left(1 - \frac{\Delta t}{2 \text{Re}} \frac{\partial}{\partial x} (vst \frac{\partial}{\partial x})\right) (vt1 - vt0) &= VTX_{i,j}
 \end{aligned} \tag{E6.1}$$

From (E6.1):

$$\begin{aligned}
 v_{i,j} - \frac{\Delta t}{2 \text{Re}} \left(\frac{vst_{i+1,j} + vst_{i+1,j-1} - vst_{i-1,j} - vst_{i-1,j-1}}{4\Delta x} \frac{v_{i+1,j} - v_{i-1,j}}{2\Delta x} \right. \\
 \left. + \frac{vst_{i,j} + vst_{i,j-1}}{2} \frac{v_{i+1,j} - 2 * v_{i,j} + v_{i-1,j}}{\Delta x^2} \right) &= VTY_{i,j} \\
 Aa_{i,j} v_{i-1,j} + Ab_{i,j} v_{i,j} + Ac_{i,j} v_{i+1,j} &= VTX_{i,j} \\
 Aa_{i,j} &= \frac{\Delta t}{2 \text{Re}} \frac{1}{8\Delta x^2} [vst_{i+1,j} + vst_{i+1,j-1} - vst_{i-1,j} - vst_{i-1,j-1} - 4(vst_{i,j-1} + vst_{i,j})] \\
 Ab_{i,j} &= 1 + \frac{\Delta t}{2 \text{Re}} \frac{1}{\Delta x^2} (vst_{i,j} + vst_{i,j-1}) \\
 Ac_{i,j} &= -\frac{\Delta t}{2 \text{Re}} \frac{1}{8\Delta x^2} [vst_{i+1,j} + vst_{i+1,j-1} - vst_{i-1,j} - vst_{i-1,j-1} + 4(vst_{i,j-1} + vst_{i,j})]
 \end{aligned}$$

$$i = 3, nx - 1 \text{ and } j = 3, ny - 1$$

At the inlet and the wall, the eddy viscosity is one, therefore:

$$\begin{aligned}
Aa_{2,j} &= \frac{\Delta t}{2 \text{Re}} \frac{1}{8\Delta x^2} [vst_{2,j} + vst_{2,j-1} + vst_{3,j} + vst_{3,j-1} - 4 - 4(vst_{2,j-1} + vst_{2,j})] \\
Ab_{2,j} &= 1 + \frac{\Delta t}{2 \text{Re}} \frac{1}{\Delta x^2} (vst_{2,j} + vst_{2,j-1}) \\
Ac_{2,j} &= -\frac{\Delta t}{2 \text{Re}} \frac{1}{8\Delta x^2} [vst_{2,j} + vst_{2,j-1} + vst_{3,j} + vst_{3,j-1} - 4 + 4(vst_{2,j-1} + vst_{2,j})]
\end{aligned}$$

At the outlet, the zero gradient condition applies, that is $\frac{\partial vst}{\partial x} = 0$: $vst_{nx,j} = vst_{nx-1,j}$.

$$Ba_{i,j} VTX_{i,j-1} + Bb_{i,j} VTX_{i,j} + Bc_{i,j} VTX_{i,j+1} = YV_{i,j}$$

$$Ba_{i,j} = -\frac{\Delta t}{2 \text{Re}} \frac{1}{\Delta y^2} vst_{i,j-1}$$

$$Bb_{i,j} = 1 + \frac{\Delta t}{2 \text{Re}} \frac{1}{\Delta y^2} * (vst_{i,j} + vst_{i,j-1}) \quad i = 2, nx \text{ and } j = 3, ny - 1$$

$$Bc_{i,j} = -\frac{\Delta t}{2 \text{Re}} \frac{1}{\Delta y^2} vst_{i,j}$$

E. 6.1 Boundary Conditions for VTX:

Same as for u , at top and bottom it is a solid wall, and the non-slip condition applies for v at $n+1$. For the intermediate velocity at boundaries, from (E5.1):

$$vt1_b = vt2 + \Delta t \frac{\partial \phi}{\partial y} = \Delta t \frac{\partial \phi}{\partial y} \Big|_b$$

Then at the lower boundary:

$$v_{i,2} = \Delta t \frac{\phi_{i,2} - \phi_{i,1}}{\Delta y} - vt0_{i,2}, \quad vt0_{i,2} = 0$$

$$VTX_{i,2} = v_{i,2} - \frac{\Delta t}{2 \text{Re}} \frac{v_{i+1,2} - 2v_{i,2} + v_{i-1,2}}{\Delta x^2}$$

$$YU_{i,3} = YU_{i,3} - Ba_{i,3} VTX_{i,2}$$

At the upper boundary:

$$v_{i,ny} = \Delta t \frac{\phi_{i,ny} - \phi_{i,ny-1}}{\Delta y} - vt0_{i,ny}, \quad vt0_{i,ny} = 0$$

$$VTX_{i,ny} = v_{i,ny} - \frac{\Delta t}{2 \text{Re}} \frac{v_{i+1,ny} - 2v_{i,ny} + v_{i-1,ny}}{\Delta x^2}$$

$$YU_{i,ny-1} = YU_{i,ny-1} - Bc_{i,ny-1} VTX_{i,ny}$$

E.6.2 Boundary Conditions for v

At the boundary, the lower half is solid wall and the upper half is the inlet. At right boundary, it is outlet, velocity derivatives are zero.

$$\frac{\partial u_i^{n+1}}{\partial x} = \frac{\partial u_i^n}{\partial x} = 0; \quad \frac{\partial vt2}{\partial x} = \frac{\partial vt0}{\partial x} = 0$$

At outlet, same as for u :

$$vt2_{nx,j} = vt2_{nx-1,j} \quad \text{and} \quad vt0_{nx,j} = vt0_{nx-1,j}$$

$$vt1_{nx,j} = vt1_{nx-1,j}; \quad v_{nx,j} = v_{nx-1,j}$$

Then

$$Ab_{nx-1,j} = Ab_{nx-1,j} + Ac_{nx-1,j}$$

At inlet:

$$vt2_{1,j} = 2vinlet_j - vt2_{2,j}$$

$$vt1_{1,j} = vt2_{1,j} + \Delta t \left. \frac{\partial \phi}{\partial y} \right|_{1,j} = -vt1_2 + 2vinlet_j + \Delta t \left. \frac{\partial \phi}{\partial y} \right|_{1,j} + \Delta t \left. \frac{\partial \phi}{\partial y} \right|_{2,j}$$

$$v_{1,j} = vt1_{1,j} - vt0_{1,j} = 2v_{in,j} - v_{2,j}$$

$$v_{in,j} = vinlet_j + \Delta t \frac{\phi_{1,j} - \phi_{1,j-1} + \phi_{2,j} - \phi_{2,j-1}}{2\Delta y} - \frac{vt0_{2,j} + vt0_{1,j}}{2}$$

$$VTX_{2,j} = VYX_{2,j} - 2Aa_{2,j}v_{in,j} \quad \text{and} \quad Ab_{2,j} = Ab_{2,j} - Aa_{2,j}$$

The boundary condition at left lower half is non-slip.

$$vinlet_j = 0$$

Then it is ready to solve vtl for $i=1, nx; j=2, ny$ after applying boundary conditions. At $j=1$ and $j=ny+1$, vtl can be obtained specially, as will be discussed in E.7.

E.7. Intermediate Velocity Outside of the Bounds

Since staggered grids are used, outside the boundaries there are some points that are difficult to calculate; such as $v_{i,1}$, $v_{i,m+1}$ and $u_{1,j}$, $u_{n+1,j}$ in Figure E.2. The velocity values at those points are needed in the computation of pressure terms in Part 2 of appendix E. A special difference quotient was used to compute those values at the points (Stummel et al., 1980).

$$P'_{0,1,2,3}(x_0) = \frac{1}{6\Delta x} [2P(x_3) - 9P(x_2) + 18P(x_1) - 11P(x_0)]$$

$$P''_{0,1,2,3}(x_0) = \frac{1}{\Delta x^2} [-P(x_3) + 4P(x_2) - 5P(x_1) + 2P(x_0)]$$

The above quotients use grid points at one direction for derivatives. So after the velocity values at inner points and boundaries are known, the values at outside points can be obtained by the equation (2.16) with the above quotients. The intermediate velocity (\hat{u}_i^{n+1}) needs to be solved by this method because continuity does not apply to the velocity. Continuity can be used to solve the corrected velocity very easily.

PART II: To Solve the Pressure Term ϕ

It is the Poisson equation for the pressure term. We already known that ϕ is the second order approximate of pressure.

$$\frac{\partial^2 \phi}{\partial x_j \partial x_j} = \frac{1}{\Delta t} \frac{\partial \hat{u}_i^{n+1}}{\partial x_i} \Rightarrow \frac{\partial^2 \phi}{\partial x^2} + \frac{\partial^2 \phi}{\partial y^2} = \frac{1}{\Delta t} \left(\frac{\partial \hat{u}^{n+1}}{\partial x} + \frac{\partial \hat{v}^{n+1}}{\partial y} \right)$$

For staggered grid:

$$\frac{\partial ut1}{\partial x} \Big|_{p-ij} = \frac{ut1_{i+1,j} - ut1_{i,j}}{\Delta x}, \quad \frac{\partial vt1}{\partial y} \Big|_{p-ij} = \frac{vt1_{i,j+1} - vt1_{i,j}}{\Delta y}$$

$$Q_{i,j} = \frac{1}{\Delta t} \left(\frac{ut1_{i+1,j} - ut1_{i,j}}{\Delta x} + \frac{vt1_{i,j+1} - vt1_{i,j}}{\Delta y} \right)$$

For inner grids, $i=2, n, j=2, m$

Let $PSI = \phi$, then

$$\frac{PSI_{i+1,j} - 2PSI_{i,j} + PSI_{i-1,j}}{\Delta x^2} + \frac{PSI_{i,j+1} - 2PSI_{i,j} + PSI_{i,j-1}}{\Delta y^2} - Q_{i,j} = 0$$

$$Rt = \frac{PSI_{i+1,j}^k + PSI_{i-1,j}^k}{\Delta x^2} + \frac{PSI_{i,j+1}^k + PSI_{i,j-1}^k}{\Delta y^2} - 2\left(\frac{1}{\Delta x^2} + \frac{1}{\Delta y^2}\right)PSI_{i,j}^k$$

$$PSI_{i,j}^{k+1} = PSI_{i,j}^k + \frac{1}{2}w(Rt - Q_{i,j}) / \left(\frac{1}{\Delta x^2} + \frac{1}{\Delta y^2}\right)$$

$$PSI_{i,j} = PSI_{i,j}^{k+1}, \text{ when } PSI_{i,j}^{k+1} - PSI_{i,j}^k < 10^{-6}$$

where w is the relaxation coefficient.

At boundary special treatments are needed as in Kim and Moin (1985):

$$j=1: \quad \frac{PSI_{i+1,1} - 2PSI_{i,1} + PSI_{i-1,1}}{\Delta x^2} + \frac{1}{\Delta y} \frac{PSI_{i,2} - PSI_{i,1}}{\Delta y} = Q_{i,1} - \frac{\Delta t}{\Delta y} (vt2_{i,1} - vt1_{i,1})$$

$j=ny$:

$$\frac{PSI_{i+1,ny} - 2PSI_{i,ny} + PSI_{i-1,ny}}{\Delta x^2} - \frac{1}{\Delta y} \frac{PSI_{i,ny} - PSI_{i,ny-1}}{\Delta y} = Q_{i,ny} - \frac{\Delta t}{\Delta y} (vt2_{i,ny+1} - vt1_{i,ny+1})$$

$$i=1: \quad \frac{PSI_{1,j+1} - 2PSI_{1,j} + PSI_{1,j-1}}{\Delta y^2} + \frac{1}{\Delta x} \frac{PSI_{2,j} - PSI_{1,j}}{\Delta x} = Q_{1,j} - \frac{\Delta t}{\Delta x} (ut2_{1,j} - ut1_{1,j})$$

$i=nx$:

$$\frac{PSI_{nx,j+1} - 2PSI_{nx,j} + PSI_{nx,j-1}}{\Delta y^2} - \frac{1}{\Delta x} \frac{PSI_{nx,j} - PSI_{nx-1,j}}{\Delta x} = Q_{nx,j} - \frac{\Delta t}{\Delta x} (ut2_{nx+1,j} - ut1_{nx+1,j})$$

With PSI known, new $ut2$ and $vt2$ can be calculated at inner grids as:

$$u_i^{n+1} = \hat{u}_i^{n+1} - \Delta t \frac{\partial PSI}{\partial x_i}$$

$$ut2_{i,j} = ut1_{i,j} - \Delta t \frac{PSI_{i,j} - PSI_{i-1,j}}{\Delta x}, \text{ and } vt2_{i,j} = vt1_{i,j} - \Delta t \frac{PSI_{i,j} - PSI_{i,j-1}}{\Delta y}$$

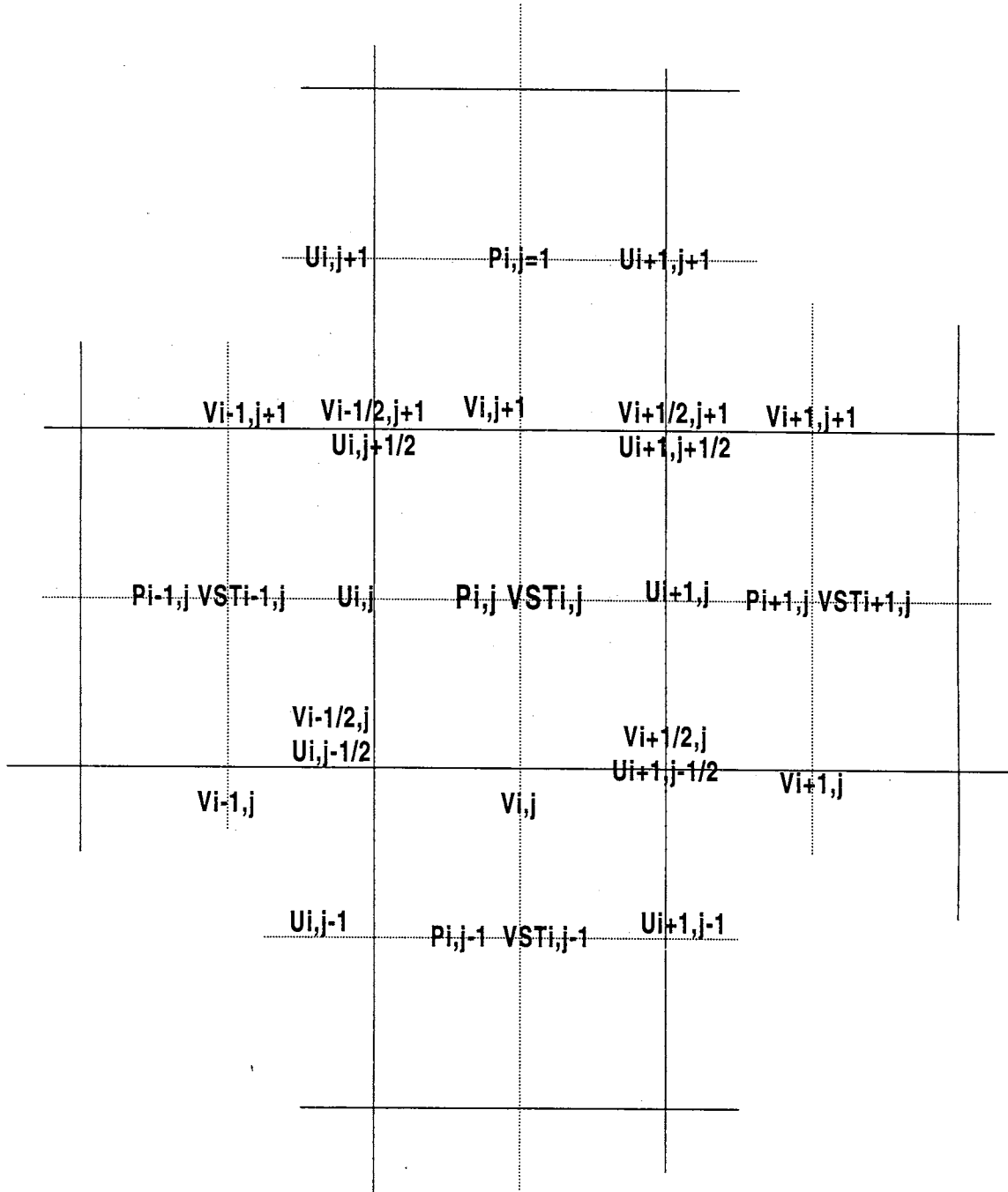


Figure E.1. Staggered grids for the inner points.

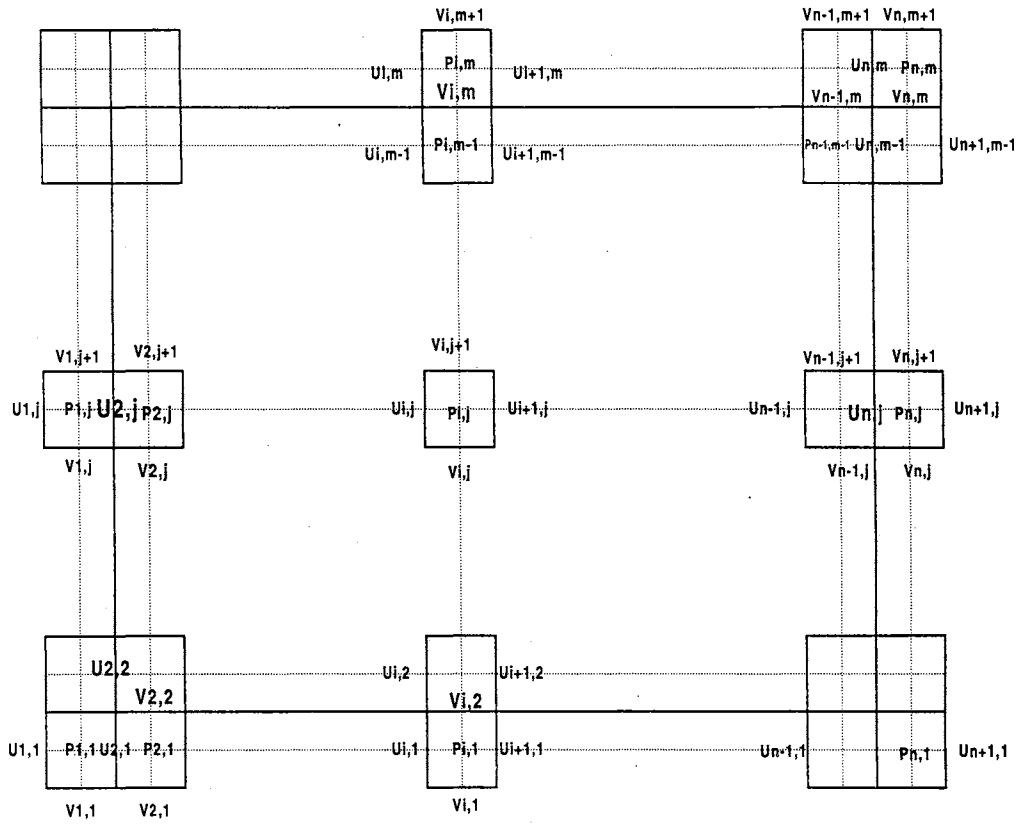


Figure E.2. Staggered grids at the boundaries.

F. DIFFERENCE AT THE INTERFACES OF MEDIUM AND FLUIDS

F.1. Interface:

At the interface, continuity applies to the velocity and shear stress as follows.

$$\begin{aligned}
 u_{air} &= u_{med}, & P_{air} + 2\mu \frac{\partial u_{air}}{\partial x} &= P_{med} + 2\mu \frac{\partial u_{med}}{\partial x} \\
 v_{air} &= v_{med}, & \mu \frac{\partial v_{air}}{\partial x} &= \mu \frac{\partial v_{med}}{\partial x}
 \end{aligned}
 \tag{F.1}$$

The difference grids with respect to the variables are shown in Figure F.1.

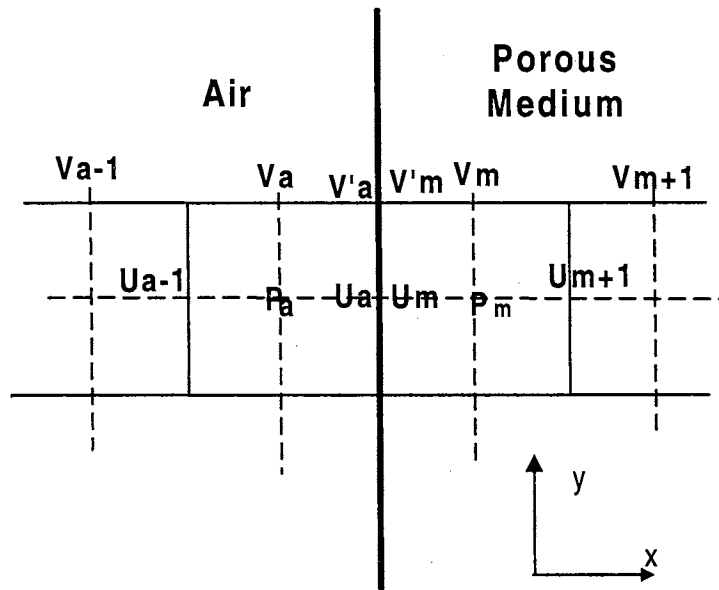


Figure F.1. Grid system at the interface of the filter.

The subscript m indicates medium and a indicates air. The finite difference approximation for the continuity conditions are as follows:

$$\text{Let } u_a = u_m = u_{am}, \text{ and } v_a = v_m = v_{am}, \text{ and we know at the interface } P_{air} = P_{med},$$

then

$$\frac{u_{am} - u_{a-1}}{\Delta x} = \frac{u_{m+1} - u_{am}}{\Delta x_m} \quad (F.2)$$

$$\frac{v_{am} - v_a}{\Delta x} = \frac{v_m - v_{am}}{\Delta x_m}$$

The accuracy of the difference is first order. Then the relationships between the velocities at two sides are established as:

$$v_{am}^{n+1} = \frac{\frac{\Delta x_m}{\Delta x} v_a^{n+1} + v_m^{n+1}}{1 + \frac{\Delta x_m}{\Delta x}}$$

$$-\frac{\Delta x_m}{\Delta x} u_{a-1}^{n+1} + \left(1 + \frac{\Delta x_m}{\Delta x}\right) u_{am}^{n+1} - u_{m+1}^{n+1} = 0$$

The equations are normalized with the same scales as for the equations for pure fluids. However to keep it simple, the original symbols will be used here after normalization.

$$v_{am}^{n+1} = \frac{\frac{\Delta x_m}{\Delta x} v_a^{n+1} + v_m^{n+1}}{1 + \frac{\Delta x_m}{\Delta x}} \quad (F.3)$$

$$-\frac{\Delta x_m}{\Delta x} u_{a-1}^{n+1} + \left(1 + \frac{\Delta x_m}{\Delta x}\right) u_{am}^{n+1} - u_{m+1}^{n+1} = 0 \quad (F.4)$$

For UTY, defined as in appendix E.

$$-\frac{\Delta x_m}{\Delta x} UTY_{a-1}^{n+1} + \left(1 + \frac{\Delta x_m}{\Delta x}\right) UTY_{am}^{n+1} - UTY_{m+1}^{n+1} = 0$$

F.2. Equations for the Porous Medium

$$\bar{B} = \frac{B}{L}, \quad \bar{K} = \frac{K}{L^2}, \quad \text{Re} = \frac{UL}{\nu}, \quad p_m = \frac{p}{\rho U^2}$$

where U and L are the velocity and length scales to normalize the equations for both pure

fluids and porous medium. Then the non-dimensionalized equations for porous medium are:

$$\begin{aligned} \nabla \bullet u_m &= 0 \\ \frac{\partial u_m}{\partial t} &= -\phi_m \nabla p_m - \phi_m \left(\frac{\bar{B}}{\bar{K}} |u_m| + \frac{1}{\text{Re } \bar{K}} \right) u_m + \frac{1}{\text{Re}} \nabla^2 u_m \end{aligned} \quad (\text{F.5})$$

The time-split method will be applied to the equations above as follows:

$$\begin{aligned} \frac{\hat{u}_{mi}^{n+1} - u_{mi}^n}{\Delta t} &= \frac{1}{2} (3H_i^n - H_i^{n-1}) + \frac{1}{2\text{Re}} \nabla^2 (\hat{u}_{mi}^{n+1} + u_{mi}^n) \\ H_i^n &= -\phi_m \left(\frac{\bar{B}}{\bar{K}} |u_{mi}^n| + \frac{1}{\text{Re } \bar{K}} \right) u_{mi}^n \end{aligned}$$

Let $\frac{u_{mi}^{n+1} - \hat{u}_{mi}^{n+1}}{\Delta t} = \phi_m \nabla \varphi^{n+1}$ and we know $\nabla \bullet u_{mi}^{n+1} = 0$. (F.6)

Then: $\phi_m \nabla^2 \varphi^{n+1} = (\nabla \bullet \hat{u}_{mi}^{n+1}) / \Delta t$ and $p_m = (1 + \frac{\Delta t}{2\phi_m \text{Re}} \nabla^2) \varphi \cong \varphi$

Then the same CFD procedure for the pure fluid can be used to solve the flow inside the porous medium.

F.3. Handling the Intermediate Velocities at the Interface and Boundaries:

Substitute (F.3) and (F.4) into $\frac{u_{mi}^{n+1} - \hat{u}_{mi}^{n+1}}{\Delta t} = \phi_m \nabla p^{n+1}$

Let $\frac{\partial \varphi}{\partial y} \Big|_{am} = \frac{\frac{\Delta x_m}{\Delta x} \frac{\partial \varphi}{\partial y} \Big|_{va} + \phi_m \frac{\partial \varphi}{\partial y} \Big|_{vm}}{1 + \frac{\Delta x_m}{\Delta x}}$ and $\hat{v}_{am}^{n+1} = v_{am}^{n+1} + \frac{\partial \varphi}{\partial y} \Big|_{am} \Delta t$; (F.7)

then the intermediate velocity v at the interface is:

$$\hat{v}_{am}^{n+1} = \frac{\frac{\Delta x_m}{\Delta x} \hat{v}_a^{n+1} + \hat{v}_m^{n+1}}{1 + \frac{\Delta x_m}{\Delta x}}$$

It is different for velocity u since it goes through the interface:

$$\left. \frac{\partial p}{\partial x} \right|_{am} = \frac{2}{\Delta x} \frac{p_m - p_a}{1 + \frac{\Delta x_m}{\Delta x}} \text{ and } \hat{u}_{am}^{n+1} = u_{am}^{n+1} + \left. \frac{\partial p}{\partial x} \right|_{am} \Delta t; \quad (\text{F.8})$$

Substituting equation (H.8) into (F.4) will yield the equation for \hat{u}_i^{n+1} at interface. Since a time-split method is used for the pure fluids, the current pressure is not yet known. Its value at the previous time step is used. After \hat{u}_i^{n+1} is known for the whole domain, u_{am}^{n+1} can be obtained by equation (F.8) with the current known pressure.

At top or bottom solid walls, for v , the boundary conditions for the medium are non-slip, as for the homogeneous fluid.

F.4. VTX at the Interface:

UTY is easy to handle since its difference does not cross the interface, however VTX needs special consideration because it needs velocity values at both sides of the interface.

$$VTX_{i,j} = \left[1 - \frac{\Delta t}{2\text{Re}} \frac{\partial}{\partial x} (vst \frac{\partial}{\partial x}) \right] (\hat{v}_{i,j}^{n+1} - v_{i,j}^n)$$

At the interface, the flow is considered as laminar, therefore eddy viscosity will be one.

Here the formula is only for the upstream interface. The subscript al indicates the air side left of the interface.

$$\left. \frac{\partial v}{\partial x} \right|_{al,j} = \frac{2v_{am} - (v_{al} + v_{al-1})}{2\Delta x} = \frac{1}{2\Delta x} \left(\frac{2}{1 + \frac{\Delta x_m}{\Delta x}} v_{al+1} - \frac{1 - \frac{\Delta x_m}{\Delta x}}{1 + \frac{\Delta x_m}{\Delta x}} v_{al} - v_{al-1} \right)$$

$$\left. \frac{\partial^2 v}{\partial x^2} \right|_{al,j} = \frac{2(v_{am} - v_{al}) - (v_{al} - v_{al-1})}{\Delta x^2} = \frac{1}{\Delta x^2} \left(\frac{2}{1 + \frac{\Delta x_m}{\Delta x}} v_{al+1} - \frac{3 + \frac{\Delta x_m}{\Delta x}}{1 + \frac{\Delta x_m}{\Delta x}} v_{al} + v_{al-1} \right)$$

Then the same formula will be yielded as for the pure fluids.

$$A_{al,j}v_{al-1,j} + B_{al,j}v_{al,j} + C_{l,j}v_{al+1,j} = VT X_{al,j}$$

$$A_{al,j} = -reydx \left(\frac{bb}{2} - \frac{aa}{8} \right)$$

$$B_{al,j} = 1 + reyd x \left(\frac{bb}{2} \frac{3 + \frac{\Delta x_m}{\Delta x}}{1 + \frac{\Delta x_m}{\Delta x}} + \frac{aa}{8} \frac{1 - \frac{\Delta x_m}{\Delta x}}{1 + \frac{\Delta x_m}{\Delta x}} \right)$$

$$C_{al,j} = -reydx \left(\frac{bb}{2} + \frac{aa}{8} \right) \frac{2}{1 + \frac{\Delta x_m}{\Delta x}}$$

$$aa = 4 - (vst_{al,j} + vst_{al,j-1} + vst_{al-1,j} + vst_{al-1,j-1})$$

$$bb = vst_{al,j} + vst_{al,j-1} \quad reyd x = \frac{\Delta t}{2 \text{Re} \Delta x^2}$$

Similarly at right side of the interface, it is the medium:

$$\frac{\partial v}{\partial x} \Big|_{mr,j} = \frac{(v_{mr} + v_{mr+1}) - 2v_{am}}{2\Delta x_m} = \frac{1}{2\Delta x_m} \left(v_{mr+1} - \frac{1 - \frac{\Delta x_m}{\Delta x}}{1 + \frac{\Delta x_m}{\Delta x}} v_{mr} - \frac{2 \frac{\Delta x_m}{\Delta x}}{1 + \frac{\Delta x_m}{\Delta x}} v_{mr-1} \right)$$

$$\frac{\partial^2 v}{\partial x^2} \Big|_{mr,j} = \frac{(v_{mr+1} - v_{mr}) - 2(v_{mr} - v_{am})}{\Delta x_m^2} = \frac{1}{\Delta x_m^2} \left[v_{mr+1} - \left(3 - \frac{2}{1 + \frac{\Delta x_m}{\Delta x}} \right) v_{mr} + \frac{2 \frac{\Delta x_m}{\Delta x}}{1 + \frac{\Delta x_m}{\Delta x}} v_{mr-1} \right]$$

where mr indicates the medium side right of the interface.

$$A_{mr,j}v_{mr-1,j} + B_{mr,j}v_{mr,j} + C_{mr,j}v_{mr+1,j} = VT X_{mr,j}$$

$$A_{mr,j} = -reydx \frac{2 \frac{\Delta x_m}{\Delta x}}{1 + \frac{\Delta x_m}{\Delta x}}$$

$$B_{mr,j} = 1 + reyd x \left(3 - \frac{2}{1 + \frac{\Delta x_m}{\Delta x}} \right)$$

$$C_{mr,j} = -reydx \quad reyd x = \frac{\Delta t}{2 \text{Re} \Delta x^2}$$

At the downstream interface, the difference is just exchanging the coefficients

between $m + 1$ and $m - 1$ for the medium side. The same procedure applies when fluid is

at right side of the interface. Since inside the porous medium flow is laminar, therefore the eddy viscosity is the molecular viscosity.

F.5. Pressure Gradient at the Interface:

Since at the interface the relation between intermediate velocity and the pressure term are not the same as at inside points, the finite difference in x -direction need to be treated specially.

$$\frac{\partial^2 p}{\partial^2 x} = \frac{\frac{\partial p}{\partial x}\Big|_{am} - \frac{\partial p}{\partial x}\Big|_a}{\Delta x} = \frac{\frac{\partial p}{\partial x}\Big|_{am} - \frac{P_{mI-1} - P_{mI-2}}{\Delta x}}{\Delta x}, \text{ where } \frac{\partial p}{\partial x}\Big|_{am} \text{ is from Eq (F.8)}$$

At the right side of the interface we can obtain the formula similarly.

G. FOCUS POINTS FOR FOUR BEAM LDA THROUGH A TILTED WALL

For the two horizontal beams, because the LDV optical axis was perpendicular to the horizontal lines on both sides of the wall, the effect of the tilted wall was only the effective thickness: $\delta_1 = \delta / \sin(\alpha)$, as shown in Figure 3.4. The α is the angle between the vertical lines on the wall and the LDV optical axis, as in Fig. 3.5. Since the two sides of the wall were parallel, as stated in Durst et al. (1976), the out-coming beams were parallel to the incident beams for both horizontal and vertical arrangements.

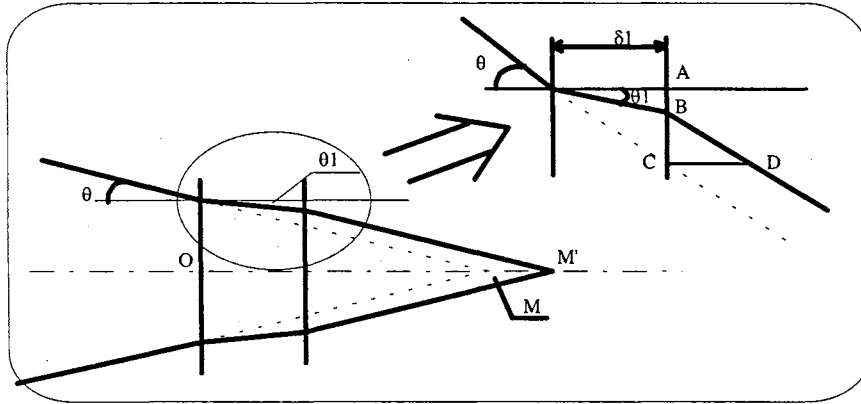


Figure G.1. Two horizontally arranged beams with a vertically tilted wall.

The formula to calculate the focus point changes is as follows:

$$\frac{\sin(\theta)}{\sin(\theta_1)} = n_{air,plex} \dots AB = \delta_1 \times \tan(\theta_1) \dots BC = \delta \times \tan(\theta) \dots \delta_1 = \delta / \sin(\theta)$$

$$CD = \frac{BC}{\tan(\theta)} = \frac{AC - AB}{\tan(\theta)} = \delta_1 \times \left[1 - \frac{\tan(\theta_1)}{\tan(\theta)} \right]$$

$$M'M = CD = \frac{\delta}{\sin(\alpha)} \left(1 - \frac{\cos(\theta)}{\sqrt{n^2 - \sin^2(\theta)}} \right)$$

The two vertical beams went through different paths, as shown in Figure G.1; therefore besides the MoM, shift on axis, there was a MoM', shift off axis.

distance between the two points is referred as the shift distance, which is L_s in Figure G.3.

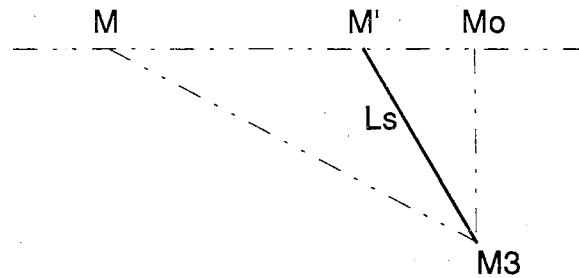


Figure G.3. The relation between the two points of measuring u and v .

The formula above can be used to compute the shift distance via the wall tilt angle α , the half angle between two beams θ and the thickness of the wall. However in the present study, the angles are given, the only variable left here is the wall thickness. From the formulas above, we can see that the shift distance is proportional to the wall thickness. The present θ is about 4.5 degrees and α is about 35 degrees. Refraction index n for the transparent wall is 1.5. Then we have the horizontal distance between two focused points is $MoM' = MoM - M'M = 0.152\delta$ and the vertical distance is $M3Mo = 0.449\delta$. The wall that was used is 2.5mm (0.1 inch) thick, which indicates the two focused points were 1.2 mm apart. For a filter with upwind surface of 114 mm by 170 mm the difference in measuring points is reasonably tolerable. The error is not critical since u and v are analyzed separately.

VITA

Shenghong Yao

Candidate for the Degree of

Doctor of Philosophy

Thesis: TWO DIMENSIONAL BACKWARD FACING SINGLE STEP FLOW
PRECEDING AN AUTOMOTIVE AIR-FILTER

Major Field: Mechanical Engineering

Biographical:

Personal Data: Born in Yuanshi/Hebei, China, on October 17, 1963, the son of
Kuilin Gao and Shuqin Yao.
Married Yibing Du, January 18, 1989.

Education: Received Bachelor of Engineering in Electrical Engineering from
Tianjin University, Tianjin, China in July 1983. Received Master of
Engineering in Fluid Mechanics from Tianjin University, Tianjin, China in
June 1986. Completed the requirements for the Doctor of Philosophy
degree with a major in Mechanical Engineering at Oklahoma State
University in May, 2000.

Professional Experience: Graduate Research Assistant, Oklahoma State
University, from June 1995 to December 1999. Research Associate,
Lisbon Institute of Science and technology, Portugal, from March 1994 to
December 1994. Associate Professor, Department of Mechanics, Tianjin
University, from September 1992 to February 1994. Lecturer, Department
of Mechanics, Tianjin University, from March 1989 to August 1992.